Title
Synthesis, Ion Exchange, and Properties of New Semiconductor Nanostructures

Author
Wong, Andrew Barnabas

Publication Date
2016

Synthesis, Ion Exchange, and Properties of New Semiconductor Nanostructures

By

Andrew Barnabas Wong

A dissertation submitted in partial satisfaction of the
Requirements for the degree of
Doctor of Philosophy
in
Chemistry
in the
Graduate Division
of the
University of California, Berkeley

Committee in charge:

Professor Peidong Yang, Chair
Professor Felix Fischer
Professor Ting Xu
Professor Ali Javey

Fall 2016

Abstract

Synthesis, Ion Exchange, and Properties of New Semiconductor Nanostructures

By

Andrew Barnabas Wong

Doctor of Philosophy in Chemistry

University of California, Berkeley

Professor Peidong Yang, Chair

Advances in the synthetic control of semiconductor nanostructures and material properties offers many opportunities to enable new technologies. This is especially true for advances in the areas of photovoltaics, light emitting diodes, photodetectors, transistors, miniaturized lasers, and thermoelectrics. In this work, I demonstrate the synthesis and properties of several novel nanoscale morphologies composed of copper sulfide, cadmium sulfide, and halide perovskite, which can be useful for these applications. Here, I demonstrate the first synthesis of Cu_2S-CdS core-shell nanowires by reverse cation exchange, and I explore the evolution of the epitaxial interface during the cation exchange. In addition, I demonstrate the synthesis and photovoltaic properties of core-shell CdS-Cu_2S nanorod arrays with power conversion efficiencies approaching 4%. I also demonstrate the first bottom-up synthesis of $CH_3NH_3PbBr_3$ nanorod arrays and the first example of morphology-conserving anion exchange to $CH_3NH_3PbI_3$. As a demonstration of this, I created and characterized the first halide perovskite nanorod array light emitting diodes. Furthermore, using the first example of ultrathin halide perovskites, I demonstrate the unexpected changes in the structural and optical properties of layered halide perovskites as they approach ultrathin thicknesses. Finally, I synthesized the first example of all-inorganic, lead-free perovskite $CsSnI_3$, which is shown to possess strong photoluminescence at 1.3 eV, metallic electrical conductivity, and ultralow thermal conductivity. These research directions all contribute towards the ultimate goal of providing new nanostructured materials to enable new technologies and innovations, which might also lead to new energy generating and energy saving applications.

Dedication

To my Mom, my Dad, and Simonia.
Without their support, nothing I have done or will do would have been possible.

Table of Contents

Chapter 1: Cu_2S-CdS Core-Shell Nanowires by Reverse Cation Exchange

Chapter 2: CdS-Cu_2S Core-Shell Nanowire Array Photovoltaics by Cation Exchange

Chapter 3: Synthesis, Anion Exchange, and Electroluminescence of $CH_3NH_3PbBr_3$

Chapter 4: Properties of Atomically Thin Layered Perovskites

Chapter 5: Synthesis and Properties of $CsSnI_3$ Nanowires and Nanostructures

Acknowledgements

Looking back on my time in graduate school, I have benefited greatly from the help of many individuals and relatively good fortune (overall) during graduate school. To these individuals, I owe all the successes I have had and will ever have. To repay them, I can only promise to do my best both to make worthwhile contributions and to help others as I had been helped.

At a personal level, I do owe a lot of my success to my Mom and Dad for their encouragement, their love, their support, and their industry. Unfortunately, for better or worse, the decision to move far from home has come at a high cost to them, and I would like to take this opportunity to acknowledge their sacrifice and their understanding of my dream of making contributions in the sciences.

While at the University of Chicago, I benefited from excellent support and perspectives during my time as an undergraduate. My advisors Prof. Stuart A. Rice, Laurens Mets, and Dr. Binhua Lin proved instrumental in my fledging understanding of what it meant to pursue research. I am thankful for the opportunity to benefit from their experience and to enjoy their support. It was Stuart Rice, who convinced me that I should attend UC Berkeley, and I am very thankful for that advice.

While at UC Berkeley, I was fortunate to meet Simonia, another alumnus of UChicago, the love of my life, and my future wife. She has stood with me and supported me throughout the good and bad times while putting my goals often above her own. I cannot express how thankful I am for her love and unconditional support both now and in the future. I would be hard pressed to explain whether I really merit her dedication. In addition, I am grateful that both of Simonia's parents have been supportive of me and have encouraged me to do my best. These last few years they have been like a second set of parents to me. Last of all, Simonia, thank you for everything you have done. You mean the world to me.

It almost goes without being said that I am very thankful for my advisor's support. Although I suspect that Prof. Peidong Yang may not fully realize the extent to which I have learned from observing how he approaches research, I am very thankful to have learned so much from him. I hope that I may be so fortunate as to be able to pass on what I have learned from him to many others.

I have benefited tremendously from the support and perspectives of the entire Peidong Yang Group over the last several years, and I would like to thank everyone of my peers for our positive interactions. Specifically, I would like to name several senior students of Peidong who stand out in that they have taught me a lot: Dr. Christopher Hahn, Dr. Ziyang Huo, Dr. Jinyao Tang, Dr. Neil Dasgupta, Dr. Letian Dou, and Dr. Woochul Lee. It has been my pleasure to work closely with these talented individuals and to learn from their experiences over the years. In addition, I would like to acknowledge Dr. Sarah Brittman for her help and mentorship during the cation exchange portion of my graduate work. It was with her help that I learned lithography techniques that I applied to successfully publish my photovoltaics paper. In addition, I would like to thank Dr. Anthony Fu for getting me interested in optics as well as making the initial suggestion that I should consider if it is possible to synthesize perovskite nanostructures.

Among my lab mates, Dr. Kelsey Sakimoto also deserves special recognition. I am glad that he accepted my suggestion that he should pick a desk near me so we could chat about research. It has been a pleasure to discuss about a wide range of issues and questions. This is especially true given our contrasting worldviews. In particular, I am glad that we were able to work together on his work on the hybrid organism *Moorella thermoacetica*-CdS to achieve the self-photosensitization of a non-photosynthetic organism. I feel that my intellectual contributions to this work are the most significant contributions I have made to society in my scientific career thus far. I am thankful for the collaboration on our unorthodox idea.

Now, I would also like to acknowledge the financial support that enabled my research. I would like to acknowledge the research support of the Bay Area Photovoltaic Consortium, DOE prime award number DE-EE0004946 and sub-award number 60094384-51077-D. In addition, I would like to acknowledge the funding from the Office of Science, Office of Basic Energy Sciences, of the U.S. Department of Energy under Contract No. DE-AC02-05CH11231. Finally, I would like to acknowledge the support of the LAM Research Graduate Fellowship.

The work in Chapter 1 was based off of: A. B. Wong, P. Yang, Cu_2S-CdS Core-Shell Nanowires through Reverse Cation Exchange. *In Preparation*.

The work in Chapter 2 was based off of: A. B. Wong, S. Brittman, Y. Yu, N. P. Dasgupta, P. Yang, Core–Shell CdS–Cu_2S Nanorod Array Solar Cells, *Nano Lett.*, **15**, 4096–4101, 2015.

The work in Chapter 3 was based off of: A. B. Wong, M. Lai, S. W. Eaton, Y. Yu, E. Lin, L. Dou, A. Fu, P. Yang, Growth and Anion Exchange Conversion of $CH_3NH_3PbX_3$ Nanorod Arrays for Light-Emitting Diodes, *Nano Lett.*, **15**, 5519–5524, 2015.

The work in Chapter 4 was based off of: L. Dou*, A. B. Wong*, Y. Yu*, M. Lai, N. Kornienko, S. W. Eaton, A. Fu, C. G. Bischak, J. Ma, T. Ding, N. S. Ginsberg, L.-W. Wang, A. P. Alivisatos, P. Yang, Atomically Thin Two-dimensional Organic-inorganic Hybrid Perovskites, *Science*, **349**, 1518–1521, 2015.

The paper that Chapter 4 is based on is a joint work. The original synthesis of ultrathin halide nanoplates was accomplished by Dr. Letian Dou. I performed and interpreted the results of the optical experiments as well as the connection of these results to the structural work, which was led by Dr. Yi Yu. I offer them many thanks for this wonderful collaboration.

The work in Chapter 5 was based off of: W. Lee*, H. Li*, A. B. Wong*, D. Zhang, M. Lai, Y. Yu, Q. Kong, E. Lin, J. J. Urban, J. C. Grossman, P. Yang, Ultralow thermal conductivity in all-inorganic halide perovskites. *Nature*, *In Review*.

The paper that Chapter 5 is based off of is also another joint publication, which is currently in preparation for submission. In this work, I developed the synthesis of $CsSnI_3$ nanowires and performed the structural and optical characterization. Dr. Woochul Lee led the experimental investigation of the transport properties of $CsSnI_3$ nanowires, and together we developed a means to characterize these nanowires using our existing measurement platforms without the degradation of the suspended nanowire measurement devices that can result from the inherent instability of $CsSnI_3$ in ambient air. I would like to thank Dr. Lee for teaching me a great deal about thermal transport measurements. Dr. Huashan Li led the computational efforts to understand the experimental results in this work. In the manuscript that this chapter is based on, a discussion of electrically insulating $CsPbBr_3$ and $CsPbI_3$ nanowires is also included. However, Chapter 5 solely discusses the $CsSnI_3$ nanowires that I developed.

Preface

At present, the continued growth of population, technology, and industry has driven the demand for energy to power increasingly complex and numerous devices. As a result, there is now a need to develop increasingly efficient devices as well as to develop new energy harvesting technologies. As a field, the study of chemistry holds the potential to unlock new technologies for increasing energy efficiency and supply.

In order to explore the potential for the development of new technologies, it is necessary to synthesize and evaluate the properties of new materials and new morphologies. To this end, nanostructures as nanorod arrays and two-dimensional platelets are interesting morphologies to explore. This is especially true for the case of earth-abundant solution processable semiconductors such as metal sulfides and halide perovskites, which have shown initial promise for application as photovoltaic materials in the lab scale.

Chapter 1 explores the first report of using a reverse cation exchange reaction to synthesize core-shell Cu_2S-CdS nanowires with an epitaxial heterojunction between p-type Cu_2S and n-type CdS. The structural formation of the interface during the cation exchange is studied *ex situ* using high resolution transmission electron microscopy and energy dispersive X-ray spectroscopy. The heterojunction is found to be epitaxial from the initial stages of the reaction and the conversion of the CdS shell is found to occur via the merging of epitaxial islands of CdS into a continuous shell.

Chapter 2 details the synthesis and fabrication of a solution-processed CdS-Cu_2S core-shell nanorod array photovoltaic device, with an efficiency approaching 4%. The CdS nanorod arrays are synthesized using a hydrothermal technique, and a solution phase cation exchange reaction is used to grow an epitaxial Cu_2S shell on the CdS nanorod core. The epitaxy of the Cu_2S on the CdS is established by selected area electron diffraction.

Chapter 3 details the synthesis of the first $CH_3NH_3PbBr_3$ nanorod arrays and the invention of anion exchange reactions in hybrid perovskite nanostructures. These $CH_3NH_3PbBr_3$ nanorod arrays were converted to $CH_3NH_3PbI_3$ nanorod arrays by annealing in CH_3NH_3I vapor, which is the first example of morphology-preserving anion exchange in the halide perovskites. To show the utility of this technique, the first hybrid perovskite nanorod light-emitting diodes were fabricated and characterized. The optical properties of these materials before and after anion exchange were also explored.

Chapter 4 describes the structural and optical characterization of the first ultrathin layered halide perovskites of a composition of $(C_4H_9NH_3)_2PbX_4$ with X = Cl, Br, or I. This composition consists of a series of Pb-X sheets that serve as quantum wells. Previously, it was believed that the butylammonium chains electronically isolated these quantum wells in a bulk crystal of these materials, and their properties had never been explored at the nanoscale. Using the first synthesis of ultrathin $(C_4H_9NH_3)_2PbX_4$, the optical and structural properties of this material is investigated on the nanoscale for the first time. It is found that as these two dimensional sheets approach atomically thin thicknesses, they display an unexpected structural relaxation leading to a blue shifting of the band gap.

Chapter 5 details the development of the first synthesis of $CsSnI_3$ nanowires, which are synthesized in solution without a reducing agent. $CsSnI_3$ is an example of an all-inorganic, lead-free perovskite, and is a direct band gap semiconductor with strong photoluminescence at 1.3 eV. Amazingly, we have shown that $CsSnI_3$ is a p-type semiconductor that possesses often contraindicated properties: metallic electrical transport and ultralow thermal conductivity. Following Chapter 5, I conclude with my thoughts and perspectives about the trajectory of nanoscale energy materials research as related to my work.

Curriculum Vitae

(* Denotes Equal Contribution, Papers Listed in Chronological Order)

1. A. B. Wong*, Y. Bekenstein*, C. Kley, D. Kim, A. P. Alivisatos, P. Yang, Colloidal $CsSnI_3$ Perovskite Nanoplates, *In Preparation.*
2. W. Lee*, H. Li*, A. B. Wong*, D. Zhang, M. Lai, Y. Yu, Q. Kong, E. Lin, J. J. Urban, J. C. Grossman, P. Yang, Ultralow thermal conductivity in all-inorganic halide perovskites. *Nature*, *In Review*.
3. Y. Yu, D. Zhang, C. Kisielowski, L. Dou, N. Kornienko, Y. Bekenstein, A. B. Wong, A. P. Alivisatos, P. Yang, Atomic Resolution Imaging of Halide Perovskites, *Nano Lett.*, *In press*.
4. D. Zhang*, Y. Yu*, Y. Bekenstein*, A. B. Wong, A. P. Alivisatos, P. Yang, Ultrathin Colloidal Cesium Lead Halide Perovskite Nanowires, *JACS*, **138**, 13155-13158, 2016.
5. D. Zhang*, Y. Yang*, Y. Bekenstein*, Y. Yu, N. A. Gibson, A. B Wong, S. W Eaton, N. Kornienko, Q. Kong, M. Lai, A. P. Alivisatos, S. R. Leone, P. Yang, Synthesis of Composition Tunable and Highly Luminescent Cesium Lead Halide Nanowires through Anion-Exchange Reactions, *JACS*, **138**, 7236–7239, 2016.
6. S. W. Eaton, A. Fu, A. B. Wong, C.-Z. Ning, P. Yang, Semiconductor Nanowire Lasers, *Nature Rev. Mater.*, **1**, 16028, 2016.
7. S. W. Eaton, M. Lai, N. A. Gibson, A. B. Wong, L. Dou, J. Ma, L.-W. Wang, S. R. Leone, P. Yang. Lasing in robust cesium lead halide perovskite nanowires, *PNAS*, **113**, 1993–1998, 2016.
8. K. Sakimoto, A. B. Wong, P. Yang, Self-photosensitization of non-photosynthetic bacteria for artificial photosynthesis, *Science*, **351**, 74–77, 2016.
9. L. Dou*, A. B. Wong*, Y. Yu*, M. Lai, N. Kornienko, S. W. Eaton, A. Fu, C. G. Bischak, J. Ma, T. Ding, N. S. Ginsberg, L.-W. Wang, A. P. Alivisatos, P. Yang, Atomically Thin Two-dimensional Organic-inorganic Hybrid Perovskites, *Science*, **349**, 1518–1521, 2015.
10. A. B. Wong, M. Lai, S. W. Eaton, Y. Yu, E. Lin, L. Dou, A. Fu, P. Yang, Growth and Anion Exchange Conversion of $CH_3NH_3PbX_3$ Nanorod Arrays for Light-Emitting Diodes, *Nano Lett.*, **15**, 5519–5524, 2015.
11. A. B. Wong, S. Brittman, Y. Yu, N. P. Dasgupta, P. Yang, Core–Shell CdS–Cu_2S Nanorod Array Solar Cells, *Nano Lett.*, **15**, 4096–4101, 2015.

12. L. Zhang*, C. Liu*, A. B. Wong, J. Resasco, P. Yang, MoS_2-wrapped silicon nanowires for photoelectrochemical water reduction, *Nano Research*, **8**, 281–287, 2015.
13. D. Zhang, A. Wong, Y. Yu, S. Brittman, J. Sun, B. Brandon, A. P. Alivisatos, P. Yang, Phase-selective cation-exchange chemistry in sulfide nanowire systems, *JACS*, **136**, 17430–17433, 2014.
14. L. Zhang, K. Liu, A. B. Wong, J. Kim, X. Hong, C. Liu, T. Cao, S. G. Louie, F. Wang, P. Yang, Three-Dimensional Spirals of Atomic Layered MoS_2, *Nano Lett.*, **14**, 6418–6423, 2014.

Chapter 1

Synthesis and Epitaxy of Cu_2S-CdS Core-Shell Nanowires by Reverse Cation Exchange

1.1 Abstract:

Core-shell nanowires have many potential benefits for solar energy conversion, and cation exchange chemistry is one approach to achieve their synthesis. In this fundamental study, epitaxial Cu_2S-CdS core-shell nanowires were synthesized through a low-temperature cation exchange reaction applied to an array of Cu_2S nanowires. The direction of the reaction presented in this work is the reverse of the typical energetically favorable CdS to Cu_2S conversion, and this reversal of the reaction direction was achieved using a phosphine ligand in solution. Mechanistically, the CdS shell forms via the nucleation of islands of epitaxial CdS in the host Cu_2S nanowire. Although the nucleation of islands often results in polycrystalline products, these CdS islands eventually merge into a continuous, epitaxial, and single-crystalline shell of CdS on stoichiometric Cu_2S. This result represents a new principle for the use of cation exchange as a generalized synthetic approach.

1.2 Introduction:

Cation exchange has attracted increasing interest in recent years as a tool to synthesize complicated nanostructures that are not accessible by other synthetic routes.[1,2, 3, 4] The effective use of this synthetic technique to produce new structures requires an understanding of the mechanism of cation exchange. As the name implies, cation exchange refers to the replacement of the cations in the original crystal with cations from solution, which results in the formation of a new material composed of the original anion and the new cation. During the reaction, the original and product crystals meet in a reaction zone of several atomic layers between the two crystals.[1] The anion sublattice remains unchanged because the anion generally has reduced mobility as compared to the cation; therefore, the anion sublattice transmits shape and structural information to the newly formed crystal.[5] Moreover, particle size has important implications for the overall process of cation exchange. When particle size is on the order of several nanometers, the entire volume of a nanoparticle can be considered accessible to the cation, so exchange is not limited by solid-state cation diffusion.[1] This results in a rate of exchange exceeding that of bulk materials by several orders of magnitude. As particle size increases, it is interesting how accelerated rates of cation exchange gradually converge to the bulk rates that are limited by solid-state diffusion.[1,6,7] To obtain a deeper understanding of this, careful study of the progression of cation exchange on length scales beyond several nanometers should be performed to obtain new insights into the synthesis of nanowire and bulk materials by this technique.

Historically, *p*-type copper sulfide (Cu_2S) and *n*-type cadmium sulfide (CdS) is a classic material combination that is accessible with cation exchange. From the 1960’s through the 1980’s, cation exchange of CdS to Cu_2S attracted interest as an inexpensive method of producing solar cells, and rapid progress allowed efficiencies to approach 10%.[8] Partial cation exchange of CdS to

Cu_2S in nanorods and nanowires has also been recently reported for solar cell applications.[9,10] At the single-nanorod level, conversion of CdS produces an epitaxial axial junction between Cu_2S and CdS.[1,9,11] In contrast, at the single-nanowire level, (diameter > ~30 nm) solid-state diffusion of cations limits the reaction.[1,6,13] As a result, cation exchange of CdS nanowires produces a heteroepitaxial core-shell nanowire with a CdS core and a Cu_2S shell, and these core-shell nanowires have record open circuit voltages and fill factors for a CdS/Cu_2S photovoltaic device.[10] In addition, a vertical array of nanowires with this radial core-shell junction is attractive because it decouples the length scale for light absorption in Cu_2S (~1 μm) from the minority carrier diffusion length (~200 nm). In theory, this nanowire array geometry enables the creation of efficient photovoltaics from materials such as Cu_2S that are unsuitable for thin films.[14] Overall, three improvements that can be made to the previously reported single-nanowire system would be encapsulation of the Cu_2S to limit oxidation, thickening the Cu_2S shell, and using a vertical nanowire array for more efficient visible light absorption.

In all previous work, a host CdS crystal was converted to Cu_2S. In principle, the conversion of CdS to Cu_2S is thermodynamically favored by 118.6 kJ mol^{-1} in aqueous solution.[1] Although thermodynamically unfavorable, the reverse cation exchange reaction would enable Cu_2S nanowires to be converted to Cu_2S-CdS core-shell nanowires. This is beneficial because the volume proportion of the conductive Cu_2S light absorber can be maximized to improve photovoltaic efficiency, and the encapsulation of the core Cu_2S with the CdS shell can potentially improve the air stability of the Cu_2S.

In order to realize this Cu_2S-CdS core-shell structure, the chemistry to convert Cu_2S nanowires to CdS must be developed. Previously, it has been demonstrated that energetically favorable interactions of Cu^+ with a phosphine ligand in solution can provide the thermodynamic driving force to make a reverse cation exchange reaction proceed.[1,4, 15, 16] This reverse cation exchange reaction that converts Cu_2S nanowires to CdS using a phosphine ligand constitutes a new approach to a model material system by reversing the reaction's direction and by increasing its length scale when compared to nanorods. The Cu_2S-CdS nanowires formed by cation exchange have a radial junction as opposed to the axial junction found in nanorods because the reaction is limited by solid-state diffusion. As a result, the surface of the nanowire is converted before the interior of the nanowire, which promotes the formation of core-shell nanowires. Conceptually, the initial formation of the shell could proceed in one of several ways such as through homogeneous conversion of the surface, through island formation, or through homogeneous conversion with island formation.

In this fundamental study, the formation of the epitaxial CdS shell is found to begin as epitaxial CdS islands in the Cu_2S nanowire. These islands join together to form an epitaxial core-shell Cu_2S-CdS nanowire, which is a suitable morphology for photovoltaics. The study of the formation of the CdS shell presented here introduces the new principle that epitaxial island formation is a potential mechanism for cation exchange in nanowires.

1.3 Growth of Cu_2S Nanowires:

To grow Cu_2S nanowire arrays for conversion, the reaction of Cu with H_2S was chosen because this method provides a scalable and inexpensive synthesis of Cu_2S nanowires suitable for solar energy conversion. Cu foil was placed into a 1 liter glass reactor with an atmosphere of H_2S/air at ambient temperature, which was similar to previous reports of Cu_2S nanowire array growth.[17, 18, 19] After 12 hours, the Cu substrate turned black because of the formation of the Cu_2S nanowire array, and these Cu_2S nanowires were kept under N_2 prior to the reverse cation exchange reaction. The nanowire size varied according to the H_2S:Cu ratio and the reaction time. Clusters of exceptionally long wires were observed, as in previous reports (Figure 1-3).[19] The smaller nanowires that covered the majority of the substrate were tapered with tips around 100 nm in diameter and lengths on the order of 1 µm (Figure 1-1a). As seen by high resolution transmission electron microscopy (HRTEM), the fresh Cu_2S nanowires were found to be crystalline and to have clean surfaces suitable for cation exchange (Figure 1-1b). Selected area electron diffraction (SAED) showed the single-crystallinity of the Cu_2S nanowires made by this method, and the phase was indexed to monoclinic low chalcocite Cu_2S (Figure 1-1b, inset). The monoclinic low chalcocite Cu_2S nanowires grew in the [-204] direction, which corresponds to the c-axis of hexagonal high chalcocite Cu_2S, in agreement with previous reports.[19, 20] The pure monoclinic low chalcocite phase of the Cu_2S nanowires was also confirmed by powder x-ray diffraction (XRD) (Figure 1-4).

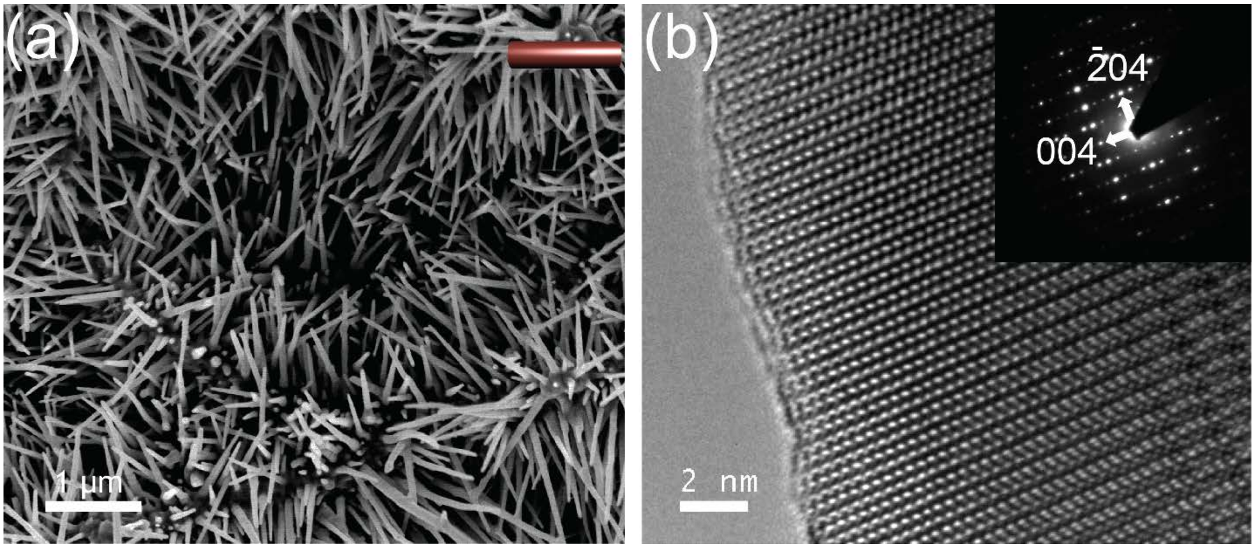

Figure 1-1. Characterization of Cu_2S nanowires used as the starting material for the reverse cation exchange reaction. (A) Scanning electron microscopy (SEM) image of a Cu_2S nanowire array grown on Cu foil. (B) High resolution transmission electron microscopy (HRTEM) image of a low chalcocite Cu_2S nanowire with inset SAED pattern showing the crystallinity of the nanowires. Nanowires characterized shortly after exposure to air exhibit clean surfaces, which are suitable for cation exchange.

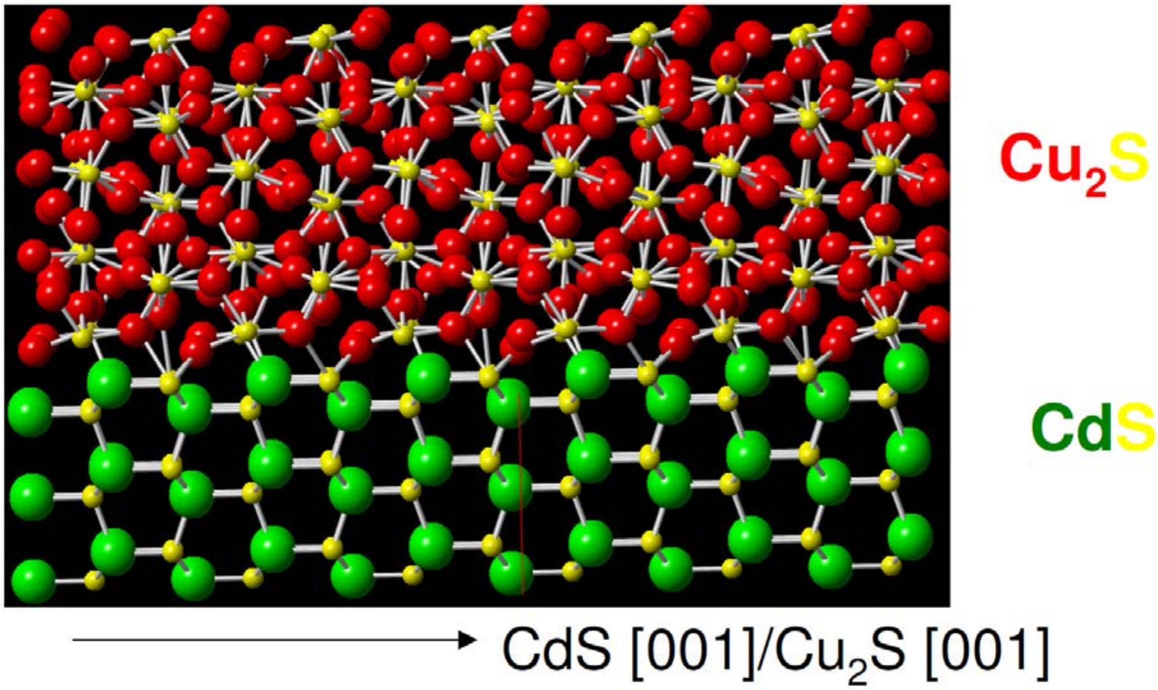

Figure 1-2. Cluster of CdS and Cu$_2$S showing the continuity of the sulfur anion sublattice at a heteroepitaxial CdS-Cu$_2$S interface. Structural model is based on the unit cell of CdS and Cu2S with no strain relaxation. Although Cu$_2$S has a monoclinic unit cell while CdS has a hexagonal unit cell and a wurtzite structure, the hexagonal sulfur CdS sublattice is very similar to the quasihexagonal Cu$_2$S sulfur sublattice.

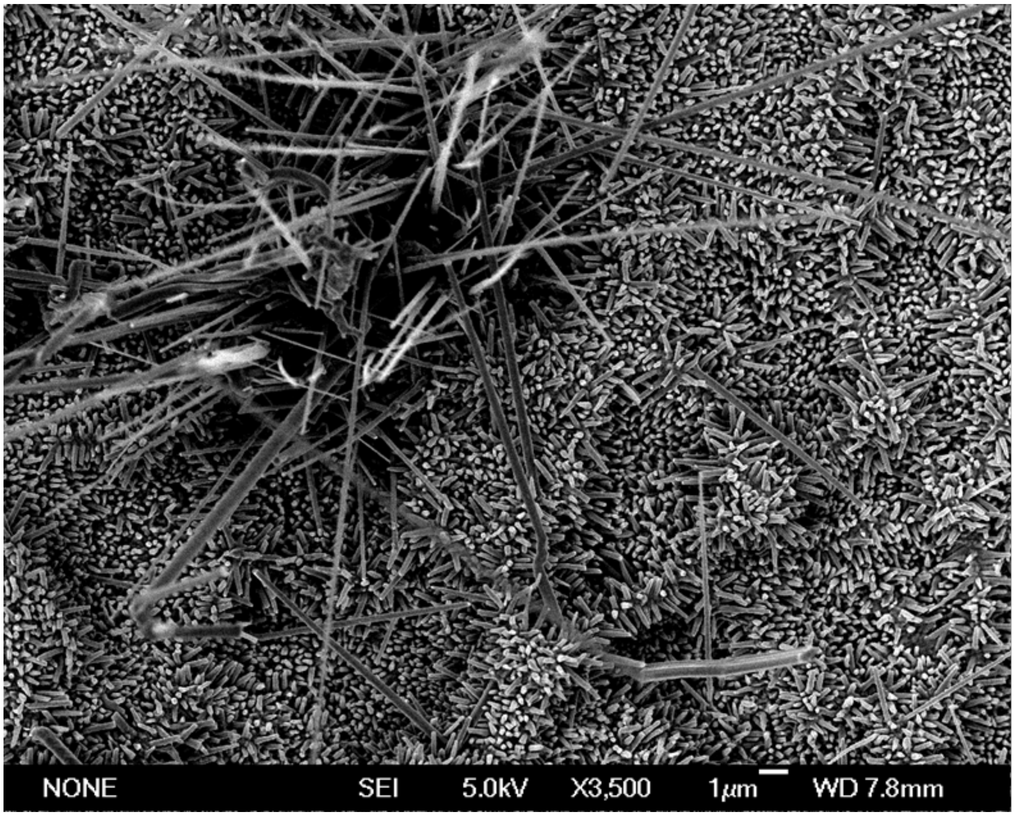

Figure 1-3. Low magnification SEM image of Cu_2S nanorod array showing the growth of long Cu_2S nanowires in certain regions of the Cu substrate.

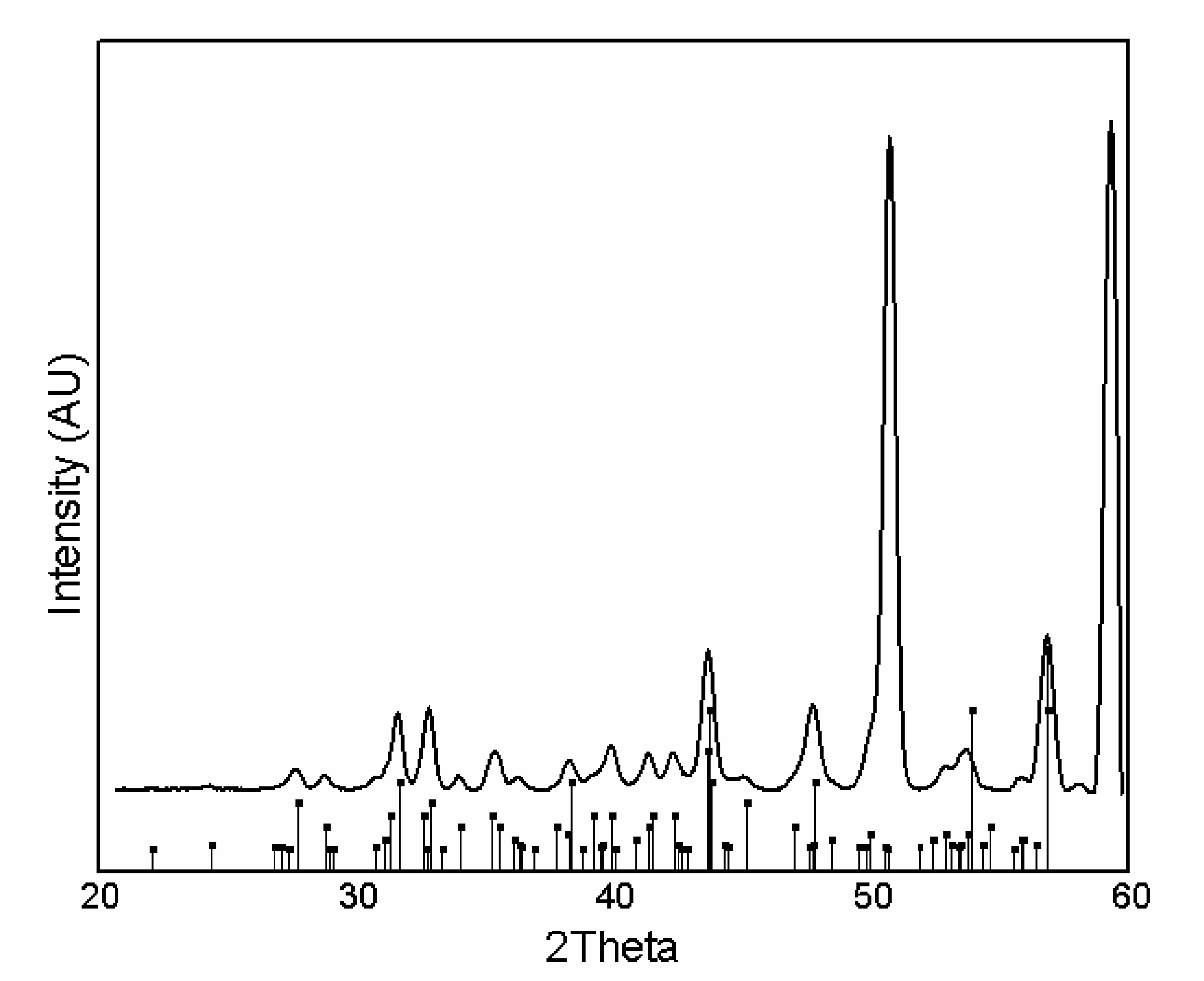

Figure 1-4. XRD pattern of Cu_2S (ICSD: 01-073-6145) nanowire array on Cu foil substrate. The Cu foil accounts for the strong signal at 50 and 59 degrees.

1.4 Conversion to Cu_2S-CdS Core-Shell Nanowires:

The Cu_2S nanowire arrays were subsequently converted to Cu_2S-CdS core-shell structures by soaking them in an organic solution of oleylamine, 1-octadecene, and trioctylphosphine with cadmium acetate at 40 °C under a N_2 atmosphere. Trioctylphosphine was chosen to drive the conversion of Cu_2S to CdS. Based on Pearson's hard soft acid base theory, different Lewis acids and bases are classified by their hardness, η. In general, soft-soft and hard-hard interactions are favored over hard-soft interactions, which means that phosphine ligands ($\eta = \sim 6$) will have stronger interactions with Cu^+ ($\eta = 6.28$ eV) than with Cd^{2+} ($\eta = 10.29$ eV).[1, 21] Despite an energy barrier of 118.6 kJ mol^{-1} in aqueous solution, the favorable interactions between the Cu^+ and the trioctylphosphine allow this Cu_2S to CdS conversion to proceed. After the reaction, the nanowire morphology was preserved (Figure 1-5a), which is a hallmark of cation exchange in large crystals. The relatively small size of the reaction zone as compared to that of the crystal allows the anionic framework to be conserved during cation exchange. In addition, the XRD pattern of the Cu_2S-CdS core-shell nanowires (Figure 1-5b) shows strong peaks for CdS, which indicates that CdS has formed from the Cu_2S because there is no other source of sulfur in the reaction. The XRD pattern also shows that the phase is unchanged in the unreacted Cu_2S in the core, and no copper-deficient phases are formed despite the removal of Cu^+ cations during the reaction.

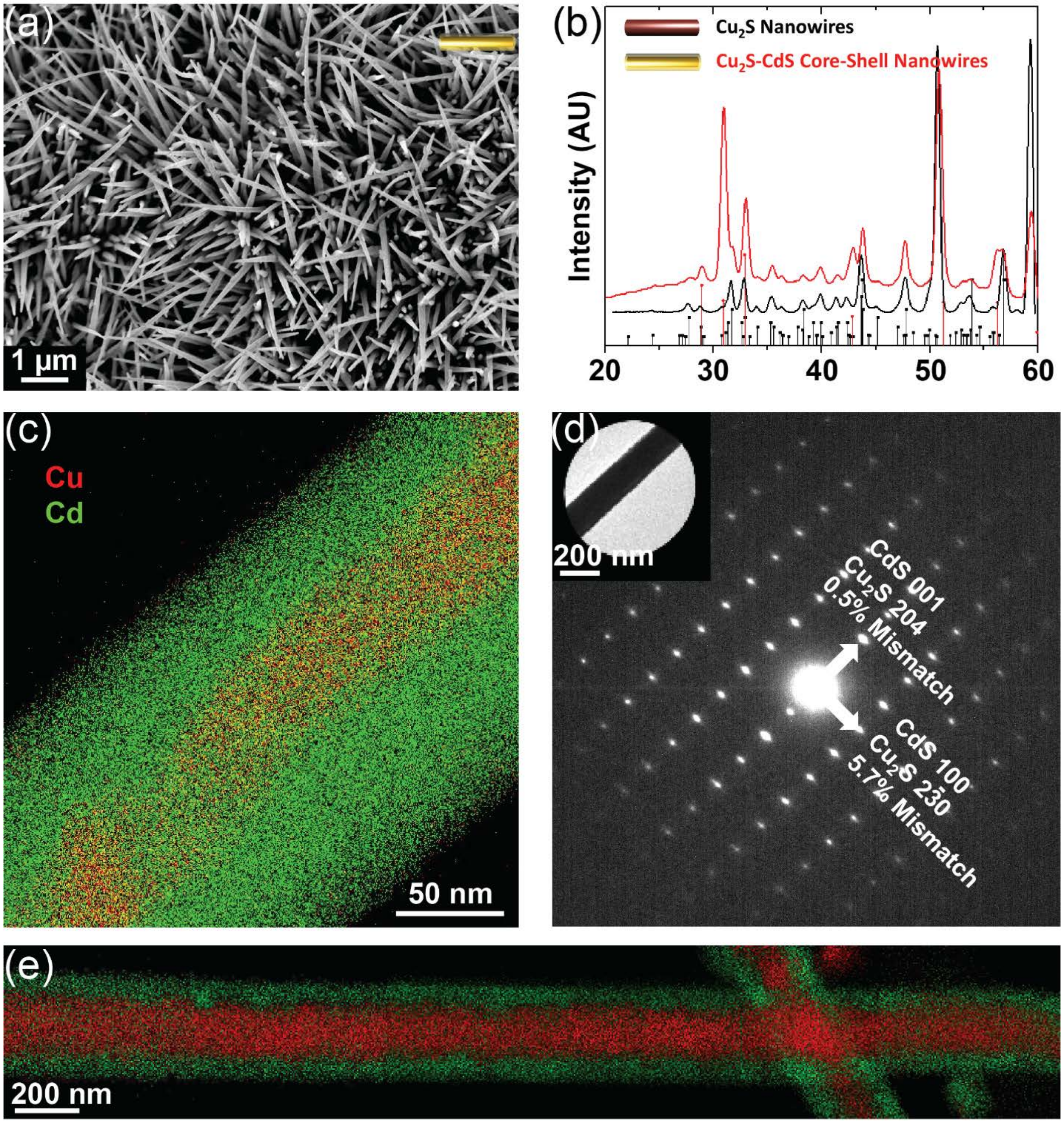

Figure 1-5. Structural characterization of core-shell Cu_2S-CdS nanowires. (A) SEM image of Cu_2S-CdS core-shell nanowire array showing the preservation of nanowire morphology after the reaction. (B) XRD spectra of Cu_2S nanowire array (black) and Cu_2S-CdS core-shell nanowire array on Cu substrate (red). XRD patterns of low chalcocite Cu_2S (black) and CdS (red) are shown for

comparison. The XRD spectrum of the core-shell nanowires shows the preservation of all peaks associated with the low chalcocite phase of Cu_2S after the introduction of crystalline CdS. (C) EDS mapping of core-shell nanowire after conversion in reverse cation exchange conditions for 120 hours. Cd counts are shown in green while Cu counts are shown in red. (D) SAED pattern of the same core-shell nanowire shown in (C) with the area of the nanowire selected shown in the inset. The SAED pattern shows the epitaxial formation of CdS onto the Cu_2S nanowire. (E) EDS mapping of Cu_2S-CdS core-shell nanowire over a length of several microns with Cd (green) and Cu (red). Image was assembled from multiple scans along the length of the nanowire to show the continuity of the CdS shell.

1.5 Structural Characterization of Cu_2S-CdS Core-Shell Nanowires:

To identify and characterize the structure of CdS on the Cu_2S core, energy dispersive x-ray spectroscopy (EDS) mapping and SAED were performed. For nanowires with diameters greater than 200 nm, the EDS maps consistently show a clear Cu_2S-CdS core-shell structure (Figure 1-5c), which is also reflected in the EDS line scans (Figure 1-6). The Cu_2S-CdS nanowires have a core-shell geometry and a radial interface instead of the axial interface previously observed in Cu_2S/CdS nanorods in the forward cation exchange reaction.[1,9,11] In nanoparticles with diameters of several nanometers, cations can easily diffuse across the entire nanoparticle, but in thick nanowires, solid-state diffusion limits the cation exchange, which will reduce the rate of the penetration of CdS into the Cu_2S nanowire. This situation favors the formation of a radial core-shell geometry.[1,6] The SAED pattern of the same nanowire shown in figure 1-5c is shown in figure 1-5d, which proves that the region used to make the SAED pattern contains a core-shell structure. The simplicity of the SAED pattern is explained by the heteroepitaxy of the Cu_2S/CdS interface. The epitaxial relationship of CdS and Cu_2S shown here is: CdS[001] ∥ Cu_2S[-204], and CdS[100] ∥ Cu_2S[2-30], and these orientations have a lattice mismatch of 0.5% and 5.7%, respectively (Figure 1-5d). The large area selected for SAED demonstrates that the shell is both single-crystalline and epitaxial to the core of the nanowire along the nanowire's length. HRTEM images of the shell also confirm that the shell is single-crystalline (Figure 1-7). A constructed EDS map of a core-shell CdS-Cu_2S nanowire after conversion for over 40 hours also shows the continuity of the CdS shell over several micrometers of the nanowire (Figure 1-5e). Collectively, these data demonstrate that a Cu_2S-CdS core-shell nanowire morphology has been produced. Their radial heteroepitaxial interface over the length of the nanowire has been achieved using a reverse cation exchange reaction under mild temperatures to form a single-crystalline CdS shell.[1]

---

[1] Initial attempts were made to use these core-shell Cu_2S-CdS nanowires as single-nanowire solar cells. Although devices exhibited rectifying current-voltage characteristics, these devices reversibly switch between conductive and resistive states under applied bias, and this rectifying memristor behavior is similar to previous reports.[22]

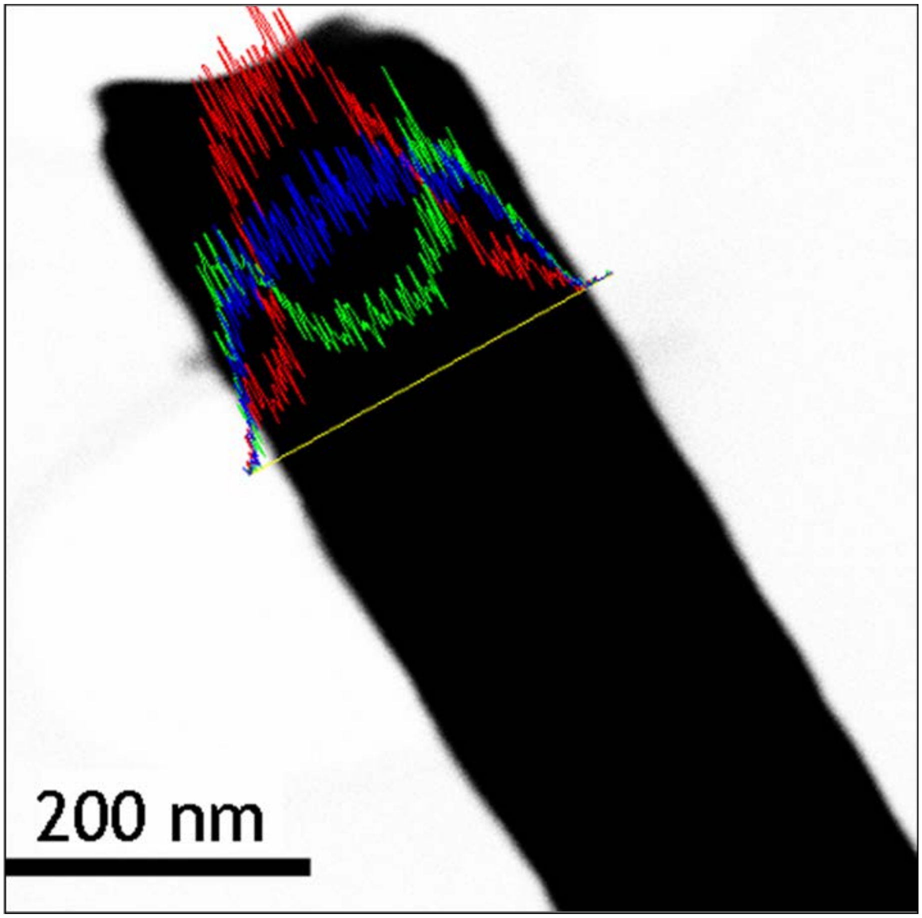

Figure 1-6. EDS line scan showing Cu (red) core and Cd (green) shell morphology. The S (blue) signal is present along the diameter of the wire. The reduction of Cd signal in the middle of the nanowire at the same point at the increase in the Cu signal provide strong evidence for the presence of a core-shell structure.

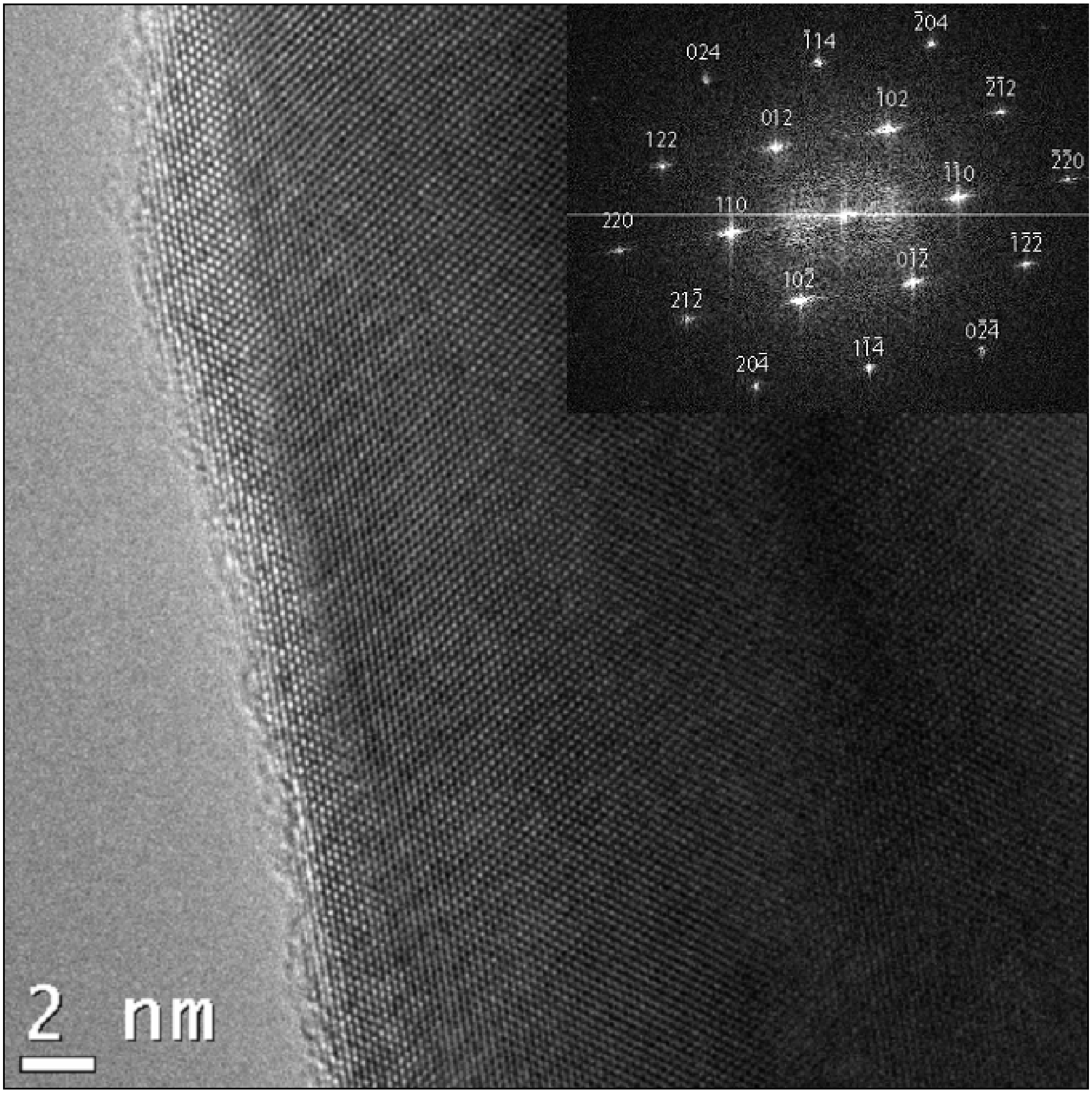

Figure 1-7. HRTEM image of crystalline CdS shell formed at 40°C. Inset shows FFT of fringes on CdS, which can be indexed to crystalline CdS.

1.6 Insights into the Shell Formation Mechanism by High Resolution Transmission Microscopy:

To obtain further insight into the mechanism of the formation of the CdS shell, partially converted nanowires were studied by HRTEM, which showed that the cation exchange does not occur uniformly over the surface of the nanowire. After 1 hour of conversion, many areas of the nanowire show an identical fringe pattern to the inset FFT, which corresponds to Cu_2S at the nanowire's surface (Figure 1-8a). On the same nanowire, a small region contains an inclusion of CdS that has nucleated into the Cu_2S host material (Figure 1-8b). The difference in the crystal structure between CdS and the Cu_2S regions is emphasized by the FFT insets. This shows that the formation of the CdS in the Cu_2S nanowire by cation exchange is epitaxial from the initial stages of conversion. Small regions of CdS nucleate inside the nanowire at the surface with each CdS region having its own reaction zone and epitaxial interface. Figure 1-8c shows the lattice fringes of the first several nanometers of a nanowire after 3 hours of conversion. In this region, the fringes correspond to the crystal structure of CdS, which demonstrates the crystallinity of the CdS that formed under mild conditions. The difference in the lattice fringes is due to the interface between CdS and Cu_2S. To confirm this, the same position on the same nanowire was visualized by HRTEM and mapped with EDS (Figures 1-8d, 1-8e). The Cd- and Cu-rich regions to the left and right, respectively, in the EDS map correspond well to the CdS and Cu_2S fringes in the HRTEM image. These data show that cation exchange can produce structures with epitaxial materials embedded in the surface of the host nanowire en route to the formation of a core-shell nanowire. This epitaxial particle in a nanowire is a complex structure that is difficult to obtain by direct seeded growth, and it is reminiscent of Janus particles. As time progresses these epitaxial CdS inclusions eventually form the continuous CdS shell as each inclusion penetrates deeper into the CdS nanowire (Figure 1-8f). By measuring the shell's thickness dependence on the square root of time, an effective diffusion coefficient corresponding to the depth of the CdS/Cu_2S interface is calculated to be $D \sim 10^{-17}$ cm^2 s^{-1}. This is calculated based on the approximation of the solid-state diffusion in the nanowire as 1-D diffusion along the radius.

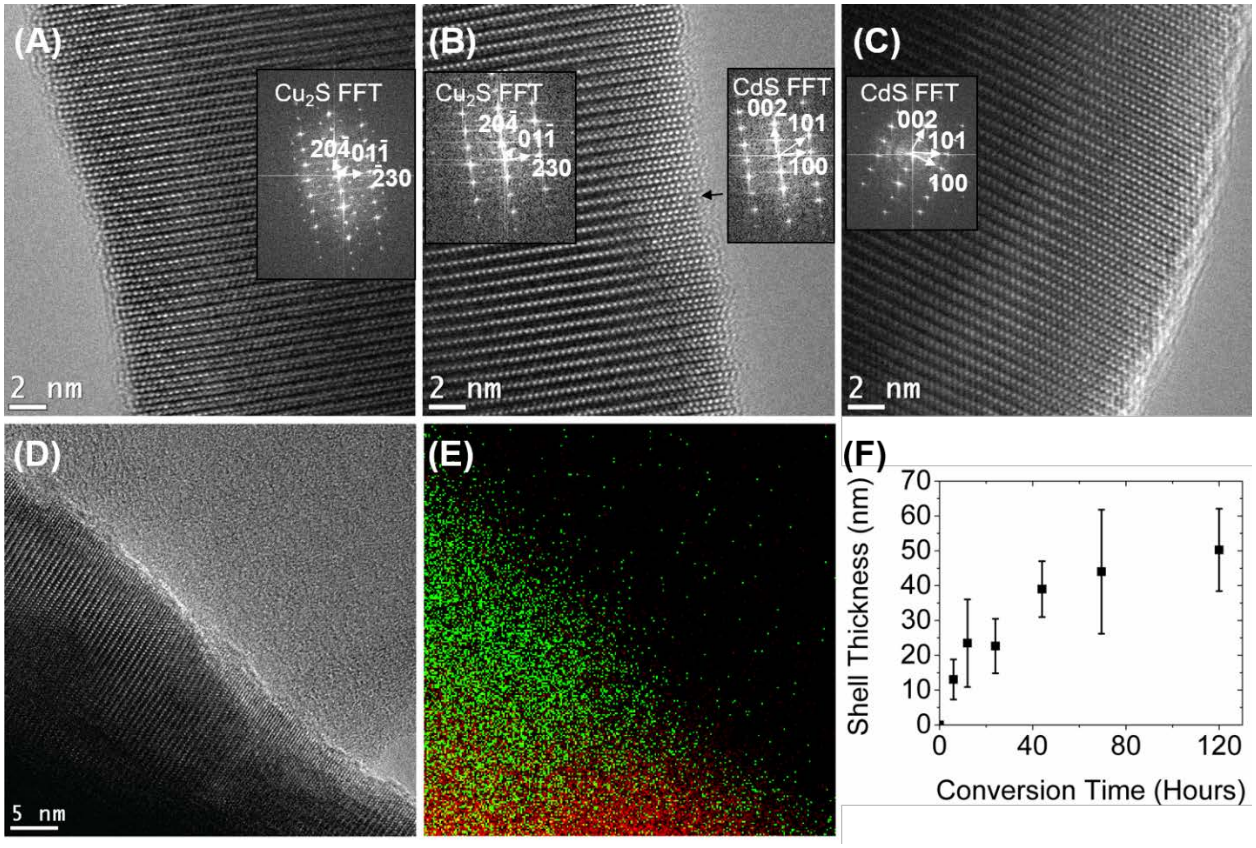

Figure 1-8. Formation of CdS in Cu_2S nanowires during reverse cation exchange. (A) HRTEM image of a nanowire after 1 hour of exposure to reverse cation exchange conditions. The area imaged corresponds to the crystal structure of Cu_2S as shown in the inset FFT pattern. (B) HRTEM image of the same nanowire as in (a) showing an area of epitaxial CdS formation within the Cu_2S. The inset FFT patterns show the Cu_2S structure inside the nanowire and the CdS structure at the edge of the nanowire near the center of the image. (C) HRTEM of a nanowire after cation exchange for 3 hours. The area visible can be indexed to CdS as shown in the inset FFT. (D) HRTEM pattern of a nanowire after 1 hour of reverse cation exchange showing regions of Cu_2S and CdS at the surface. (E) EDS mapping of the same region as in (D) on the same scale bar indicating the correspondence between the changes in the lattice fringes and the chemical composition of the nanowire. (F) Average shell thickness of the CdS measured by EDS line scans at increasing conversion time for nanowires with an average diameter between 250 and 260 nanometers. Error bars show the standard deviation of the measurements.

The progression of the individual epitaxial CdS inclusions as they join to form a continuous heteroepitaxial shell can be tracked by EDS mapping, and this analysis shows that the nanowire's size is an important consideration. CdS forms by nucleating at different areas in the surface of the Cu_2S nanowire after 1 hour of conversion (Figure 1-9). By 3 hours into the reaction, these domains have become significantly larger, so CdS covers much of the nanowire's surface. By 24 hours, the coverage of the nanowire's surface is nearly complete. Overall, this study of the formation of the heteroepitaxial Cu_2S-CdS core-shell nanowires has yielded new insights into the mechanism of cation exchange that can help to inform the synthesis of new heterostructured nanowire materials.

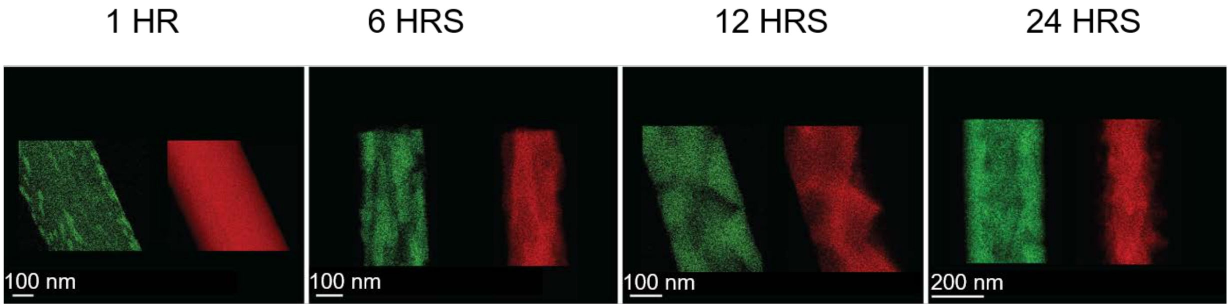

Figure 1-9. Progression of the CdS islands into a CdS shell. EDS maps for nanowires after 1, 6, 12, and 24 hrs of CdS conversion. Cd (green) is shown on the left while Cu (red) is shown in the right for each nanowire. The isolated regions of CdS eventually merge together into an epitaxial shell of CdS on the Cu_2S core.

1.7 Chapter 1 Conclusions:

Cation exchange for nanomaterial synthesis offers a way to synthesize materials that are not accessible by other means. Using a reverse cation exchange reaction, Cu_2S nanowires were converted into Cu_2S-CdS core-shell nanowires, which possessed a heteroepitaxial interface and a continuous single-crystalline shell. As the reaction proceeds, CdS nucleates as epitaxial islands embedded within the Cu_2S. This work elucidates epitaxial thin film growth during cation exchange.

1.8 Chapter 1 Methods:

Cu_2S Nanowire Growth. Cu_2S nanowires were synthesized in a 1 L glass reactor containing a smaller cylinder charged with 1.4 g sodium sulfide hydrate (≥ 60% scales, Aldrich). 1 cm^2 of Cu foil (thickness 0.025 mm, 99.98% trace metals basis, Aldrich) was preoxidized in a 0.1 M ammonium persulfate (≥ 98%, Acros) aqueous solution for at least 6 hours to clean and oxidize the surface. The Cu foil was quickly washed 3 times in deionized water and dried. The Cu foil was placed in the sealed glass reactor inside a fume hood for Cu_2S nanowire growth, which was initiated by the addition of 4 mL of 3 M HCl to the sodium sulfide through a septum. The double replacement reaction between sodium sulfide and HCl formed H_2S gas in situ. The Cu foil darkened as it began to react with the H_2S, with the substrate eventually becoming black. After 12 to 36 hours, the glass cylinder was purged, and the H_2S gas passed through several bubblers with ZnO suspensions to deactivate it before exiting the apparatus. After 1 hour of N_2 purging, the Cu_2S nanowire array was removed from the glass reactor and stored in N_2.

Reverse Cation Exchange Reaction. The solution for reverse cation exchange was prepared by combining 1.0 g cadmium acetate dihydrate (≥ 98% purum, Aldrich), 0.7 mL oleylamine (70% technical, Aldrich), and 0.7 1-octadecene (90% technical, Aldrich). When the solution had stabilized at a temperature of 40°C, 1.4 mL of trioctylphosphine (≥ 90%, Fluka) was quickly added along with the Cu_2S nanowire array. The reverse cation exchange solution was kept under a N_2 atmosphere. The reaction was allowed to proceed for the desired time with continuous CdS shells being found on all wires after 44 hours of reverse cation exchange. To stop the reaction, the core-shell nanowire arrays were removed and soaked in toluene for several minutes and then repeatedly rinsed in a sequence of toluene, isopropanol, water, and isopropanol ten times. After reverse cation exchange, samples were stored under N_2.

Electron Microscopy Characterization. SEM images were taken using a JEOL JSM-6340F field emission scanning electron microscope. XRD patterns were acquired using a Bruker AXS D8 Advance diffractometer, which used Co Kα radiation with a wavelength of 1.79026 Å. EDS maps were taken using a JEOL JEM-2100 LaB6 microscope at 200 kV. The microscope was equipped with an Oxford EDS detector, which was used to map the CdLα and CuKα energies. The EDS map over several microns of the core-shell nanowire was constructed by mapping the nanowire multiple times along its length at a high magnification to produce sufficient spatial resolution to determine if the CdS shell is continuous over the length of the nanowire. These EDS maps were combined, and together they show that the CdS shell is continuous on the Cu_2S core along the length of the nanowires after conversion for over 40 hours. EDS maps for the time evolution of the shell formation were also taken on a FEI Titan microscope operated at 80 kV at the National Center for Electron Microscopy. The microscope was equipped with a FEI Super-X Quad windowless detector based on silicon drift technology controlled by Bruker Esprit software. HRTEM images were also taken on a FEI Tecnai F20 U-Twin microscope that was operated at 200kV at the National Center for Electron Microscopy.

1.9 Chapter 1 References:

1. Beberwyck, B. J.; Surendranah, Y.; Alivisatos A. P. *J. Phys. Chem. C* **2013**, 117, 19759-19770.
2. Rivest, J. B.; Jain P. K. *Chem. Soc. Rev*. **2013**, 43. 89-96.
3. Deka, S.; Miszta, Km.; Dorfs, D.; Genovese, A.; Bertoni, G.; Manna, L. *Nano Lett*. **2010**, 10, 3770-3776.
4. Li, H.; Zanella, M; Genovese, A.; Povia, M. Falqui, A. Giannini, C.; Manna, L. *Nano Lett*. **2011**, 11, 4964-4970.
5. Putnis, A. *Mineral. Mag*. **2002**, 66, 689−708.
6. Zhang, B.; Jung, Y.; Chung, H. S.; Vugt, L. V.; Agarwal, R. *Nano Lett.* **2010**, 10, 149-155.
7. Dorn, A.; Allen, P. M.; Harris, D. K.; Bawendi, M. G. *Nano Lett*. **2010**, 10, 3948-3951.
8. Bragagnolo, J. A.; Barnett, A. M.; Phillips, J. E.; Hall, R. B.; Rothwarf, A.; Meakin, J. D. *IEEE Trans. Electron Devices* **1980**, 27, 645-651.
9. Rivest, J. B.; Swisher, S. L.; Fong, L. K.; Zheng, H.; Alivisatos A. P. *ACS Nano* **2011**, 5, 3811-3816.
10. Tang, J.; Huo, Z.: Brittman, S; Gao, H.; Yang, P. *Nat. Nanotechnol*. **2011**, 6, 568-572.
11. Sadtler, B.; Demchenko, D. O.; Zheng, H.; Hughes, S. M.; Merkle, M.G.; Dahmen, U.; Wang, L.W.; Alivisatos, A.P. *J. Am. Chem. Soc*. **2009**, 131, 5285-5293.
12. Zheng, H.; Rivest, J. B.; Miller, T. A.; Sadtler, B.; Lindenberg, A.; Toney M. F.; Wang, L. W.; Kisielowski, C.; Alivisatos, A. P. *Science* **2011**, 333, 206-209.
13. Dorn, A.; Allen, P. M.; Harris, D. K.; Bawendi, M. G. *Nano Lett*. **2010**, 10, 3948-3951.
14. Dasgupta, N. P.; Sun, J.; Liu, C.; Brittman, S.; Andrews, S. C.; Lim, J.; Gao, H.; Yan, R.; Yang, P. *Adv. Mater*. **2014**, 26, 2137-2184.
15. Son, D. H.; Hughes, S. M.; Yin, Y.; Alivisatos, A. P. *Science* **2004**, 306, 1009-1012.
16. Luther, J. M.; Zheng, H.; Sadtler, B.; Alivisatos, A. P. *J. Am. Chem. Soc*. **2009**, 131, 16851-16857.
17. Zhang, W.; Wen, X.; Yang, S. *Langmuir* **2003**, 19, 4420-4426.
18. Wang, N.; Fung, K. K.; Wang, S.; Yang, S. *J. Cryst. Growth* **2001**, 233, 226-232.
19. Liu, X.; Mayer, M. T.; Wang, D. *Angew. Chem., Int. Ed*. **2010**, 49, 3165-3168.
20. Wang, S.; Guo, L.; Wen, X.; Yang, S; Zhao, J.; Liu, J.; Wu, Z. *Mater. Chem. Phys*. **2002**, 75, 32-38.
21. Pearson, R. G. *Inorg. Chem.* **1988**, 27, 734-740.
22. Liu, X.; Mayer, M. T.; Wang, D. *Appl. Phys. Lett*. **2010**, 96, 223103.

Chapter 2

Core-Shell CdS-Cu_2S Nanorod Array Solar Cells

2.1 Abstract:

As an earth-abundant *p-type* semiconductor, copper sulfide (Cu_2S) is an attractive material for application in photovoltaic devices. However, it suffers from a minority carrier diffusion length that is less than the length required for complete light absorption. Core-shell nanowires and nanorods have the potential to alleviate this difficulty because they decouple the length scales of light absorption and charge collection. To achieve this geometry using Cu_2S, cation exchange was applied to an array of CdS nanorods to produce well-defined CdS-Cu_2S core-shell nanorods. Previous work has demonstrated single-nanowire photovoltaic devices from this material system, but in this work, the cation exchange chemistry has been applied to nanorod arrays to produce ensemble-level devices with micro-scale sizes. The core-shell nanorod array devices show power conversion efficiencies of up to 3.8%. In addition, these devices are stable when measured in air after nearly one month of storage in a desiccator. These results are a first step in the development of large-area nanostructured Cu_2S-based photovoltaics that can be processed from solution.

2.2 Introduction:

The development of new renewable energy technologies such as photovoltaics for solar energy conversion is an area of considerable interest. From the 1960's through the 1980's, one major approach to produce scalable photovoltaics was the development of thin film CdS/Cu_2S solar cells. In these photovoltaics, the Cu_2S layer serves as an earth-abundant light absorber with an indirect band gap of 1.2 eV,[1] which corresponds to a maximum theoretical efficiency of 30%.[2] To form the heterojunction, the partial conversion of *n*-type cadmium sulfide (CdS) thin films to form *p*-type copper sulfide was performed though a solution phase or solid state cation exchange reaction. In cation exchange, the cations in an initial crystal are replaced with new cations that diffuse into the material from solution. In many cases, the anion lattice is conserved, which allows the initial morphology to be preserved after the reaction.[3-5] This cation exchange chemistry was thought to be a promising route to produce inexpensive and scalable solar cells despite a mismatch between the length scales required for light absorption (~6 µm at 1000 nm for 90% absorption) and diffusion of minority carriers within the Cu_2S (~300 nm).[6] Despite this limitation, rapid progress allowed cell efficiencies to approach 10%,[7] which made this technology competitive with planar silicon-based photovoltaics at the time.[8] Before 1980, the record efficiency for multicrystalline silicon solar cells was only ~15.3%.[9] However, interest in CdS/Cu_2S waned during the 1980's because of the continued progress of Si solar cells as well as concerns about the long-term stability of CdS/Cu_2S solar cells. Mechanistically, the degradation in performance was thought to occur by the diffusion of Cu^+ into CdS, particularly along grain boundaries, and by oxidation of the Cu_2S at the surface to form non-stoichiometric phases of copper sulfide. [10-12] Recently, there has been progress in the stabilization of Cu_2S for light-harvesting applications through the use of Al_2O_3 protection layers deposited by atomic layer deposition (ALD), [8,12] which partially addresses the stability issues that were previously encountered.

To improve the performance of CdS/Cu_2S solar cells, the core-shell nanowire array geometry is an ideal structure to resolve the mismatch between the short length scale for minority carrier diffusion and the longer length scale for light absorption in Cu_2S by decoupling these directions.[13,14] In addition, nanowires also offer advantages in terms of low optical reflectivity, light trapping, and the potential for flexible, inexpensive, and industrially scalable solar cells.[13,15-22] These advantages may eventually lead to the overall goal of efficient and scalable solution-processed solar cells.

Moreover, core-shell nanowire and nanorod arrays create the opportunity for the synthesis of precise and well-controlled junctions for solar energy conversion. For these reasons, work on Cu_2S and CdS has drawn renewed interest. Cation exchange can produce precisely controlled heteroepitaxial CdS/Cu_2S axial and core-shell junctions in thin nanorods (<15 nm) and nanowires respectively.[14,23,24] These axial nanorod and single nanowire core-shell heteroepitaxial junctions of single-crystalline Cu_2S and CdS have photovoltaic properties without the disadvantage of diffusion along grain boundaries.[14,25] At the level of a single nanowire, $CdS\text{-}Cu_2S$ core-shell photovoltaic devices exhibited a record open circuit voltage (0.61 V) and fill factor (80.8%) compared to all previous Cu_2S/CdS photovoltaics. These values were attributed to the high quality of the CdS/Cu_2S junction formed by performing cation exchange on a single-crystalline CdS wire grown by the vapor-liquid-solid (VLS) mechanism. The $CdS\text{-}Cu_2S$ core-shell interface was structurally well defined and heteroepitaxial.[14] Despite this excellent performance, this work presented several new challenges. First, the power output of a single nanowire solar cell is limited; therefore, the assembly of the core-shell nanowires into a scalable device is critical. Second, the shell thickness in these solar cells reached only about 20 nm, which limited the light absorption in the Cu_2S beyond 510 nm and limited short-circuit current densities. To address these challenges, cation exchange chemistry was applied to CdS nanorod arrays patterned with microscale windows to produce solution-processed photovoltaic devices featuring well-defined *p-n* junctions. This approach yields ensemble-level devices in contrast to the previous single-nanowire devices. The vertical array of core-shell nanorods addresses the issue of the mismatched length scales for light absorption and minority carrier diffusion in thin film CdS/Cu_2S devices by decoupling them. Within this vertically oriented array, the Cu_2S shell thickness exceeds 60 nm, which has improved short circuit current density as compared to the previous work on single core-shell nanowires. The micro-scale array devices reach a maximum efficiency of 3.8% and maintain this efficiency after at least one month of storage.

2.3 CdS Nanorod Array Synthesis:

As the CdS substrate for cation exchange, wurtzite CdS nanorods were grown on indium tin oxide (ITO) or fluorine-doped tin oxide (FTO) by modifying a previously reported hydrothermal method.[26,27] At the single nanorod level, transmission electron microscopy (TEM) and selected area-electron diffraction (SAED) images demonstrate that the nanorods are grown along the c-axis and are single crystalline, which is beneficial for forming a high-quality junction via cation exchange (Figure 2-1a). Typical nanorods have diameters of 200 to 300 nm and average lengths exceeding 600 nm (Figures 2-1a, 2-1b, 2-1c). The vertical CdS nanorods sit on top of a dense buffer layer that covers the FTO substrate.

2.4 Cation Exchange to form CdS-Cu_2S Core-Shell Structures:

Before fabricating the solar cells, cation exchange on the CdS nanorods was found to be able to convert them into Cu_2S either fully or partially, depending on the reaction conditions. Briefly, CdS nanorods were dipped into an aqueous solution of CuCl at 90°C. By controlling reaction time, the synthesis of uniform core-shell nanorods can be achieved through this method, as demonstrated by energy dispersive X-ray spectroscopy (EDS) (Figure 2-1d). The SAED pattern of a single core-shell CdS-Cu_2S nanorod indicates to formation of crystalline Cu_2S on the CdS shell (Figure 2-1e). The splitting of the CdS and Cu_2S diffraction spots in the SAED image is due to the difference in d-spacing between the CdS and Cu_2S, and this splitting is an indication of a heteroepitaxial relationship between the CdS in the core and the Cu_2S in the shell in agreement with prior work on core-shell CdS-Cu_2S nanowires. These previous studies have shown that this method of dipping single-crystalline CdS nanowires into the heated aqueous solution forms a heteroepitaxial interface between the CdS core and the rapidly-grown Cu_2S shell.[14,28]

In addition to the formation of core-shell structures, the phase of copper sulfide produced from CdS is also important. It has been shown previously that substoichiometric phases of copper sulfide can be formed from CdS, such as roxbyite ($Cu_{1.74\text{-}1.82}S$) and djurleite ($Cu_{1.97\text{-}1.93}S$), in addition to stoichiometric low chalcocite (Cu_2S).[24] Planar photovoltaic devices made from copper-deficient phases exhibited lower current densities than devices produced with stoichiometric Cu_2S, and this poorer performance is caused by adverse changes in the absorption coefficient, minority carrier diffusion length, mobility, and band gap with increasing copper deficiency.[29] As is demonstrated by X-ray diffraction (XRD) in Figure 2-1f, the core-shell CdS-Cu_2S nanorods formed by cation exchange consist of stoichiometric Cu_2S of the low chalcocite phase, which is most suitable for photovoltaics.

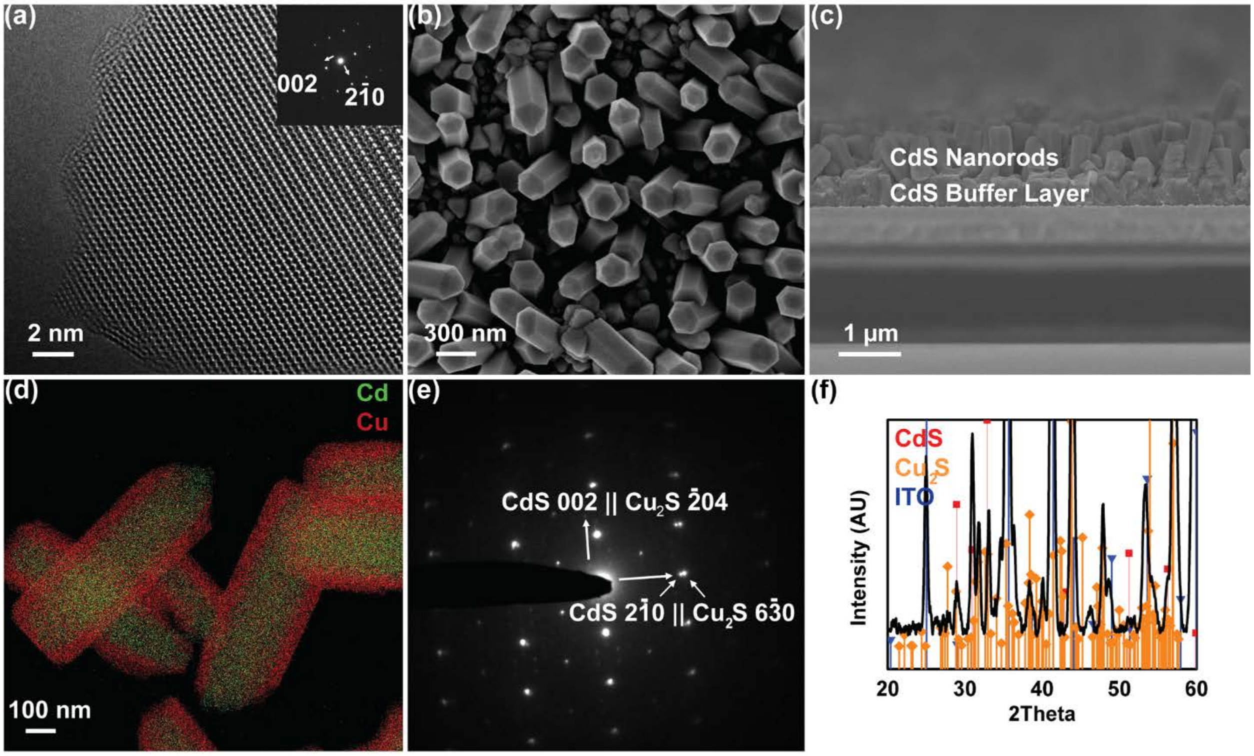

Figure 2-1. Characterization of the CdS nanorods used for the cation exchange reaction and Cu_2S after conversion of CdS nanorods. (a) HRTEM image of an individual CdS nanorod with inset diffraction pattern. (b) Top-view SEM image of a CdS nanorod array. (c) Cross-sectional SEM image of a CdS nanorod array showing the interface with the underlying FTO substrate. (d) Energy dispersive X-ray spectroscopy (EDS) images of partially converted CdS-Cu_2S nanorods synthesized under the same conditions used for photovoltaic devices. Cadmium is shown in green, and copper is shown in red. (e) Selected area diffraction pattern of a core-shell CdS-Cu_2S nanorod. (f) X-ray diffraction pattern of CdS-Cu_2S core-shell nanorods indicating the presence of wurtzite CdS (red squares) as well as low-chalcocite Cu_2S (orange diamonds). Diffraction peaks from ITO substrate are also shown (blue triangles).

2.5 Fabrication of Photovoltaic Devices:

Core-shell nanorod array photovoltaic devices were then fabricated using the CdS-Cu_2S cation exchange reaction as shown in Figure 2-2a. Briefly, the solution-synthesized CdS nanorod array was coated with a thin layer of Al_2O_3 using ALD and filled with poly(methyl methacrylate) (PMMA) to protect against shunting between the p-type and n-type contacts. Photolithography and O_2 plasma etching were used to define windows with areas of ~25 μm^2 where the devices were fabricated. The PMMA was partially removed with an anisotropic etch to leave only a thin layer of polymer on top of the CdS particles at the bottom of the array (Figure 2-3). After the sample was dipped in 10:1 buffered hydrofluoric acid (BHF) solution to remove the Al_2O_3 protection layer, the exposed CdS rods were converted to core-shell CdS-Cu_2S structures to form the junction by dipping the sample into a 90°C aqueous solution of CuCl for 2 to 4 seconds. After cation exchange, the sample was coated with an Al_2O_3 protection layer, and photolithography was used to define the top contact, which consisted of sputtered ITO. A scanning electron microscopy (SEM) image of a representative array device is shown in Figure 2-2b. The PMMA coating of the buffer layer enables the nanorods to be converted to core-shell structures while the polycrystalline buffer layer remains unconverted, which is illustrated by cross-sectional EDS mapping (Figure 2-2c). This design prevents the formation of shunt paths from the Cu_2S to the CdS contact. An EDS linescan of a single nanorod shows that the Cu_2S shell thickness used for devices is greater than 60 nm (Figure 2-2d). The shell thickness can be controlled by the duration of the cation exchange reaction.

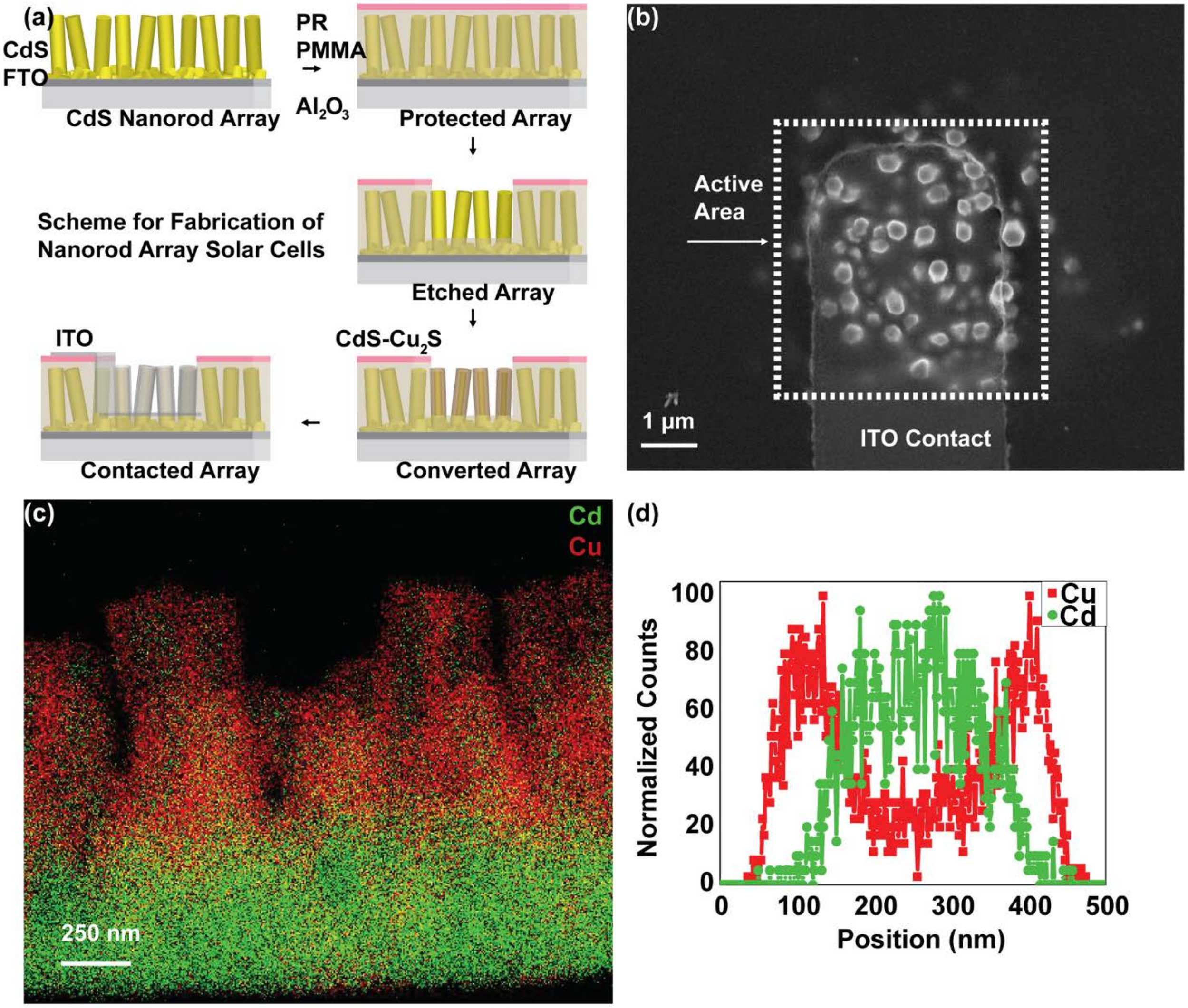

Figure 2-2. Fabrication of photovoltaic devices from CdS nanorod arrays. (a) Schematic of the device fabrication process. (b) SEM image of the active area of a finished device. (c) A cross-sectional EDS map demonstrating that the underlying layer of particles consists of CdS after protection with PMMA and cation exchange of the nanorods above. (d) EDS line scan of a single nanorod showing the measured Cu_2S shell thickness on the CdS core.

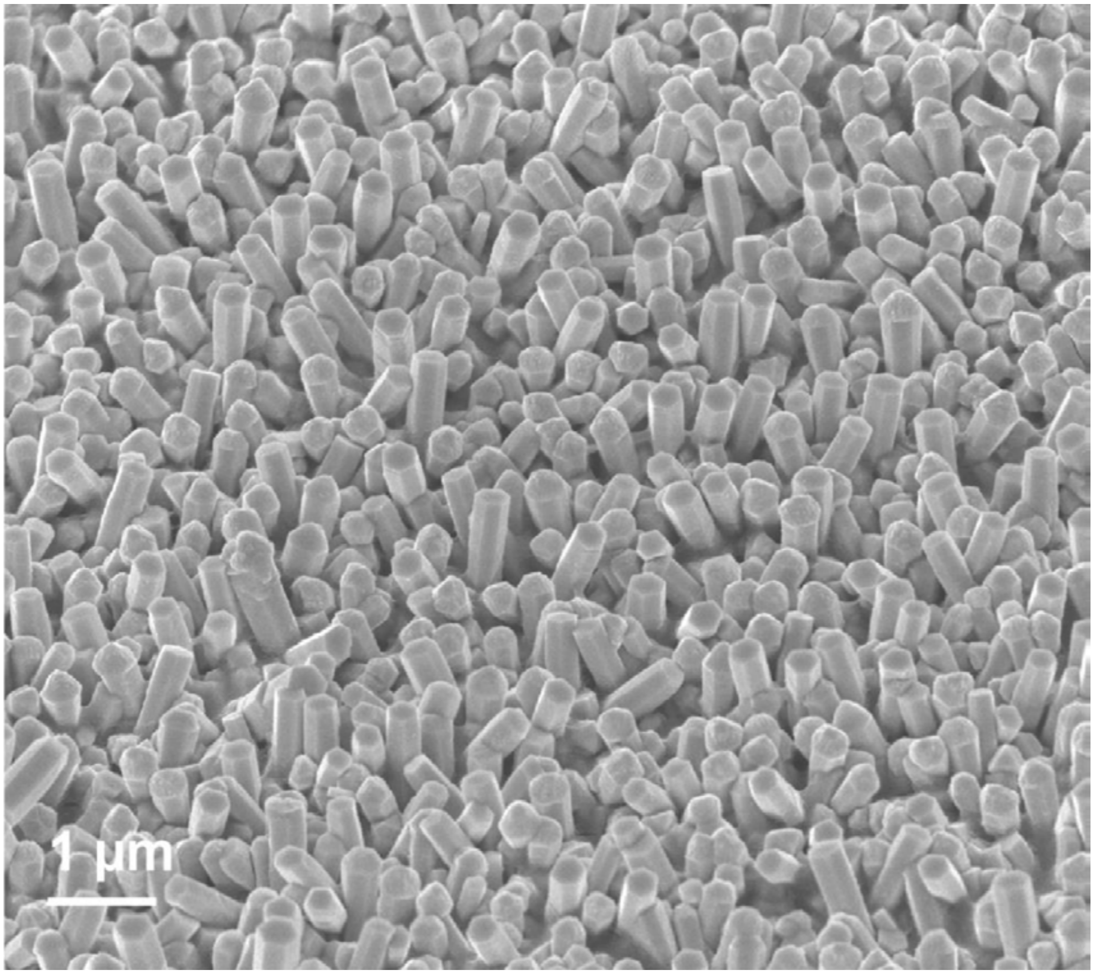

Figure 2-3.SEM image of a CdS nanorod array that has been filled with poly(methyl methacrylate) (PMMA) and subsequently partially etched in O_2 plasma.

2.6 Characterization of Photovoltaic Device Performance:

The photovoltaic performance of the patterned CdS-Cu_2S nanorod array solar cells was measured under 1-sun conditions (AM 1.5G). The *I-V* characteristic of a champion device exhibited an open circuit voltage of 0.45 V, a short-circuit current density of 12.5 mA/cm^2, and a fill factor of 68.1%, which led to an overall efficiency of 3.8% (Figure 2-4a). A table of representative devices is shown in the supporting information (Table 2-1).

The wavelength dependence of the photocurrent reveals that much of the photocurrent arises from wavelengths that are longer than 520 nm (Figure 2-4b), which is the absorption edge of CdS. This shows that Cu_2S contributes a large fraction of the photocurrent in these devices. There is a dip in the normalized photocurrent around 540 nm, which has been observed in other thin film[1,30] and nanostructured[31] CdS/Cu_2S solar cells. This dip corresponds to the tail of the absorption edge of CdS, wavelengths at which the CdS can be illuminated uniformly to generate holes in the buffer layer that are too far from the interface to be collected.[1] This effect can be particularly pronounced in solar cells that employ light trapping.[1]

Stability of the *I*-*V* characteristic is also an important consideration because Cu_2S is known to be unstable against oxidation and to exhibit interdiffusion with CdS.[9-11] After devices were fabricated and measured in ambient conditions, the *I*-*V* characteristic was shown to be stable upon re-measurement 26 days later (Figure 2-4c) after storage in a desiccator filled with nitrogen under ambient illumination and at room temperature. This is in contrast to previous work on single-crystal thin film CdS/Cu_2S devices, which showed marked degradation even upon storage of the devices in an argon atmosphere, which was attributed to interdiffusion between the CdS and Cu_2S.[11] It is possible that the 1 nm ALD layer on the Cu_2S shell, which is meant to protect the array from oxygen plasma damage during ITO sputtering, may also aid the long term stability, as has been suggested by work on ALD Cu_2S films.[8,12] Another possibility is that the single-crystalline nanoscale CdS-Cu_2S interface may exhibit increased stability in comparison to the bulk CdS/Cu_2S interface in thin films, which has been suggested previously by TEM studies of the CdS/Cu_2S interface.[32] The heteroepitaxial CdS-Cu_2S interface specifically avoids any potential grain boundary effects by forming heteroepitaxial interfaces only in single-crystalline nanorods. It is possible that the improved stability in these devices relative to thin-film architectures is due to the unique properties of these nanostructured monolithic interfaces, which avoid deleterious effects due to grain boundaries and may reduce the presence of strain-induced extended defects.

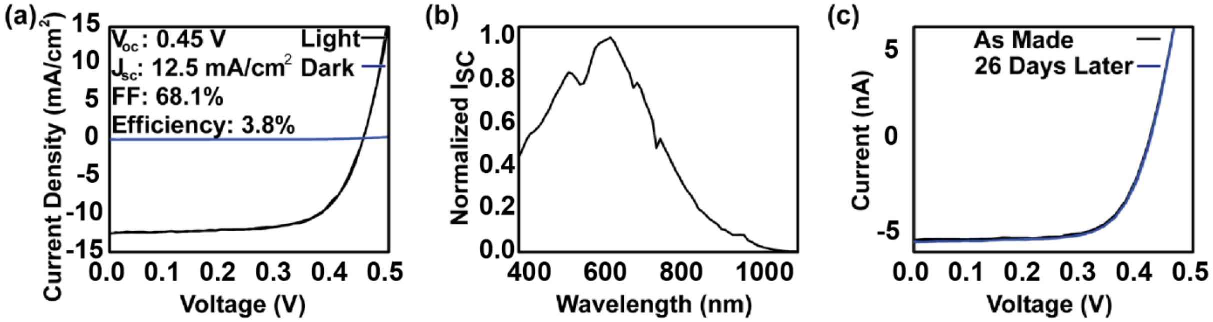

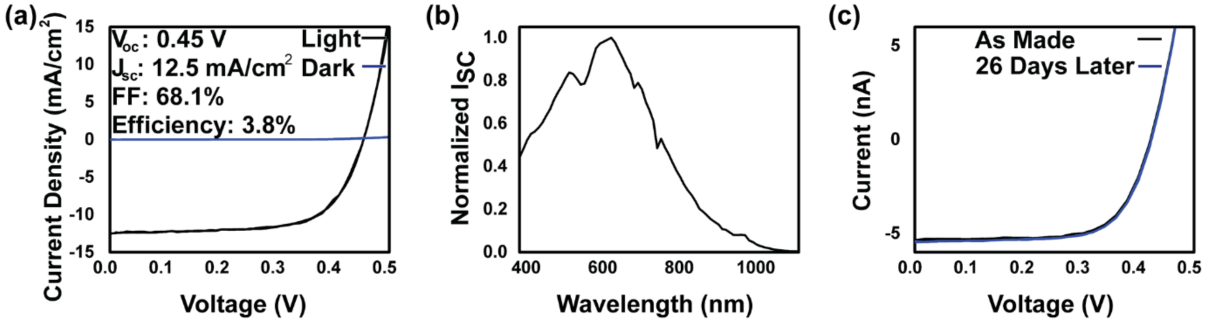

Figure 2-4. Characterization of the performance of CdS-Cu_2S core-shell nanorod array devices. (a) *J*-*V* characteristic of a champion core-shell nanorod array solar cell in the dark and under 1-sun (AM 1.5G) illumination. (b) Short-circuit current normalized by photon flux as a function of wavelength of light showing a strong contribution from the Cu_2S beyond the absorption edge of

CdS at approximately 520 nm. (c) *I-V* characteristic of a core-shell nanorod array solar cell under 1-sun (AM 1.5G) illumination after fabrication and 26 days later after storage in air.

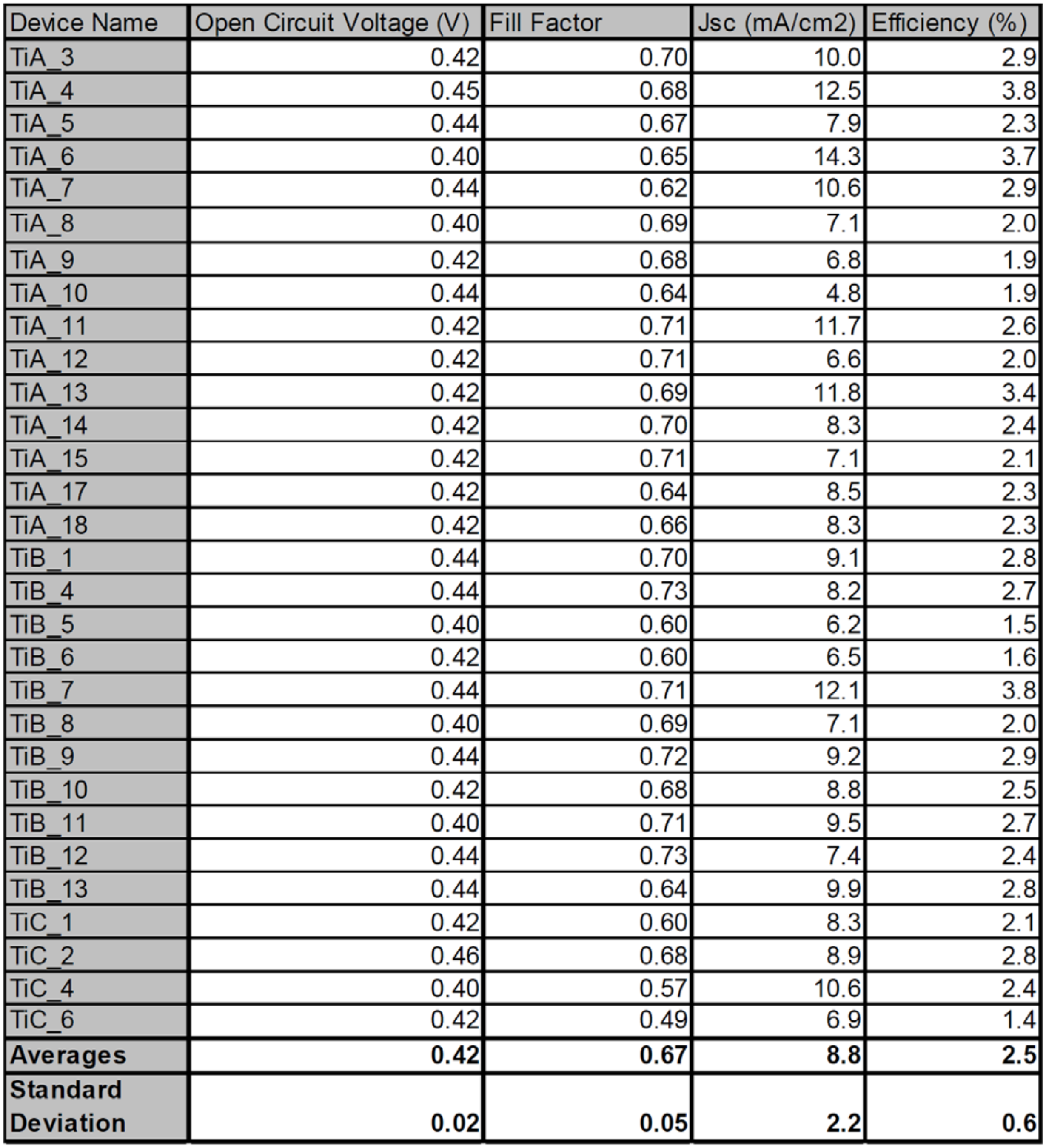

Device Name	Open Circuit Voltage (V)	Fill Factor	Jsc (mA/cm2)	Efficiency (%)
TiA_3	0.42	0.70	10.0	2.9
TiA_4	0.45	0.68	12.5	3.8
TiA_5	0.44	0.67	7.9	2.3
TiA_6	0.40	0.65	14.3	3.7
TiA_7	0.44	0.62	10.6	2.9
TiA_8	0.40	0.69	7.1	2.0
TiA_9	0.42	0.68	6.8	1.9
TiA_10	0.44	0.64	4.8	1.9
TiA_11	0.42	0.71	11.7	2.6
TiA_12	0.42	0.71	6.6	2.0
TiA_13	0.42	0.69	11.8	3.4
TiA_14	0.42	0.70	8.3	2.4
TiA_15	0.42	0.71	7.1	2.1
TiA_17	0.42	0.64	8.5	2.3
TiA_18	0.42	0.66	8.3	2.3
TiB_1	0.44	0.70	9.1	2.8
TiB_4	0.44	0.73	8.2	2.7
TiB_5	0.40	0.60	6.2	1.5
TiB_6	0.42	0.60	6.5	1.6
TiB_7	0.44	0.71	12.1	3.8
TiB_8	0.40	0.69	7.1	2.0
TiB_9	0.44	0.72	9.2	2.9
TiB_10	0.42	0.68	8.8	2.5
TiB_11	0.40	0.71	9.5	2.7
TiB_12	0.44	0.73	7.4	2.4
TiB_13	0.44	0.64	9.9	2.8
TiC_1	0.42	0.60	8.3	2.1
TiC_2	0.46	0.68	8.9	2.8
TiC_4	0.40	0.57	10.6	2.4
TiC_6	0.42	0.49	6.9	1.4
Averages	**0.42**	**0.67**	**8.8**	**2.5**
Standard Deviation	**0.02**	**0.05**	**2.2**	**0.6**

Table 2-1. Table of Representative Solar Cells. The efficiency and short circuit current density of each solar cell is calculated with based on the area of each individual solar cell with the average area of 24 μm^2 for the devices shown in this table. Although devices with areas up to 2500 μm^2

were fabricated, peak efficiency generally dropped with increasing size because of the formation of shunt paths over large areas of the nanorod array.

2.7 Prospects for the Improvement of Cu_2S/CdS Nanostructured Solar Cells:

Moving forward, several challenges remain to be overcome to achieve large-area nanorod array solar cells that surpass the efficiencies of thin-film CdS/Cu_2S solar cells while maintaining stability. While single-nanowire CdS/Cu_2S solar cells produced open circuit voltages and fill factors greater than those of planar solar cells, these metrics were lower for the nanorod array solar cells. One possible explanation is that the solution-phase-synthesized CdS is more likely to possess defects that facilitate recombination as compared to the nanowires grown at higher temperatures via the VLS-growth mechanism. In principle, this difficulty can be overcome though treatments of the solution-grown CdS such as annealing, which decreases the CdS defect emission in photoluminescence (Figure 2-5). Another possibility is that the band alignment and resulting open circuit voltage between the CdS and Cu_2S are not optimized.

As the maximum current density for Cu_2S is 40 mA/cm^2, improvements still are necessary to approach this limit. As shown in Figure 2-4b, the wavelength-dependent short-circuit current indicates that many photons absorbed by the CdS-Cu_2S array are not being collected, particularly at wavelengths less than 500 nm. This is in contrast to previous work on the single nanowire core-shell solar cells, which exhibited excellent carrier collection of light for carriers from photons with wavelengths less than 500 nm.[14] A possible explanation for the decreased collection of charges from light with wavelengths less than 500 nm is that light scattered within the array could be absorbed in the ITO top contact, the FTO underneath the CdS nanorod array, or the CdS buffer layer, where the generated carriers would be too far from the core-shell interfaces to be collected (Figure 2-6).

Scaling up these devices to macroscopic arrays is also an area requiring further investigation. In this study, the size of the active area of the photovoltaic devices was limited by the tendency to form shunt paths during cation exchange when the PMMA protection layer was too thin. If the nanorods were lengthened, it would allow for greater path length for light absorption in the core-shell array, a more robust protection layer, and a reduced portion of light absorbed by the buffer layer of CdS particles. This would improve the scalability and efficiency of these devices.

Lastly, the stability of the CdS/Cu_2S interface within these nanostructures must be investigated more fully. While the preliminary measurement indicating stability after 26 days of storage is promising, further tests investigating the stability under photovoltaic operating conditions are essential.

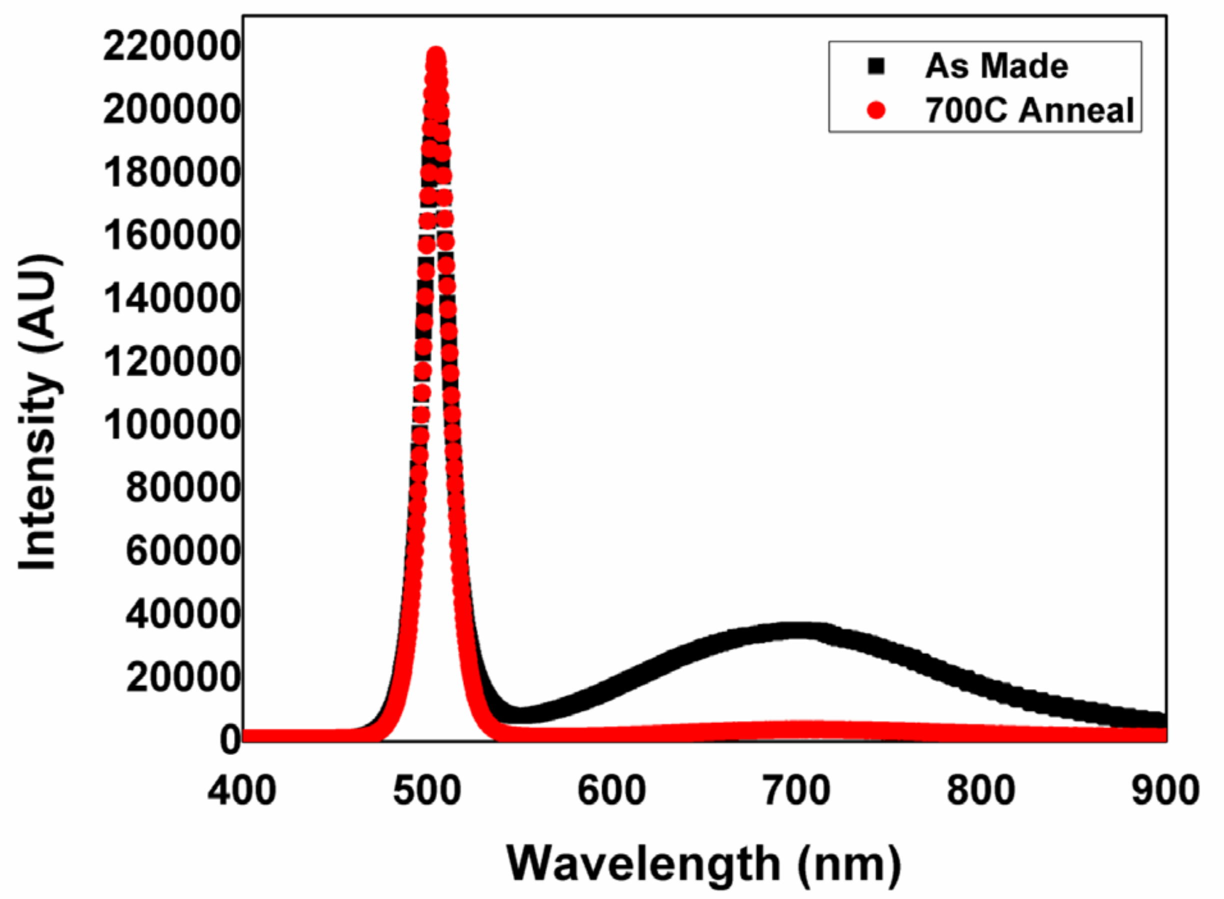

Figure 2-5. Photoluminescence of solution-grown CdS coated with Al_2O_3 before and after annealing at 700C in Ar gas.

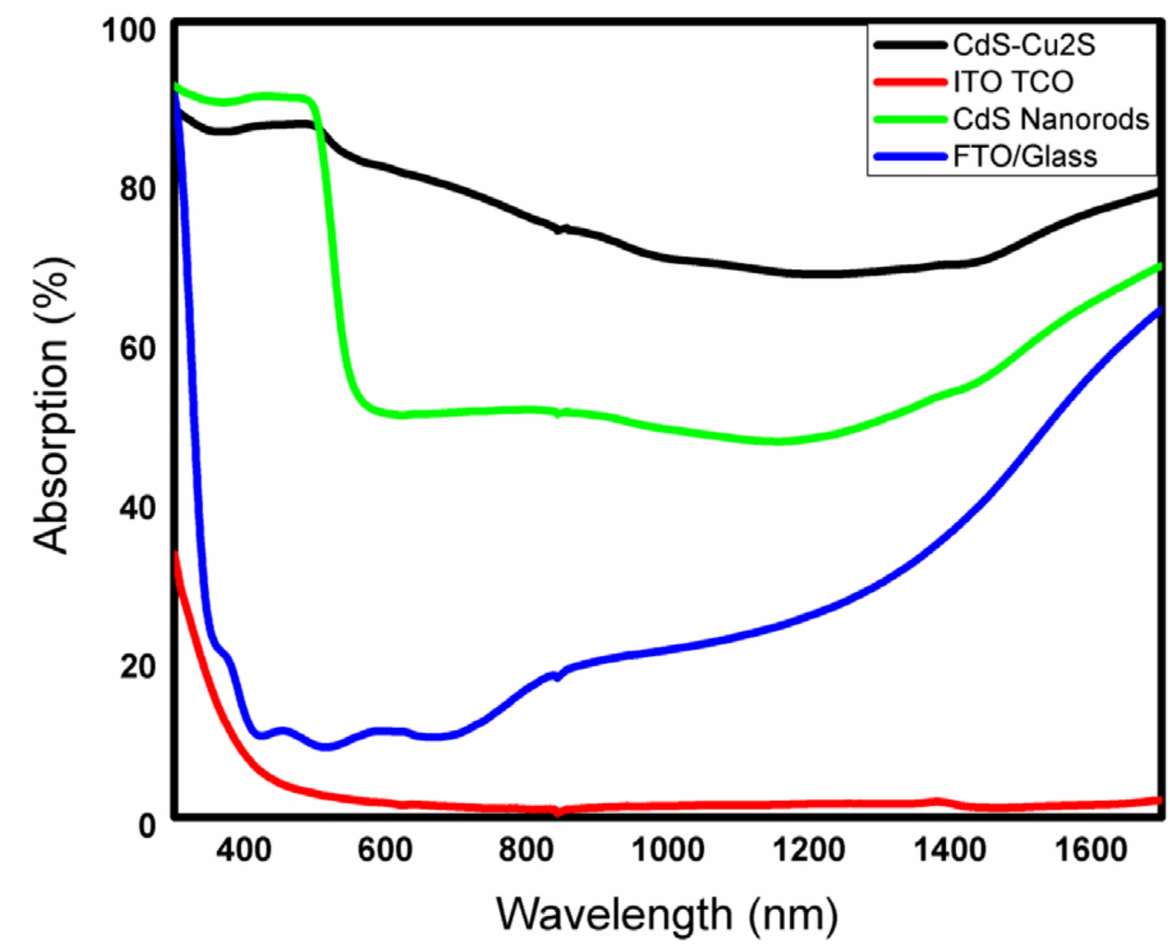

Figure 2-6. UV-vis absorption of the FTO/glass substrate, CdS nanorod array on FTO/glass substrate, $CdS-Cu_2S$ nanorod array on FTO/glass substrate, and ITO on quartz used as the top contact. Notches in the curves around 840 nm are artifacts of switching detectors.

2.8 Chapter 2 Conclusions:

In summary, solution-processed $CdS-Cu_2S$ core-shell nanorod array solar cells have been fabricated and characterized. The champion micro-scale devices have an efficiency of 3.8% and are stable after at least one month of storage. This efficiency approaches that of single nanowire devices and is only a factor of three below the efficiency of the record thin film CdS/Cu_2S devices. As compared to the single nanowire devices previously reported, the current density has been improved, but the open circuit voltage has been reduced, which is likely related to the material quality. The stability of these photovoltaic devices based on a nanoscale $CdS-Cu_2S$ junction is an area deserving of further study. In terms of future application, many improvements can be made to the core-shell array to enable a more robust protection layer that would allow for larger-area devices. This work represents one step towards the goal of improving the efficiency of photovoltaics through the use of nanostructured absorbers.

2.9 Chapter 2 Methods:

CdS Nanorod Growth. The growth of CdS nanorods on conductive FTO or ITO substrates was based on a previously reported hydrothermal method.[26,27] CdS nanorods were grown on pre-scored conductive substrates on glass in an autoclave at 200°C for 4 hours. After this reaction, the CdS array was placed back into the autoclave with a fresh stock solution to enlarge the existing nanorods by performing the reaction a second time. The CdS array coated substrates were carefully broken along the pre-scored lines into individual chips of about 1 cm^2. A more detailed description of the CdS array growth is provided in the Supporting Information.

Cation Exchange Reaction. The solution for the cation exchange reaction was prepared in a 25 mL 3-neck flask with 15 mL of 1 M HCl acid. The pH was adjusted to 7 by dropwise addition of hydrazine. An additional 10 mL of deionized water was added. The solution was purged of oxygen by bubbling nitrogen gas throughout the reaction. After a 5 minute purge at room temperature, heat was applied by a heating mantle to raise the temperature to 90°C. At 50°C, 0.14g of copper (I) chloride (Aldrich, reagent grade >97%) was quickly added to the solution, and the 3-neck flask was resealed. The solution initially had a brown-green appearance that cleared as the copper chloride dissolved. After the temperature stabilized at 90°C, the solution was clear with some grey precipitate. The reaction was opened and CdS arrays were dipped into the solution for 3 to 4 seconds of submerged time followed by rinsing the substrate in deionized water to form the core-shell nanorods. Lower pH and temperature values resulted in changes to the appearance of the solution as well as the reaction rate and the phase as has been described in the case of thin films.[29]

Device Fabrication. The as-grown CdS nanorod arrays were coated in 20 nm of Al_2O_3 at 200°C in a home-built ALD system. After functionalizing the surface with hexamethyldisilazane (HMDS), PMMA (C4, Microchem) was spin coated onto the chip. Within several minutes, the sample was annealed at 120°C for 10 minutes on an equilibrated hotplate. I-line photoresist was then spin coated and baked at 90°C for 90 seconds. The active conversion area was defined using photolithography, and the PMMA was removed from the conversion areas by timed O_2 plasma etching. Active areas fabricated ranged from about 20 to 2500 μm^2. The ALD Al_2O_3 was removed by etching in 10:1 buffered hydrofluoric acid (BHF) solution for 60 seconds followed by annealing at 170°C in Ar for 30 minutes to ensure adhesion of the PMMA to the surface of the CdS after the removal of the Al_2O_3. At this point, cation exchange was performed on these samples. After cation exchange, 1 nm of ALD Al_2O_3 was deposited as a protection layer at 50°C. Afterwards, the HMDS-functionalized surface was coated with I-line photoresist and the area for the contacts was patterned using photolithography. The ITO top contact was deposited by sputtering. To perform liftoff of the ITO, the edges of the sample were carefully scratched, and the chip was soaked for 1 hour in isopropanol before the chip was sonicated for 1-2 seconds to remove excess ITO. Prolonged sonication can induce the formation of high pressure tetragonal phases of Cu_2S.[33] After liftoff, the chips were dried under a stream of nitrogen and annealed in air at 200°C for 5 minutes. Afterwards, devices were stored in nitrogen inside a desiccator (Plas Labs, 862-CGA) under ambient conditions until measurement in air. A more detailed description of the device fabrication is provided in the Supporting Information.

Photovoltaic Device Characterization. Light was provided by a 150W Xenon arc lamp (Newport Corporation) with an AM 1.5 G filter (Newport Corporation). A silicon photodiode referenced to an NREL-calibrated photodiode was used to calibrate the light intensity, and a Keithley 2636 source-measure unit was used to measure the *I-V* characteristic with the entire chip under illumination after carefully contacting the top contact with a soft probe (Picoprobe T-4-22). All measurements were carried out in ambient air. The dependence of the normalized photocurrent on wavelength shown in Figure 2-4b was obtained by coupling a 300W Xenon arc lamp (Newport Corporation) to a monochromator (Newport Corporation). The photocurrent was measured at 10 nm increments with approximately 15-nm bandwidth, and calibration was carried out using a calibrated silicon photodiode.

Structural Characterization. SEM images were taken using a JEOL JSM-6340F field emission scanning electron microscope. XRD patterns were acquired using a Bruker AXS D8 Advance diffractometer, which used Co Kα radiation with a wavelength of 1.79026 Å. The CdS XRD pattern was indexed to wurtzite CdS (JCSD Card: 01-074-9663), and the Cu_2S XRD pattern was indexed to low-chalcocite Cu_2S (JCSD Card: 01-073-6145). The ITO was indexed to JCSD Card: 01-089-4596. EDS maps were collected on a FEI Titan microscope operated at 80 kV at the National Center for Electron Microscopy. The microscope was equipped with a FEI Super-X Quad windowless detector based on silicon drift technology controlled by Bruker Esprit software. Cross-sectional samples were prepared by scraping the core-shell nanorod array followed by dry transfer to a Ni TEM grid with a lacey carbon coating. HRTEM images were also taken on the TEAM 0.5 microscope, which was operated at 300kV at the National Center for Electron Microscopy.

2.10 Chapter 2 References:

1. Rothwarf, A. *Sol. Cells*, **1972**, 2, 115-140.
2. Henry, C. H. *J. Appl. Phys*. **1980**, 51, 4494-4500.
3. Beberwyck, B. J.; Surendranah, Y.; Alivisatos A. P. *J. Phys. Chem. C* **2013**, 117, 19759-19770.
4. Rivest, J. B.; Jain P. K. *Chem. Soc. Rev*. **2013**, 43. 89-96.
5. Deka, S.; Miszta, K.; Dorfs, D.; Genovese, A.; Bertoni, G.; Manna, L. *Nano Lett*. **2010**, 10, 3770-3776.
6. Eggleston, A. W.; Moses, M. J. *Sol. Cells*, **1985**, 14, 1-11.
7. Bragagnolo, J. A.; Barnett, A. M.; Phillips, J. E.; Hall, R. B.; Rothwarf, A.; Meakin, J. D. *IEEE Trans. Electron Devices* **1980**, 27, 645-651.
8. Riha, S. C.; Jin, S.; Baryshev, S. V.; Thimsen, E.; Wiederrecht, G. P.; Martinson, A. B. F. *ACS Appl. Mater. Interfaces* **2013**, 5, 10302-10309.
9. Green, M. A. *Prog. Photovoltaics Res. Appl.* **2009**, 17, 183-189.
10. Norian, K. H.; Edington, J. W. *Thin Solid Films* **1981**, 75, 53-65.
11. Al-Dhafiri, A. M.; Russell, J. G.; Woods, J. *Semicond. Sci. Technol.* **1992**, 7, 1052-1057.
12. Martinson, A. B. F.; Riha S. C.; Thimsen, E.; Elam, J. W.; Pellin M. J. *Energy Environ. Sci*. **2013**, 6, 1868-1878.
13. Dasgupta, N. P.; Sun, J.; Liu, C.; Brittman, S.; Andrews, S. C.; Lim, J.; Gao, H.; Yan, R.; Yang, P. *Adv. Mater.* **2014**, 26, 2137-2184.
14. Tang, J.; Huo, Z.: Brittman, S; Gao, H.; Yang, P. *Nat. Nanotechnol.* **2011**, 6, 568-572.

15. Garnett, E. C.; Brongersma, M. L.; Cui, Y; McGehee, M. D. *Annu. Rev. Mater. Res.* **2011**, 41, 269-295.
16. Kayes, B. M.; Atwater, H. A.; Lewis, N. S. *J. Appl. Phys.* **2005**, 97, 114302-114311.
17. Kelzenberg, M. D.; Boettcher, S.W.; Petykiewicz, J. A.; Turner-Evans, D. B.; Putnam, M. C.; Warren, E. L.; Spurgeon, J. M.;. Briggs, R. M. Lewis, N. S.; Atwater, H. A. *Nat. Mater.* **2010**, 9, 239-244.
18. Muskens, O. L.; Rivas, G. R.; Algra, R. E.; Bakkers, E. P. A. M.; Lagendijk, A. *Nano Lett.* **2008**, 8, 2638-2642.
19. Garnett, E.; Yang, P. *Nano Lett.* **2010**, 10, 1082-1087.
20. Fan, Z.; Razavi, H.; Do, J.-W.; Moriwaki, A.; Ergen, O.; Chueh, Y.-L.; Leu, P. W.; Ho, J. C.; Takahashi, T.; Reichertz, J. A.; Neale, S.; Yu, K.; Wu, M.; Ager, J. W., Javey, A. *Nat. Mater.* **2009**, 8, 648-653.
21. Hongyu, S.; Li, X.; Chen, Y.; Guo, D.; Xie, Y.; Li, W.; Liu, B.; Zhang, X. *Nanotechnology* **2009,** 20, 425603.
22. Lee, J.-C.; Lee, W.; Han, S.-H. Kim, T. G.; Sung, Y. M. *Electrochem. Commun.* **2009**, 11, 231-234.
23. Sadtler, B.; Demchenko, D. O.; Zheng, H.; Hughes, S. M.; Merkle, M. G.; Dahmen, U.; Wang, L. W.; Alivisatos, A. P. *J. Am. Chem. Soc*. **2009**, 131, 5285-5293.
24. Zhang, D.; Wong, A. B.; Yu, Y., Brittman, S.; Sun, J.; Fu, A.; Beberwyck, B.; Alivisatos, A. P., Yang, P. *J. Am. Chem. Soc*. **2014**, 136, 17430-17433.
25. Rivest, J. B.; Swisher, S. L.; Fong, L. K.; Zheng, H.; Alivisatos A. P. *ACS Nano* **2011**, 5, 3811-3816.
26. Chen, F.; Qiu, W.; Chen, X.; Yang, L.; Jiang, X.; Wang, M.; Chen, H. *Sol. Energy* **2011**, 85, 2122-2129.
27. Sun, M.; Fu, W.; Li, Q.; Yin, G.; Chi, K.; Zhou, X.; Ma, J.; Yang, L.; Mu, Y.; Chen, Y.; Yang, H. *J. Cryst. Growth* **2012,** 377, 112-117.
28. Pan, C.; Niu, S.; Ding, Y.; Dong, L.; Yu, R.; Liu, Y.; Zhu, G.; Wang, Z. L. *Nano Lett.* **2012**, 3302-3307.
29. Aperathitis, E.; Bryant, F. J.; Scott, C. G. *Sol. Cells* **1990**, 28, 261-272.
30. Gill, W.; Bube, R. *J. Appl. Phys*. **1970**, 41, 3731-3738.
31. Wu, Y.; Wadia, C.; Ma, W.; Sadtler, B.; Alivisatos, A. P. *Nano Lett.* **2008**, 8, 2551-2554.
32. Zheng, H.; Sadtler, B.; Habenicht, C.; Freitag, B.; Alivisatos, A. P., Kisielowski, C. *Ultramicroscopy* **2013**, 134, 207-213.
33. Wang, S.; Yang, S. *Chem. Phys. Lett.* **2000**, 322, 567-571.

Chapter 3

Growth and Anion Exchange Conversion of $CH_3NH_3PbX_3$ Nanorod Arrays for Light-Emitting Diodes

3.1 Abstract:

The nanowire and nanorod morphology offers great advantages for application in a range of optoelectronic devices, but these high quality nanorod arrays are typically based on high temperature growth techniques. Here, we demonstrate the successful room temperature growth of a hybrid perovskite ($CH_3NH_3PbBr_3$) nanorod array, and we also introduce a new low temperature anion exchange technique to convert the $CH_3NH_3PbBr_3$ nanorod array into a $CH_3NH_3PbI_3$ nanorod array while preserving morphology. We demonstrate the application of both these hybrid perovskite nanorod arrays for LEDs. This work highlights the potential utility of post-synthetic interconversion of hybrid perovskites for nano-structured optoelectronic devices such as LEDs, which enables new strategies for the application of hybrid perovskites.

3.2 Introduction:

Recently, hybrid perovskites such as $CH_3NH_3PbI_3$ and $CH_3NH_3PbBr_3$ have disrupted work on other photovoltaic technologies with efficiencies approaching 20%.[1-4] This class of materials offers remarkable photoluminescence quantum efficiencies (PLQE) up to 70% and minority carrier diffusion lengths up to 175 µm, and these materials can be easily synthesized via low temperature solution processing and with extraordinary band gap tunability.[5,6] In light of this, there have been other proposed uses for these perovskite materials for optoelectronic devices beyond solar cells such as for lasers, photodetectors, and LEDs.[7-12] Previously, thin film LEDs (~15 nm) of $CH_3NH_3PbBr_3$ demonstrated external quantum efficiencies of 0.4% at 530 nm.[10] Although the demonstration of electroluminescence was impressive, it was believed that the efficiency was limited by discontinuities in the thin perovskite film that provide shunt paths.[10] Recently, Li et al. demonstrated electroluminescence with peak external quantum efficiencies reaching 1.2% from hybrid perovskite nanocrystals blended with a thin polyimide dielectric polymer.[12] These results demonstrate the promise of hybrid perovskites for the development of high efficiency solution-processed LEDs.

Nanorod arrays have also been proposed as promising morphologies for LEDs because the vertically oriented nanorod array geometry offers advantages in terms of inherently large active surface area, higher charge carrier injection efficiencies, and improved strain relaxation from thermal expansion caused by heating.[13-16] Surface roughness achieved by etching has been shown to improve the light extraction of conventional light-emitting diodes.[17] The naturally large surface area of nanorod arrays combined with the potential difficulty of etching planar hybrid perovskites films without inducing damage makes the perovskite nanorod array an ideal platform for hybrid perovskite LEDs. The nanorod array may also act as a waveguide to improve the extraction of light from the active layer.[16,18,19] Overall, nanorod arrays offer a potential means to realize higher external quantum efficiencies for LEDs.

At present, there are limited examples of any device made from hybrid perovskite nanorods or nanowires, although recent work demonstrates their application for solar cells and single nanowire lasers.[20,21] The hybrid perovskites possess a cubic or tetragonal crystal symmetry, which does not favor the crystallization of one-dimensional nanorods. Recently, there have been several examples of hybrid perovskite nanowire synthesis using various approaches.[20-24] In particular, perovskites grown using lead acetate as a precursor have been shown to yield high quality perovskite crystals, even in aqueous solution.[21, 25-29] These high quality hybrid perovskite crystals grown from a lead acetate precursor exhibit a reduced defect density, which makes this precursor an attractive choice for nanorod array synthesis.[21,28,29]

The potential for post-synthetic interconversion and alloying is another fascinating property of the hybrid perovskites. The ability to exchange ions has proven to be a highly useful method for the synthesis of new, functional nanostructures.[30-32] The ability to interconvert the halide anion could potentially be another means for controlling the properties towards new functional devices based on hybrid perovskites. However, anion exchanges usually suffer from sluggish reaction kinetics and poor morphology retention, which are attributed to the low mobility and large ionic radius of the anion, so the reaction typically results in hollow particles.[30,33] Recently, Pellet et al. has reported the anion exchange of hybrid perovskite films in the solution phase.[34] This is in agreement with the observation that the photoluminescence of $CH_3NH_3PbI_{3-x}Br_x$ shows photoinduced reversible phase segregation, which likely constitutes a reversible *in situ* anion exchange.[35] In addition, it has recently been shown that Br_2 and I_2 gas can be used to convert $CH_3NH_3PbI_3$ to $CH_3NH_3PbBr_3$ or $CH_3NH_3PbCl_3$ through redox chemistry.[36] However, to our knowledge, the complete conversion of $CH_3NH_3PbBr_3$ to $CH_3NH_3PbI_3$ has not been previously demonstrated by any method. The ion exchange chemistry of these hybrid perovskites presents a new chemical degree of freedom to explore in the synthesis and application of these materials.

In this work, we demonstrate a solution-phase growth of high quality $CH_3NH_3PbBr_3$ nanorod arrays, which we convert to $CH_3NH_3PbI_3$ nanorod arrays using a simple morphology-preserving anion exchange reaction. Both of these hybrid perovskite nanorod arrays were used to fabricate the first hybrid perovskite nanorod array LEDs as a demonstration of their utility for optoelectronic devices. The structure of the LED device is ITO/PEDOT:PSS/$CH_3NH_3PbX_3$/F8/Ca/Ag, where 9,9-dioctylfluorene (F8) and poly(3,4-ethylenedioxythiophene) polystyrene sulfonate (PEDOT:PSS) are used to facilitate the injection of electrons and holes into the perovskite active layer, respectively.[10,11] In this work, the $CH_3NH_3PbBr_3$ nanorod array exhibits green electroluminescence at 533 nm with a small full width at half maximum (FWHM) of 26 nm. To synthesize $CH_3NH_3PbI_3$ nanorod arrays, the conversion of $CH_3NH_3PbBr_3$ to $CH_3NH_3PbI_3$ by anion exchange was achieved by annealing at 140 to 150 °C in CH_3NH_3I vapor to convert the $CH_3NH_3PbBr_3$ nanorod array into a $CH_3NH_3PbI_3$ nanorod array with retention of the initial morphology. This $CH_3NH_3PbI_3$ also exhibits electroluminescence as an LED at 782 nm, which demonstrates the quality of the $CH_3NH_3PbI_3$ nanorod array produced by anion exchange.

3.3 Synthesis of $CH_3NH_3PbBr_3$ Nanorod Arrays:

The direct growth of the vertical $CH_3NH_3PbBr_3$ nanorod array is accomplished by coating a saturated methanolic solution of lead acetate onto a PEDOT:PSS coated ITO/glass substrate. This substrate was then placed in a solution of CH_3NH_3Br in 2-propanol to form orange $CH_3NH_3PbBr_3$ nanorod arrays. As shown by scanning electron microscopy (SEM) and transmission electron microscopy (TEM), the individual $CH_3NH_3PbBr_3$ nanorods exhibit a square cross-section with lengths exceeding 1 μm and diameters exceeding 100 nm (Figure 3-1a,b). Although these nanorods are rapidly damaged by the electron beam in the TEM, the selected area electron diffraction (SAED) pattern shown in the inset of Figure 3-1b was indexed to the [001] zone axis of cubic $CH_3NH_3PbBr_3$. This SAED pattern reflects that these $CH_3NH_3PbBr_3$ nanorods are single crystalline. The square cross-section of the nanorod reflects the cubic symmetry of the $CH_3NH_3PbBr_3$ unit cell. As shown in the inset cross-sectional SEM image of the $CH_3NH_3PbBr_3$ array, a buffer layer of $CH_3NH_3PbBr_3$ particles with a thickness of over 100 nm also covers the substrate (Figure 3-1a). The X-ray diffraction (XRD) pattern of the $CH_3NH_3PbBr_3$ nanorod array can be indexed to cubic phase $CH_3NH_3PbBr_3$ with high phase purity as shown in Figure 3-1c.

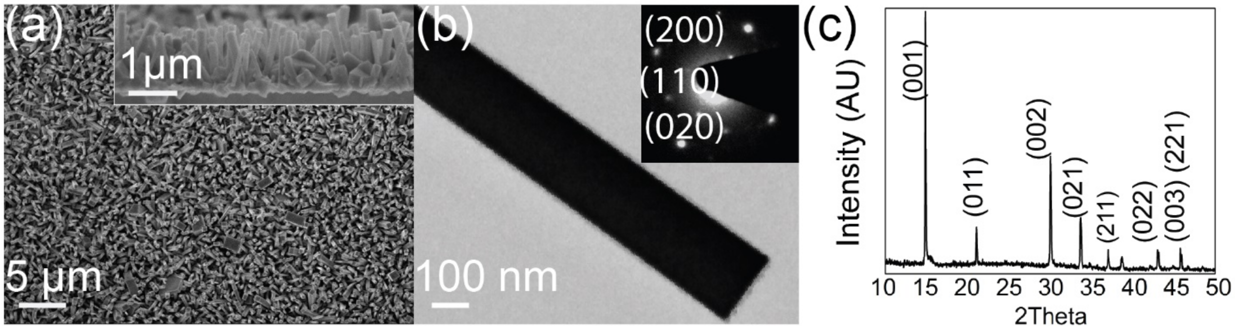

Figure 3-1. (a) Top view SEM image of $CH_3NH_3PbBr_3$ nanorod array. Inset shows a cross-sectional view of the $CH_3NH_3PbBr_3$ array. (b) Low magnification TEM image of a $CH_3NH_3PbBr_3$ nanorod with inset showing the SAED of single nanorod. (c) X-ray diffraction pattern of a $CH_3NH_3PbBr_3$ nanorod array.

3.4 Optical Properties of Solution Synthesized $CH_3NH_3PbBr_3$ Nanorod Arrays:

The optical properties of the $CH_3NH_3PbBr_3$ nanorod array highlight their potential for optoelectronic devices. The optical absorption spectrum of the $CH_3NH_3PbBr_3$ nanorod array is shown in Figure 3-2a. The absorption onset is around 530 nm, which is consistent with the fact that $CH_3NH_3PbBr_3$ is known to have a band gap of 2.3 eV.[37] As shown in Figure 3-2b, the room temperature photoluminescence of the $CH_3NH_3PbBr_3$ peaks at 534 nm with a relatively narrow FWHM of 26 nm under 325 nm excitation by a HeCd laser. No broad sub-bandgap emission typically associated with defects is observed. The low temperature photoluminescence of the $CH_3NH_3PbBr_3$ at 6 K also exhibits a significant red shift in the photoluminescence to a peak emission at 541 nm with a FWHM of 14 nm, which is a trend opposite of the Varshni relation. In this case, the $CH_3NH_3PbBr_3$ undergoes multiple phase transitions at 236.3 K (to a tetragonal phase), 154.0 K (to another tetragonal phase), and 148.8 K (to an orthorhombic phase), which may account for the observed red shift.[38] The time-resolved photoluminescence shows that the

$CH_3NH_3PbBr_3$ nanorod arrays exhibit a monoexponential decay with a lifetime of 14.00 ± 0.04 ns, which is substantially shorter than the maximum values reported for bulk crystals of ~100 ns and is possibly related to surface defects (Fig. 3-2c).[39,40]

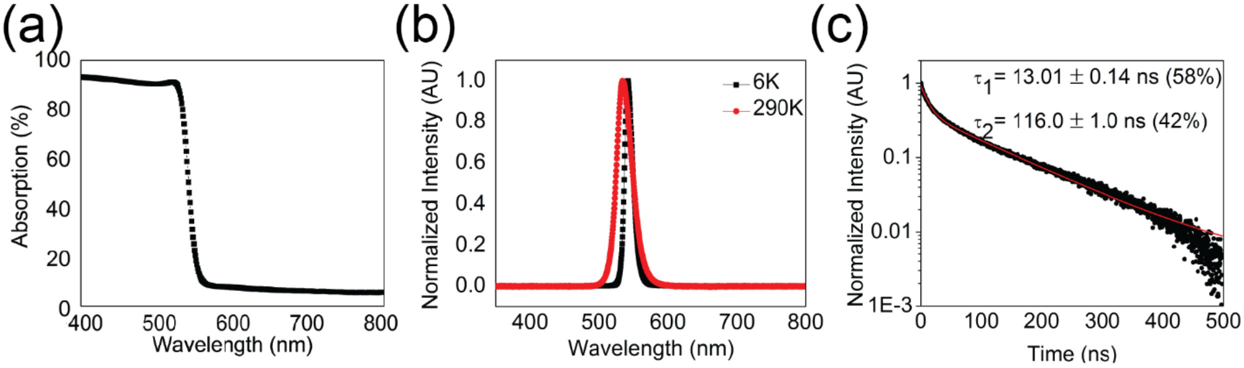

Figure 3-2. (a) UV-visible absorption spectrum of a $CH_3NH_3PbBr_3$ nanorod array grown on a Glass/ITO/PEDOT:PSS substrate. (b) PL spectra of $CH_3NH_3PbBr_3$ nanorod array. (c) TRPL of a $CH_3NH_3PbBr_3$ nanorod array.

3.5 Fabrication of $CH_3NH_3PbBr_3$ Nanorod Array LEDs:

The fabrication of the nanorod array perovskite LED adapts previous reports for planar devices, which utilized PEDOT:PSS as an ohmic hole injection layer and Ca/F8 as an electron injection layer.[10,12] The device consists of ITO/PEDOT:PSS/$CH_3NH_3PbBr_3$/F8/Ca/Ag as shown in the illustration in Figure 3-5a. After the growth of the perovskite array on the PEDOT:PSS coated ITO, the $CH_3NH_3PbBr_3$ nanorod array is coated with F8, which allows for electron transport while preventing quenching of emission at the interface with Ca metal.[10] Afterwards, 100 nm of Ca and 300 nm of Ag is thermally evaporated to coat the nanorod array and enable electrical contact between nanorods, as show via SEM in Figures 3-3 and 3-4. The metal is evaporated through a shadow mask to allow for individually addressable metal contacts between different microscale devices on the nanorod array LEDs.

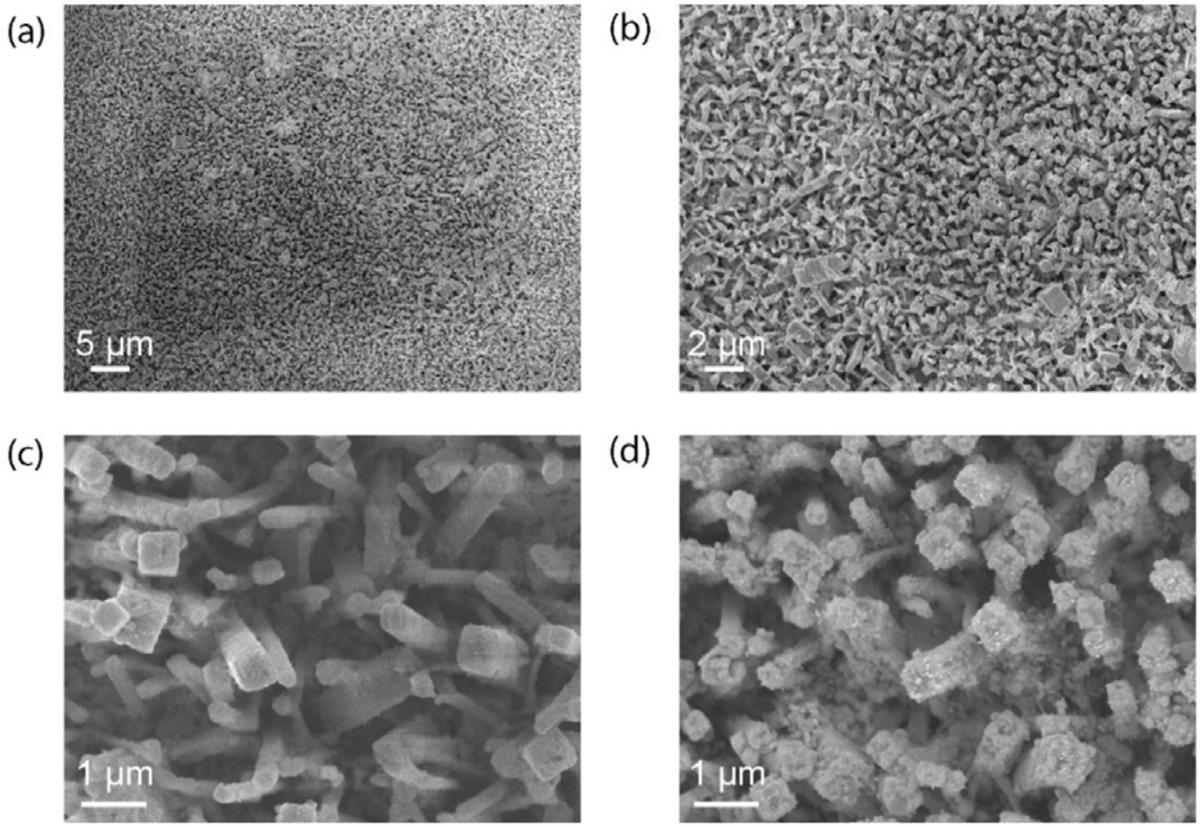

Figure 3-3. (a-b) SEM Image of Nanorod Array LED Device. The contrast of the evaporated metal contact pad can be seen. (c) Higher magnification SEM image showing the F8-coated nanorod array between contact pads. The nanorod morphology remains intact after the nanorods are coated with F8 and the after contacts are evaporated. (d) Higher magnification SEM image of nanorods under the contact pad after thermal evaporation.

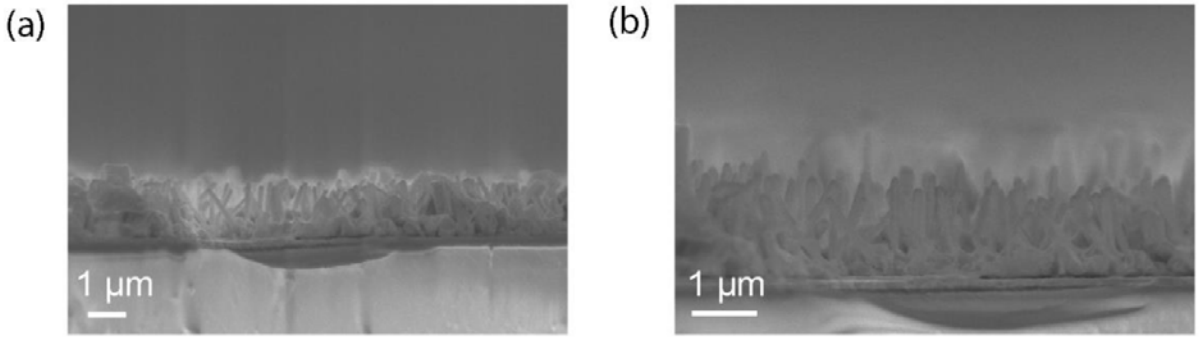

Figure 3-4. (a) Cross-sectional SEM image of nanorod array after coating with F8. (b) Higher magnification SEM image.

3.6 Electroluminescence from $CH_3NH_3PbBr_3$ Nanorod Arrays

For these devices, the turn-on voltage for room temperature electroluminescence is around 3.5 V of DC bias, which is 0.2 V higher than the thin film case.[10] This difference may be due to the increased contact area of the nanorod array relative to the thin film.[41] The electroluminescence observed from the perovskite devices is strikingly green as shown in the image as well as the spectrum of the electroluminescence (Figures 3-5a,b). The image of the electroluminescence was collected through the ITO/glass substrate using an inverted optical microscope. The spectrum of the electroluminescence is centered around 533 nm with a FWHM of approximately 26 nm, which indicates good color purity. This FWHM is identical to the FWHM of the photoluminescence emission, which suggests that there is good hole and electron injection into the active layer. It is notable that there is no electroluminescence that could be attributed to F8 in this device, which confirms that the role of F8 is for electron transport to the active $CH_3NH_3PbBr_3$. Both the electroluminescence image and spectrum were collected at 10 V and 8 V of bias respectively using DC pulses lasting 100 ms and spaced 200 ms apart. As seen in Figure 3-5d, the DC current density may exceed 10 A/cm^2, which can lead to rapid device failure caused by Joule heating. Although this current density is high, it is notable that this value is within an order of magnitude of the current densities reported for planar thin film $CH_3NH_3PbI_{3-x}Cl_x$ LEDs.[10] As shown by Tan et al., the measurement range for the bias can be extended by applying a pulsed DC bias to the LEDs. Under a pulsed DC bias, light emission from the nanorod array LED continues on the time scale of several minutes when tested in ambient air. Untested LEDs remain viable in ambient air for at least 12 hours under low humidity (less than 42 percent). Improvements to the stability of the device while emitting light as well as improvements to the efficiency remain areas of active study.

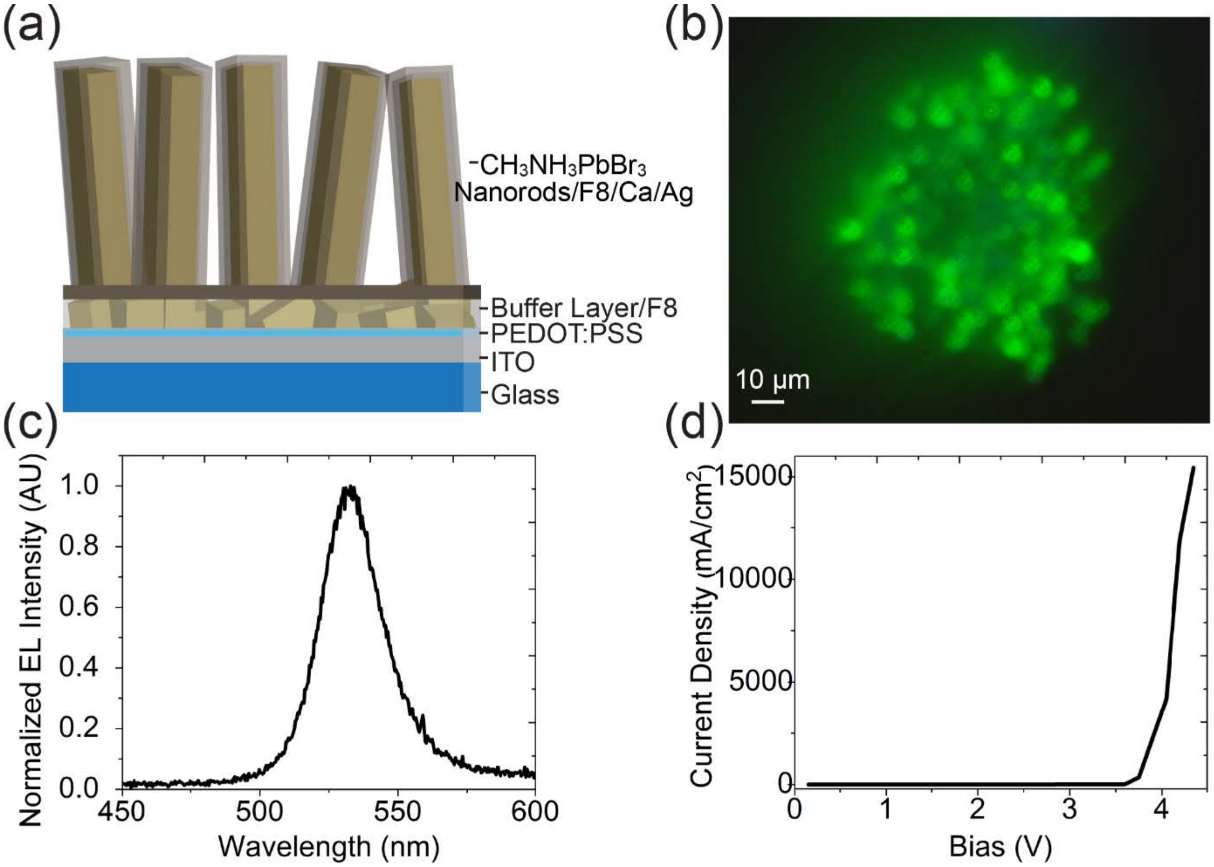

Figure 3-5. (a) Device structure of a $CH_3NH_3PbBr_3$ nanorod array LED. (b) Image of the electroluminescence from the hybrid perovskite nanorod array LED. (c) Electroluminescence spectrum from the hybrid perovskite nanorod array LED. (d) *IV* characteristic of a hybrid perovskite LED.

3.7 $CH_3NH_3PbI_3$ Nanorod Arrays by Anion Exchange:

To synthesize the $CH_3NH_3PbI_3$ nanorod arrays, the anion exchange to form $CH_3NH_3PbI_3$ from $CH_3NH_3PbBr_3$ has been investigated. By annealing the $CH_3NH_3PbBr_3$ nanorod array in CH_3NH_3I vapor at 150ºC, anion exchange to slowly form a $CH_3NH_3PbI_3$ nanorod array is possible. The excess of CH_3NH_3I provides the driving force for the anion exchange reaction. As shown in Figure 3-6a, the nanorod morphology can be retained after the vapor phase anion exchange reaction. The inset photo illustrates the striking conversion of the nanorod arrays from orange $CH_3NH_3PbBr_3$ to black $CH_3NH_3PbI_3$. After the anion exchange conversion, the $CH_3NH_3PbI_3$ nanorods remain single-crystalline as measured by SAED (Figure 3-7). The phase purity of the $CH_3NH_3PbI_3$ nanorod array was confirmed by XRD (Figure 3-6b). The XRD pattern can be fully indexed to the tetragonal phase of $CH_3NH_3PbI_3$. The photoluminescence properties of these films were also investigated, and no photoluminescence from $CH_3NH_3PbBr_3$ remained after the reaction was completed. At room temperature, the $CH_3NH_3PbI_3$ nanorod arrays exhibit photoluminescence at 772 nm with a FWHM of 44 nm, which is shown in Figure 3-6c. To our knowledge, this result is the most complete conversion of $CH_3NH_3PbBr_3$ to $CH_3NH_3PbI_3$ achieved so far. For low temperature photoluminescence, as in the case with the $CH_3NH_3PbBr_3$, a phase transition exists at 162.2 K from tetragonal to orthorhombic, which may influence the low temperature peak position (772 nm, FWHM 39 nm).

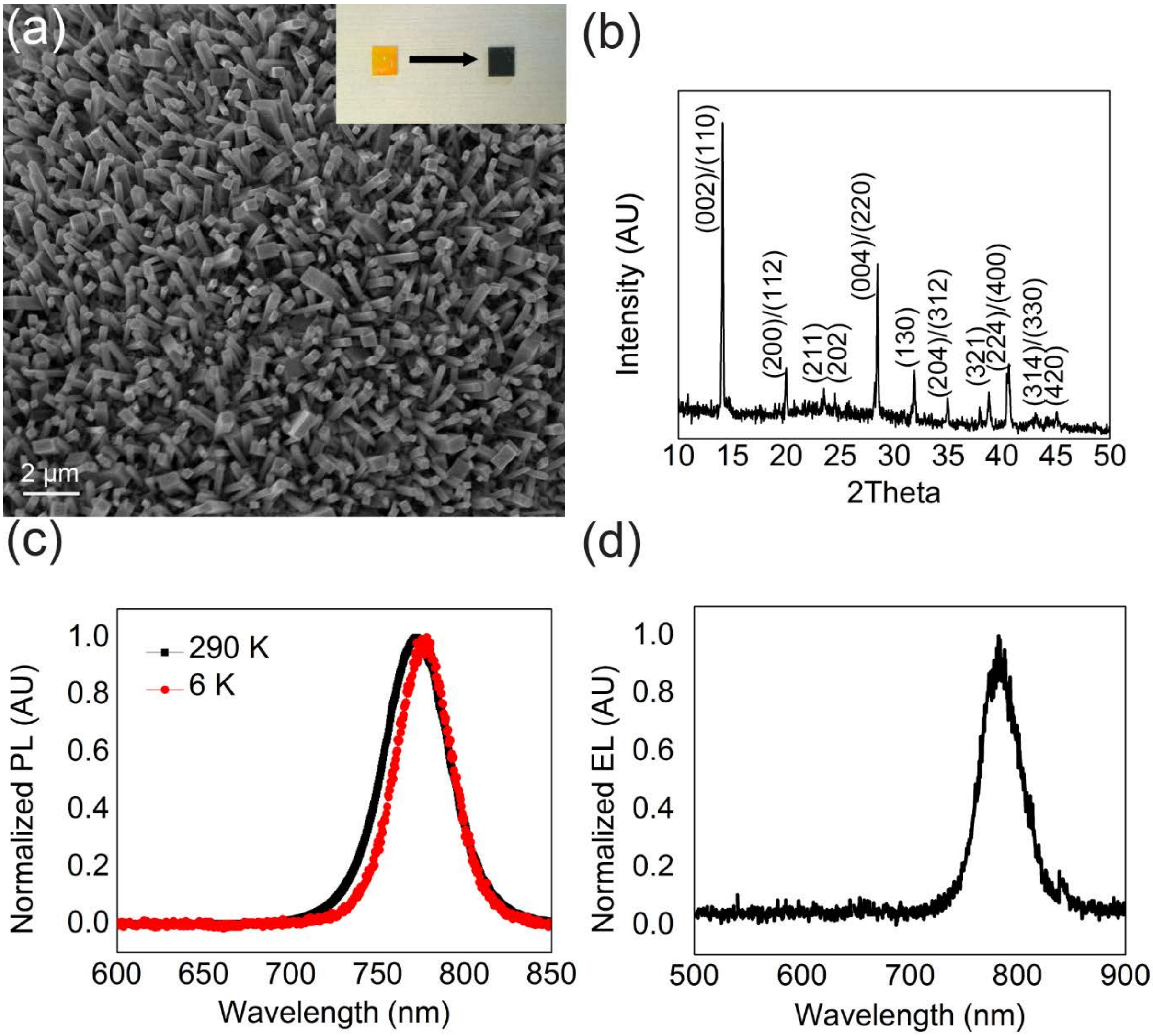

Figure 3-6. Results of Anion Exchange. (a) $CH_3NH_3PbI_3$ nanorod array formed by vapor phase anion exchange of $CH_3NH_3PbBr_3$ nanorod array. Inset shows photograph of converted chip. (b) XRD pattern of $CH_3NH_3PbI_3$ from anion exchange. (c) Normalized photoluminescence of the $CH_3NH_3PbI_3$ nanorod array after conversion. (d) Electroluminescence spectrum of a $CH_3NH_3PbI_3$ LED.

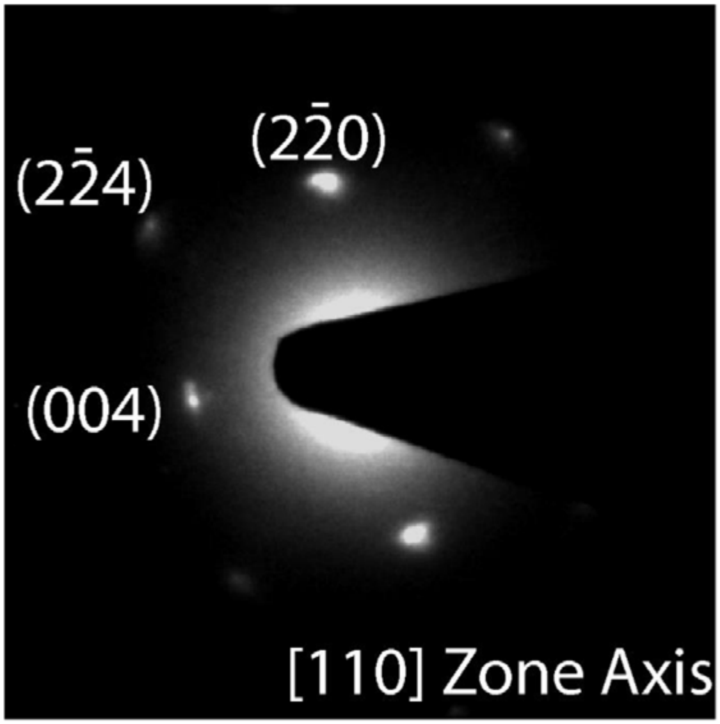

Figure 3-7. Selected area electron diffraction of a single $CH_3NH_3PbI_3$ nanorod after anion exchange from $CH_3NH_3PbBr_3$, indicating that the single crystalline nanorods remain single crystalline after the anion exchange reaction. The $CH_3NH_3PbI_3$ nanorods are rapidly damaged by the electron beam within several seconds, which causes the electron diffraction to quickly decrease in intensity.

3.8 Electroluminescence of $CH_3NH_3PbI_3$:

Finally, this $CH_3NH_3PbI_3$ nanorod array formed by anion exchange was applied to demonstrate room temperature electroluminescence in a device stack with an identical configuration to the $CH_3NH_3PbBr_3$ LED. The electroluminescence shown in Figure 3-6d was observed at a bias of 15 V under a pulsed DC measurement. The emission is centered in the infrared at 782 nm with a FWHM of 41 nm, which means that all of the light emission is beyond the 720 nm limit of visible light that can be seen by the human eye. Overall, this result represents a first example of the use of anion exchange to produce new morphological control over the growth of $CH_3NH_3PbI_3$, which can be applied for functional devices.

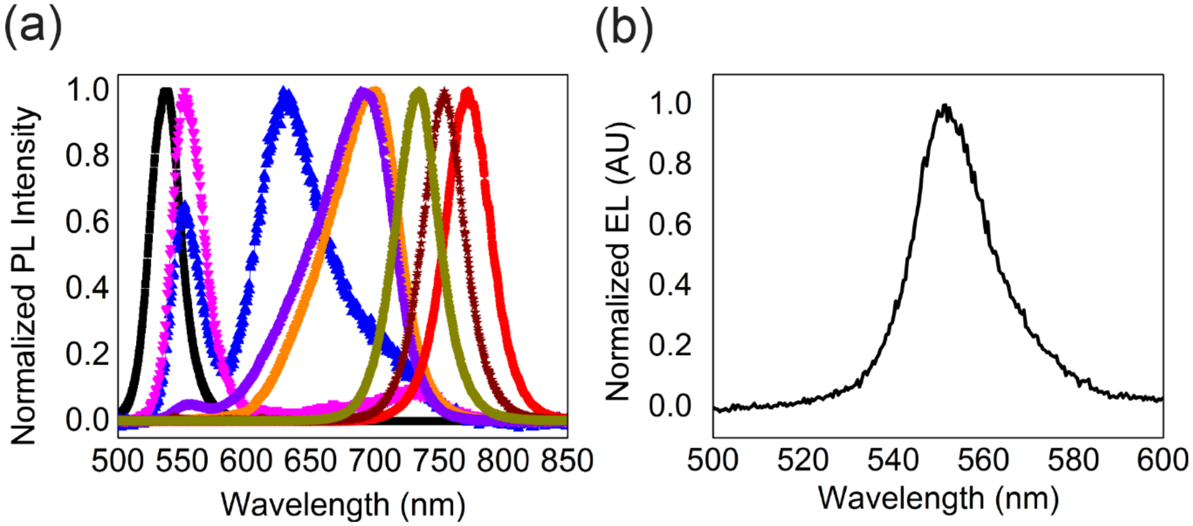

Figure 3-8. Characterization of $CH_3NH_3PbI_xBr_{3-x}$ nanorod arrays formed by partial anion exchange. (a) Photoluminescence of $CH_3NH_3PbI_xBr_{3-x}$ nanorod arrays with various compositions. Phase segregation under excitation is evident for compositions with peak emission from 550 to 700 nm. (b) Electroluminescence of $CH_3NH_3PbI_xBr_{3-x}$ nanorod array with a maximum electroluminescence of 551.5 nm, which is a red shift of 18 nm from 534 nm from electroluminescence by $CH_3NH_3PbBr_3$.

3.9 Chapter 3 Conclusions:

In summary, we have demonstrated the first solution synthesis of $CH_3NH_3PbBr_3$ perovskite nanorod arrays at room temperature, and a new and straightforward anion exchange reaction to form $CH_3NH_3PbI_3$ nanorod arrays. Both of these nanorod arrays exhibit electroluminescence at room temperature. This work identifies the potential for the application of post-synthetic conversion chemistry to modify nanostructured hybrid perovskites for optoelectronic devices such as LEDs. In the future, it may be possible to apply this anion exchange technique to other systems in order to realize other types of optoelectronic devices.

3.10 Chapter 3 Methods:

Synthesis of $CH_3NH_3PbBr_3$ Nanorod Arrays: All chemicals were used as received without further purification. A commercial ITO on glass was washed and ultrasonically cleaned. After oxygen plasma treatment, the ITO substrates were coated with high conductivity grade PEDOT:PSS (Clevios) at 3000 rpm for 40 seconds. Afterwards, the coated ITO substrates were baked at 150°C for 15 minutes. These substrates were coated with 10 µL of a saturated methanolic solution of lead acetate trihydrate (Aldrich), which spreads along the PEDOT:PSS layer. Dropcasting or spin coating are both suitable. The chips were annealed at 65°C for 30 minutes in air. After cooling, the chips were transported into a glove box filled with N2 where they were suspended face down in a centrifuge tube. A freshly dissolved solution of CH_3NH_3Br (1-materials) with a concentration of 5 mg/mL to 9 mg/mL was prepared in 4 mL of anhydrous isopropanol (Aldrich). This solution was quickly added to the vial containing the ITO/PEDOT:PSS/lead acetate substrate to allow the lead acetate film to react with the CH_3NH_3Br solution uniformly. Within several minutes, an orange film began to grow on the substrate. The reaction was allowed to proceed for 20 to 30 hours. The $CH_3NH_3PbBr_3$ arrays were gently washed in isopropanol and dried under nitrogen. It is important to note that changing the concentration of CH_3NH_3Br can result in the formation of cubes, sheets, and disordered wires as shown in Figure 3-9.

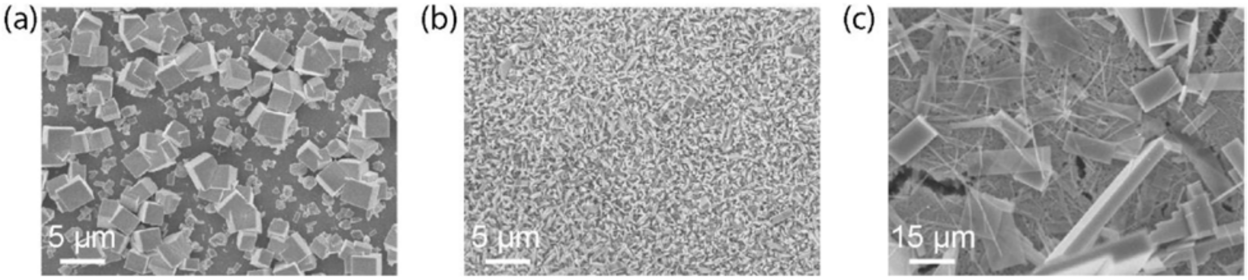

Figure 3-9. SEM Images from $CH_3NH_3PbBr_3$ nanorod arrays grown at differing concentrations of CH_3NH_3Br prepared in parallel. (a) 3 mg/mL, cubes and short rods. (b) 9 mg/mL, array. (c) 12 mg/mL, disordered nanowires and plates.

Anion Exchange Reaction: Within a glovebox, a 20 mL glass vial was charged with 0.1 g of CH_3NH_3I. Afterwards, a chip containing a $CH_3NH_3PbBr_3$ nanorod array was placed in the vial face up. The vial was carefully sealed with a rubber septum and held in place using a cable tie, and the vial was placed half submerged in an oil bath at 140 to 150 °C. Alternatively, a capped vial heated in a glovebox with a hot plate set to 160°C could also be used. Crystals of CH_3NH_3I in direct contact with the array cause inhomogeneous conversion of the film. Conversion appears to occur most rapidly at the edges of the chip. After several hours, CH_3NH_3I deposition was apparent on the sidewalls of the vial. The reaction was allowed to proceed until the film was uniformly black, which required up to 100 hours for full conversion. Partial anion exchange could be achieved by limiting reaction time. In cases with insufficient exposure to CH_3NH_3I vapor to allow anion exchange or exposure to the air during heating, decomposition of the film was observed because of the separation of CH_3NH_3X and PbX_2.

Structural and Optical Characterization: SEM images were acquired using a JEOL JSM-6340F field emission scanning electron microscope. Characterization of the electron diffraction was conducted using a FEI Tecnai TEM at an accelerating voltage of 200 kV with decreased electron dose at high spot size values. The XRD pattern was acquired using a Bruker AXS D8 Advance diffractometer equipped with a lynxeye detector, which used Cu Kα radiation. PL was measured using a 325 nm excitation from a HeCd laser with emission collected on a Nikon A1 microscope coupled to a multimode fiber coupled to a liquid-nitrogen-cooled Si CCD (PI Acton). Optical images were acquired via an Olympus IX71 inverted microscope coupled to a Zeiss AxioCam MRc5 camera. The measurement of the absorption of the $CH_3NH_3PbBr_3$ was carried out using a Shimadzu UV-3101 UV-Vis spectrometer equipped with an integrating sphere. Time resolved photoluminescence was measured using a Picoquant Fluotime 300 instrument with a PMA 175 detector. The sample was excited by a LDH-P-C-405 diode laser with an excitation wavelength of 407.1 nm, and the sample was measured at 534 nm with a power of 11.84 pJ/pulse over an area of 3.8e-4 cm^2.

Device Fabrication: Device fabrication was an adaptation of previously reported methods.[10] Within a glove box, a solution of 10 mg/mL F8 (Aldrich) was dissolved in chlorobenzene by heating after stirring overnight. This solution was spin coated onto the $CH_3NH_3PbBr_3$ array at 3000 rpm and annealed at 100 °C for 10 minutes. A TEM image of a $CH_3NH_3PbBr_3$ nanorod coated with an F8 polymer shell is shown in Figure 3-10 with an average shell thickness of approximately 8 nm. Afterwards, 100 nm of Ca and 300 nm of Ag were thermally evaporated through a shadow mask to define the microscale contacts. The evaporation rate of the contacts was limited to 0.1 Å s^{-1} to prevent thermal decomposition.

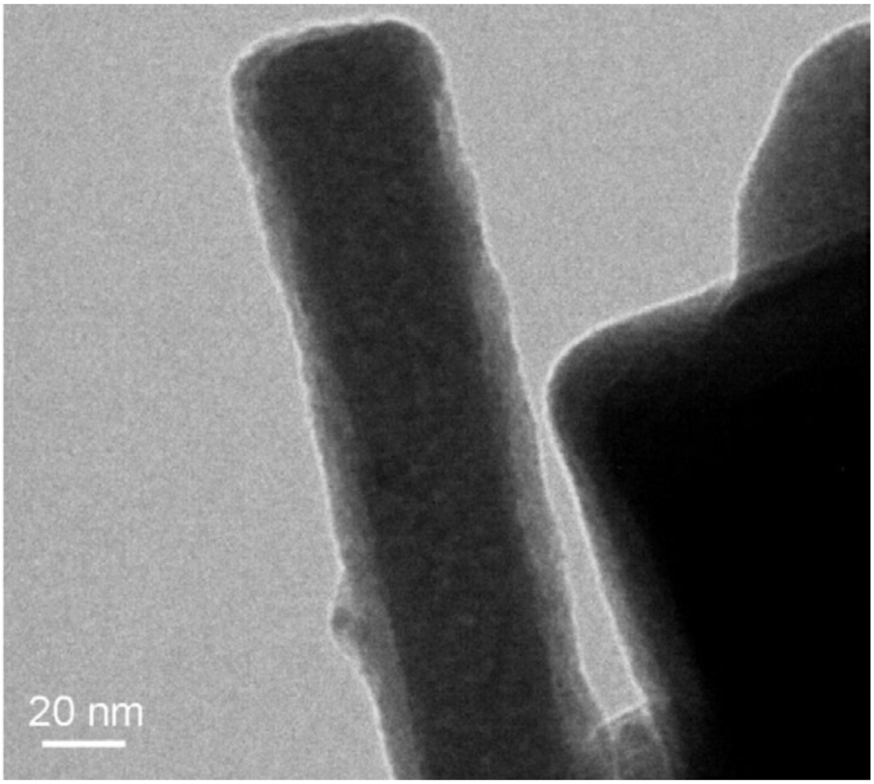

Figure 3-10. Low dose TEM image of $CH_3NH_3PbBr_3$ nanorod after coating with F8 polymer. From the image, the F8 shell is estimated to have an average thickness on the order of 8 nm.

Device Testing: A Keithley 2636 source-measure unit was used to provide bias to the device and measure the *I-V* characteristic. The devices were measured on a home-built probe station that could be coupled to a 60X objective in an inverted microscope. For pulsed DC measurements, the duration of the pulse was 100 ms while the time between pulses was 200 ms. The device was electrically contacted from the top of the metal electrode with a soft probe (Picoprobe T 4-10) coated with indium gallium eutectic (Aldrich).

3.11 Chapter 3 References:

1. Zhou, H.; Chen, Q.; Li, G.; Luo, S.; Song, T.-B.; Duan, H.-S.; Hong, Z.; You, J.; Liu, Y.; Yang, Y. *Science* **2014**, 345, 542-546.
2. Lee, M. M.; Teuscher, J.; Miyasaka, T.; Murakami, T. N.; Snaith, H. J. *Science* **2012**, 338, 643-647.
3. Burschka, J.; Pellet, N.; Moon, S-J.; Humphry-Baker, R.; Gao, P. Nazeeruddin, M. K.; Grätzel, M. *Nature* **2013**, 499, 316-319.
4. Jeon, M. J.; Noh, J. H.; Yang, W. S.; Kim, Y. C.; Ryu, S.; Seo, J.; Seok, S. I. *Nature* **2015**, 517, 476-480.
5. Deschler, F.; Price, M.; Pathak, S.; Klintberg, L. E.; Jarausch, D.-D.; Higler, R.; Hüttner, S.; Leijtens, T.; Stranks, S. D.; Snaith, H.J.; Atatüre, M.; Phillips, R. T.; Friend, R. H. *J. Phys. Chem. Lett.* **2014**, 5, 1421-1426.
6. Dong, Q.; Fang, Y.; Shao, Y.; Mulligan, P.; Qiu, J.; Cao, L.; Huang, J. *Science* **2015**, 347, 967-970.
7. Zhang, Q.; Ha, S. T.; Liu, X.; Sum, T. C.; Xiong, Q. *Nano Lett.* **2014**, 14, 5995-6001.
8. Sutherland, B. R.; Hoogland, S.; Adachi, M. M.; Wong, C. T. O.; Sargent, E. H. *ACS Nano* **2014**, 8, 10947-10952.
9. Dou, L.; Yang, Y. M.; You, J.; Hong, Z.; Chang, W-H.; Li, G.; Yang Y. *Nat. Commun.* **2014**, 5, 5404.
10. Tan, Z.-K.; Moghaddam, R. S.; Lai, M. L.; Docampo, P.; Higler, R.; Deschler, F.; Price, M.; Sadhanala, A.; Pazos, L. M.; Credgington, D.; Hanusch, F.; Bein, T.; Snaith, H. J.; Friend, R. H. *Nat. Nanotechnol.* **2014**, 9, 687-692.
11. Wang, J.; Wang, N.; Jin,Y.; Si, J.; Tan, Z.-K.; Du, H.; Cheng, L.; Dai, X.; Bai, S.; He, H.; Ye, Z.; Lai, M. L.; Friend, R. H.; Huang, W. *Adv. Mater.* **2015**, 27, 2311-2316.
12. Li, G.; Tan, Z.-K.; Di, D.; Lai, M. L.; Jiang, L.; Lim, J. H.-W.; Friend, R. H.; Greenham, N. C. *Nano Lett*. **2015**, 15, 2640-2644.
13. Li, S.; Waag, A. *J. Appl. Phys.* **2012**, 111, 071101.
14. Chen, C.-H.; Chang, S.-J.; Chang, S.-P.; Li, M.-J.; Chen, I.-C.; Hsueh, T.-J.; Hsu, C.-L. *Appl. Phys. Lett.* **2009**, 95, 223101.
15. Sheu, J.-K.; Lu, Y. S.; Lee, M.-L.; Lai, W. C.; Tun, C.-J. *Appl. Phys. Lett.* **2007**, 90, 263511.
16. Lupan, O.; Pauporté, T.; Viana, B. *Adv. Mater.* **2010**, 22, 3298-3302.
17. Fujii, T.; Gao, Y.; Sharma, R.; Hu, E. L.; DenBaars, S. P.; Nakamura, S. *Appl. Phys. Lett.* **2004**, 84, 855-857.
18. Zhong, J.; Chen, H.; Saraf, G.; Lu, Y.; Choi, C. K.; Song, J. J.; Mackie, D. M.; Shen, H. *Appl. Phys. Lett.* **2007**, 90, 203515.
19. Lai, E.; Kim, W.; Yang, P. *Nano Res.* **2008**, 1, 123-128.
20. Im, J.-H.; Luo, J.; Franckevicius, M.; Pellet, N.; Gao, P.; Moehl, T.; Zakeeruddin, S. M.; Nazeeruddin, M. K.; Gratzel, M.; Park, N. G. *Nano Lett.* **2015**, 15, 2120-2126.
21. Zhu, H.; Fu, Y.; Meng, F.; Wu, X.; Gong, Z.; Ding, Q.; Gustafsson, M. V.; Trinh, M. T. Jin, S.; Zhu X-Y. *Nat. Mater*. **2015**, 14, 636-642.
22. Horváth, E.; Spina, M.; Szekrényes, Z.; Kamarás, K.; Gaal, R.; Gachet, D.; Forró, L. *Nano Lett.* **2014**, 14, 6761-6766.
23. Zhu, F.; Men, L.; Guo, Y.; Zhu, Q.; Bhattacharjee, U.; Goodwin, P. M.; Petrich, J. W.; Smith, E. A.; Vela, J. *ACS Nano* **2015**, 9, 2948-2959.

24. Deng, H.; Dong, D.; Qiao, K.; Bu, L. Li, B.; Yang, D. Wang, H.-E.; Cheng, Y.; Zhao, Z.; Tang, J.; Song, H. *Nanoscale* **2015**, 7, 4163-4170.
25. Poglitsch, A.; Weber D. *J. Chem. Phys.* **1987**, 87, 6373-6378.
26. Aldibaja, F. K.; Badia, L.; Mas-Marzà, E.; Sánchez, R. S.; Barea, E. M.; Mora-Sero, I. *J. Mater. Chem. A*, **2015**, 3, 9194-9200.
27. Pisoni, A.; Jaćimović, J.; Barišić, O. S.; Spina, M.; Gaál, R.; Forró, L.; Horváth, E. J. *Phys. Chem. Lett.* **2014**, 5, 2488-2492.
28. Zhang, W.; Saliba, M.; Moore, D. T.; Pathak, S. K.; Hörantner, M. T.; Stergiopoulos, T.; Stranks, S. D.; Eperon, G. E.; Alexander-Webber, J. A.; Abate, A.; Sadhanala, A.; Yao, S.; Chen, Y.; Friend, R. H.; Estroff, L. A.; Wiesner, U.; Snaith, H. J. *Nat. Commun.* **2015**, 6, 6142.
29. Buin, A.; Pietsch, P.; Xu, J.; Voznyy, O.; Ip, A. H.; Comin, R.; Sargent, E. H. *Nano Lett.* **2014**, 14, 6281-6286.
30. Beberwyck, B. J.; Surendranath, Y.; Alivisatos A. P. *J. Phys. Chem. C* **2013**, 117, 19759-19770.
31. Tang, J.; Huo, Z.: Brittman, S; Gao, H.; Yang, P. *Nat. Nanotechnol.* **2011**, 6, 568-572.
32. Zhang, D.; Wong, A. B.; Yu, Y., Brittman, S.; Sun, J.; Fu, A.; Beberwyck, B.; Alivisatos, A. P., Yang, P. *J. Am. Chem. Soc*. **2014**, 136, 17430-17433.
33. Park, J.; Zheng, H.; Jun, Y-W.; Alivisatos, A. P. *J. Am. Chem. Soc.* **2009**, 131, 13943-13945.
34. Pellet, N.; Teuscher, J.; Maier, J.; Grätzel. Chem. Mater. 2015, 27, 2181-2188.
35. Hoke, E. T.; Slotcavage, D. J.; Dohner, E. R.; Bowring, A. R.; Karunadasa, H. I.; McGehee, M. D. *Chem. Sci.*, 2015, 6, 613-617.
36. Solis-Ibarra, D.; Smith, I. C.; Karunadasa, H. I. *Chem. Sci.* **2015**, 6, 4054-4059.
37. Edri, E.; Kirmayer, S.; Kulbak, M.; Hodes, G.; Cahen, D. *J. Phys. Chem. Lett.* **2014**, 5, 429-433.
38. Gesi, K. *Ferroelectrics* **1997**, 203, 249-268.
39. Zhang, M.; Yu, H.; Lyu, M.; Wang, Q.; Yun, J. H.; Wang, L. Z. *Chem. Commun.* 2014, 50, 11727-11730.
40. Zhang, F.; Zhong, H.; Chen, C.; Wu, X-G.; Hu, X.; Huang, H.; Han, J.; Zou, B.; Dong, Y. *ACS Nano* **2015**, 9, 4533-4542.
41. Kim, H.-M.; Cho, Y.-H.; Lee, H.; Kim, S. I.; Ryu, S. R.; Kim, D. Y.; Kang, T. W.; Chung, K. S. *Nano Lett.* **2004**, 4, 1059-1062.

Chapter 4

Properties of Atomically Thin Two-dimensional Organic-inorganic Hybrid Perovskites

4.1 Abstract:

Layered organic-inorganic hybrid perovskites, which have proved to be promising semiconductor materials for photovoltaic applications, have been made into atomically thin two-dimensional (2D) sheets. We report the solution-phase growth of single and few unit-cell-thick single crystalline 2D hybrid perovskites of $(C_4H_9NH_3)_2PbBr_4$ with well-defined square shape and large size. In contrast to other 2D materials, the hybrid perovskite sheets exhibit an unusual structural relaxation and such structural change leads to a band gap shift compared to the bulk crystal. The high quality 2D crystals exhibit efficient photoluminescence, and color tuning could be achieved by changing sheet thickness as well as composition via the synthesis of related materials.

4.2 Introduction:

The organic-inorganic hybrid perovskites, especially $CH_3NH_3PbI_3$, has recently been used in solution-processable photovoltaic devices that have reached 20% power conversion efficiency.[1-4] These layered materials have a general formula of $(RNH_3)_2(CH_3NH_3)_{m-1}A_mX_{3m+1}$, where R is an alkyl or aromatic moiety, A is a metal cation, and X is a halide. The variable, *m*, indicates the number of the metal cation layers between the two layers of the organic chains.[5-11] In the extreme case where $m = \infty$, the structure becomes a three-dimensional (3D) bonded perovskite crystal with a structure similar to $BaTiO_3$. In the opposite extreme where $m = 1$, the structure becomes an ideal quantum well with only one atomic layer of AX_4^{2-} separated by organic chains, in which the adjacent layers are held together by weak van der Waals forces.

This arrangement is fundamentally different from transition metal dichalcogenides, in which one layer of the metal ions is sandwiched between two hexagonal layers of S or Se atoms affording a rigid backbone; the layered hybrid perovskites normally have a tetragonal or orthorhombic structure and are inherently more flexible and deformable.[5-11] By varying the value of *m*, the thickness and the related optoelectronic properties of the quantum well can be tuned. To date, many organic amines, metal cations (Cu^{2+}, Mn^{2+}, Cd^{2+}, Ge^{2+}, Sn^{2+}, Pb^{2+}, Eu^{2+}, etc.), and halides (Cl, Br, and I) have been used to construct such layered materials ($m = 1 \sim 3$), and their corresponding optoelectronic properties have been well studied.[12-15] Previous reports have claimed that the organic layers effectively isolate the 2D quantum wells in each layer from electronic coupling, if the organic chain is longer than propyl amine (*16*). In principle, the properties of the atomically thin 2D quantum well should be the same as the bulk layered material (microscopic crystal, powder, or film). This hypothesis, as well as the technical difficulty of separating individual layers, has likely delayed investigation of freestanding single layers of such 2D materials. Very recently, attempts to obtain ultrathin 2D perovskite samples by spin coating, chemical vapor deposition, or mechanical exfoliation methods have been made with limited success.[17-19]

Here, we report the direct growth of atomically thin 2D hybrid perovskites [$(C_4H_9NH_3)_2PbBr_4$] and derivatives from solution. By using a ternary co-solvent, uniform square-shaped 2D crystals on a flat substrate with high yield and excellent reproducibility were synthesized. We investigated the structure and composition of individual 2D crystals using transmission electron microscopy (TEM) and energy-dispersive spectroscopy (EDS), grazing-incidence wide-angle x-ray scattering (GIWAXS), and Raman spectroscopy. Unlike other 2D materials, a structural relaxation (or lattice constant expansion) occurred in the hybrid perovskite 2D sheets that could be responsible for emergent features. We investigated the optical properties of individual 2D sheets using steady-state and time-resolved photoluminescence (PL) spectroscopy and cathodoluminescence microscopy. The 2D hybrid perovskite sheets have a slightly shifted band edge emission that could be attributed to the structural relaxation. We further demonstrate that the as grown 2D sheets exhibit high PL quantum efficiency as well as wide composition and color tunability.

4.3 Observation of Ultrathin $(C_4H_9NH_3)_2PbBr_4$ Plates:

A structural illustration of a monolayer 2D perovskite (Fig. 4-1A) shows the case for six Br atoms surround each Pb atom, and the four in-plane Br atoms are shared by two octahedrons forming a 2D sheet of $PbBr_4^{2-}$. The negative charges are compensated by the butylammonium that caps the surfaces of the 2D sheet. This structure is amenable to facile solution synthesis. The ionic character of such materials is stronger than the transition metal disulfides and diselenides, and the bulk solid is soluble in polar organic solvents such as dimethylformamide (DMF).[20] To grow 2D sheets, a very dilute precursor solution was dropped on the surface of a Si/SiO_2 substrate and dried under mild heating (see Supplemental Text).[21] A DMF and chlorobenzene (CB) co-solvent was initially investigated as CB helps reduce the solubility of $(C_4H_9NH_3)_2PbBr_4$ in DMF and promote crystallization. Because CB has a similar boiling point and evaporation rate as DMF, the drying of the solvents and the crystallization process were uniform across the whole substrate.

We examined the products by optical microscopy and atomic force microscopy (AFM), but instead of monolayers, thick particles with random shapes formed on the substrate (Fig. 4-2). Hybrid perovskites have limited solubility in acetonitrile and the solvent has been used previously for making microscopic hybrid perovskite single crystals.[22] In this case, acetonitrile evaporates more quickly and helped induce the formation of the ultrathin 2D hybrid perovskite sheets. When acetonitrile was combined with DMF and CB, uniform square sheets grew on the substrate (Fig. 4-1B). The edge length of the square crystals ranged from 1 to 10 μm with an average of 4.2 μm (the size distribution statistics can be found in Fig. 4-3).

The thickness of the square sheets was quantified with AFM. The thickness of the crystals varied from a few to tens of nanometers; the thinnest sheets were ~ 1.6 nm [±0.2 nm]. The AFM images of several monolayer and double layer sheets have thicknesses of 1.6 and 3.4 nm [±0.2 nm] (Fig. 4-1, C and D), whereas the *d* spacing in the bulk crystal is 1.4 nm.[20] AFM tapping mode (non-contact) was used to avoid sample damage, which can lead to a minor overestimation. Also, for the separated monolayer, the organic chain may relax, and the apparent thickness of the monolayer may increase slightly. Additional AFM images of other similar 2D sheets can be found in Fig. 4-4.

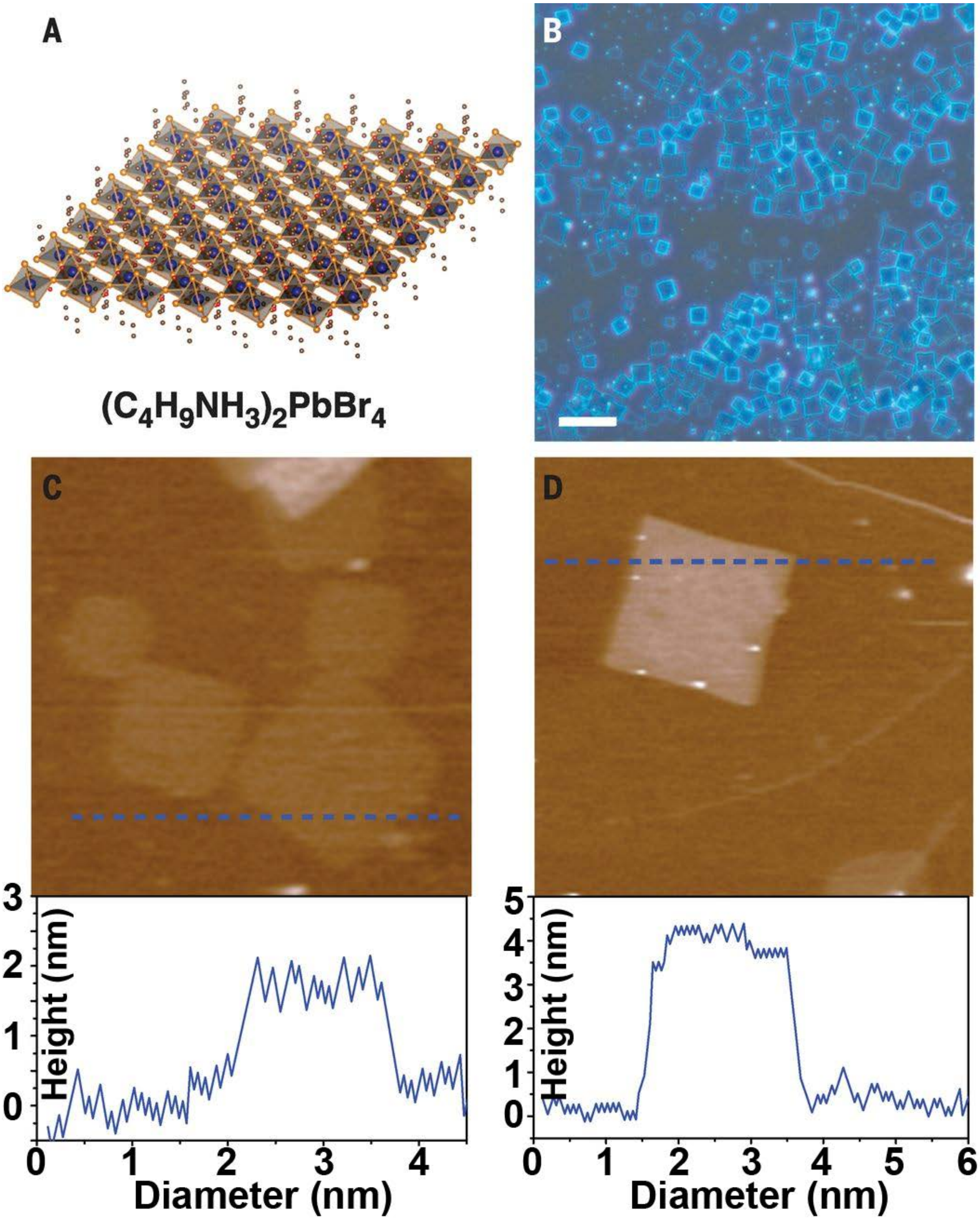

Fig. 4-1. Synthesis of atomically thin two-dimensional $(C_4H_9NH_3)_2PbBr_4$ crystals. (A) Structural illustration of a single layer $(C_4H_9NH_3)_2PbBr_4$ (blue balls, lead atoms; large orange balls, bromine atoms; red balls, nitrogen atoms; small orange balls, carbon atoms; H atoms were removed for clarity). (B) Optical image of the 2D square sheets grown on SiO_2 substrate. The scale bar is 10 µm. (C) Atomic force microscopy image and height profile of several single layers. The thickness is around 1.6 nm [±0.2 nm]. (D) Atomic force microscopy image and height profile of a double layer. The thickness is around 3.4 nm [±0.2 nm].

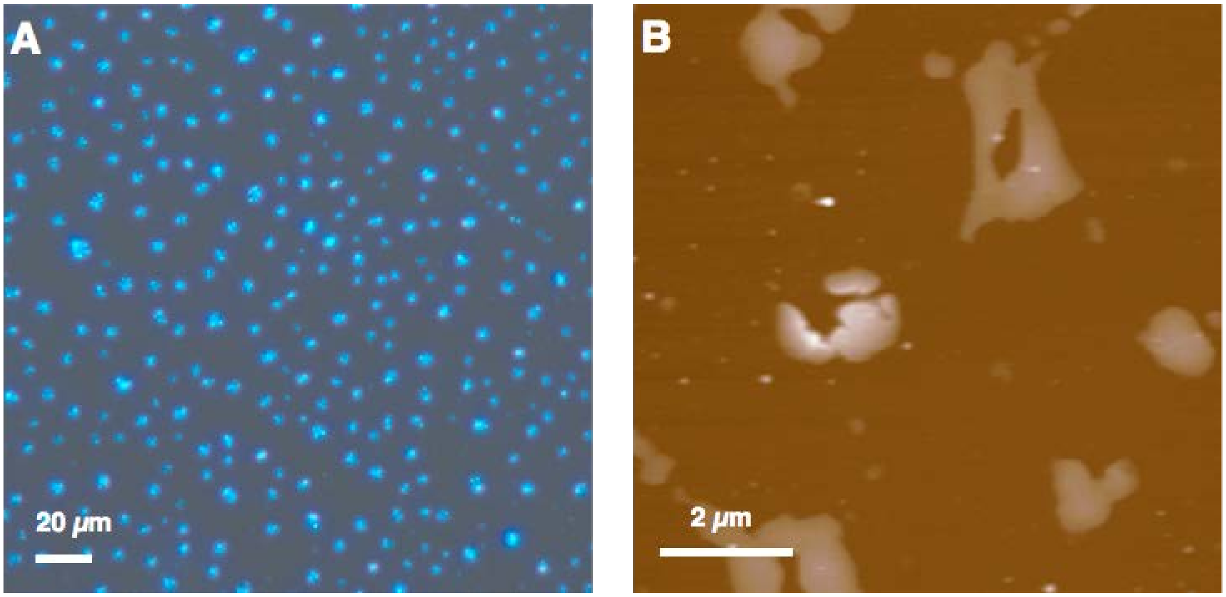

Fig. 4-2. Direct growth of thin $(C_4H_9NH_3)_2PbBr_4$ using dimethylformamide and chlorobenzene co-solvent. (A) Optical image. (B) AFM image. The crystallization and growth processes are not uniform, leading to randomly shaped multi-layer sheets. Only tiny single layer particles with diameters smaller than 200 nm can be found.

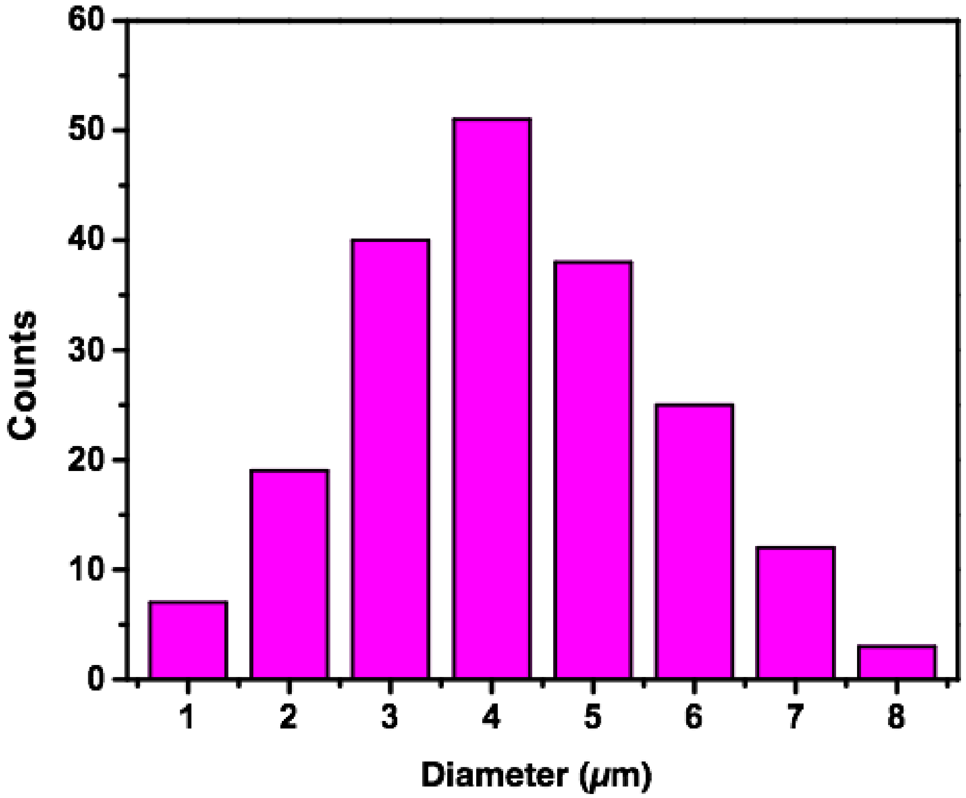

Fig. 4-3. Size distribution statistics for 2D $(C_4H_9NH_3)_2PbBr_4$ synthesized using a ternary co-solvent on Si/SiO_2 substrate.

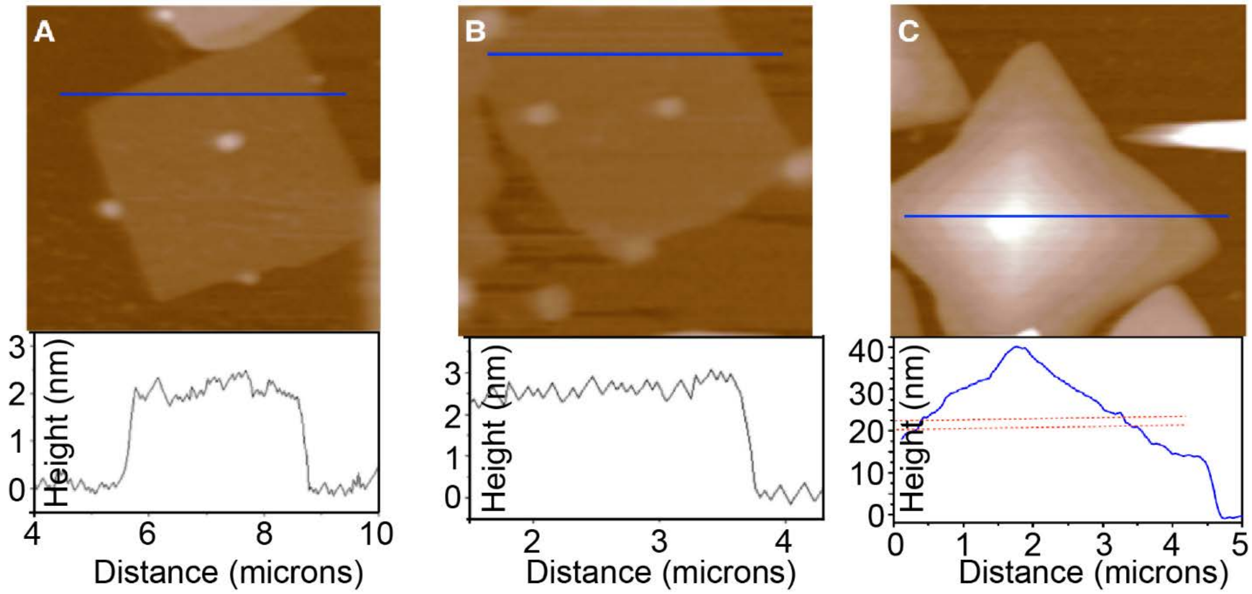

Fig. 4-4. AFM images of 2D sheets. (A, B) Single layers. (C) A pyramids. It was found some of the sheets with over 30 nm thick show such pyramidal structure. The formation of pyramids may provide important information on the growth mechanism and crystal structures of the 2D hybrid perovskite sheets. Since no spiral is observed, the growth mechanism probably occurs in a layer-

by-layer fashion. The formation of the pyramids indicates that there is probably lattice strain between each layer and the new layer stops growth after reaching a certain size. Only a small portion of the thick samples have a pyramidal shape. The majority of sheets are flat, indicating that there may be two growth mechanisms.

By combining AFM and optical microscopy, we correlated the appearance of the sheets in the optical image with their thickness as shown in Fig. 4-5. The thinnest sheet on Si/SiO_2 that we could distinguish in an optical microscope was a double layer. We also prepared large single crystals of $(C_4H_9NH_3)_2PbBr_4$ and investigated conventional mechanical exfoliation method using a scotch tape and the solvent exfoliation method using hexane to disperse the thin sheets.[23] Unfortunately, the majority of the products from mechanical exfoliation were very thick flakes (Fig. 4-6A) and randomly shaped particles from solvent exfoliation (Fig. 4-6B and 4-6C). The monolayer-thick particles obtained were very small (less than 1 µm), which suggests that these hybrid perovskite layers are mechanically brittle.

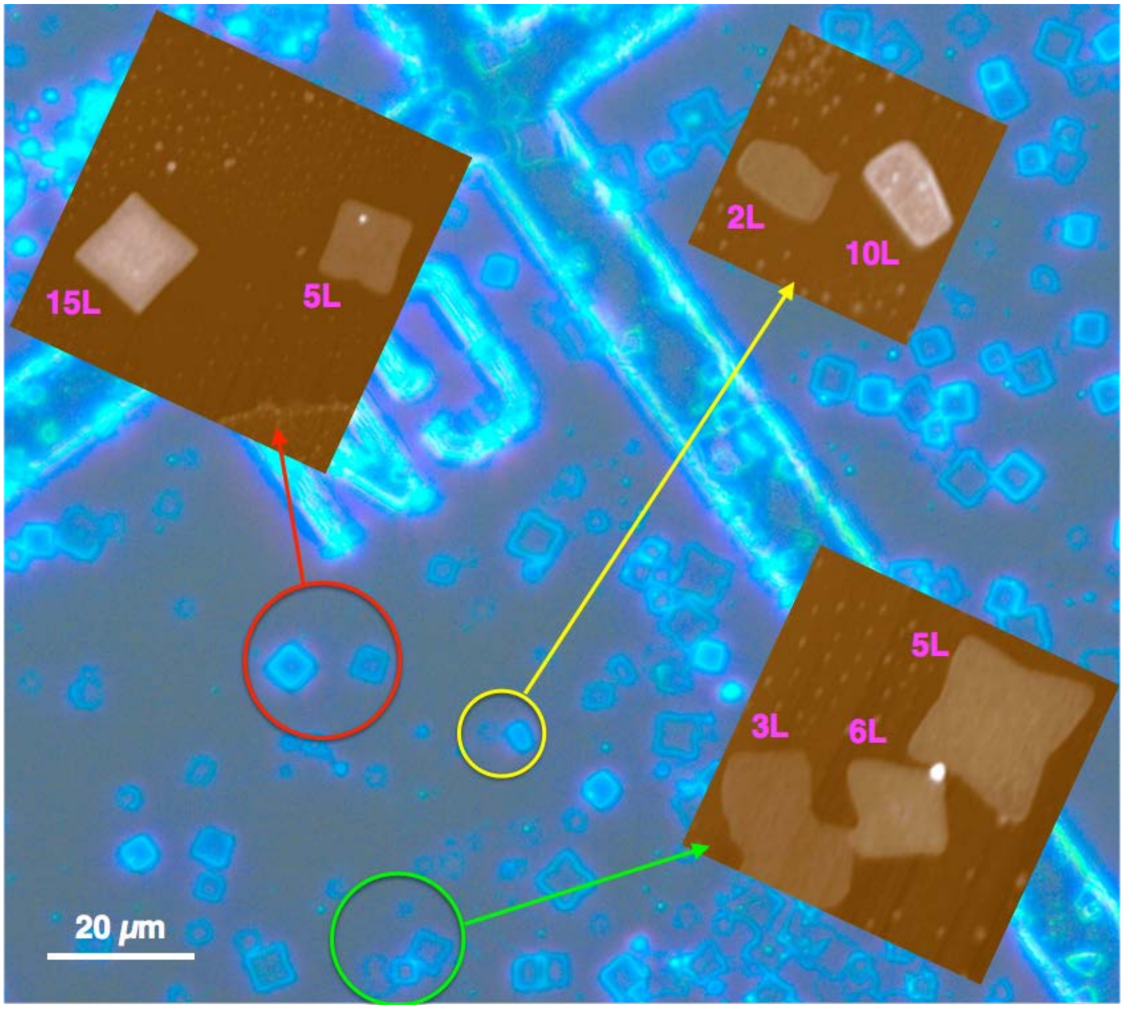

Fig. 4-5. Correlation between optical image and AFM images for the same 2D sheets. The thin sheets were grown on a labeled SiO_2 substrate (300 nm thermal oxide on Si). Dark field optical

images were taken, and then the same spots were measured by AFM. The thinnest sheets that can be seen directly by the optical microscope are double layers.

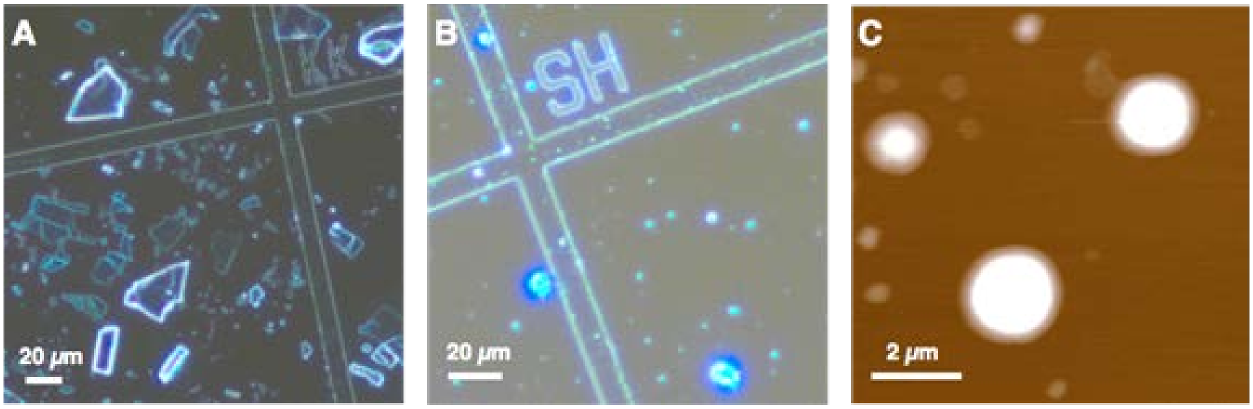

Fig. 4-6. Exfoliation from large single crystals. (A) Optical image of $(C_4H_9NH_3)_2PbBr_4$ exfoliated using a scotch tape. The size and thickness of the sheets have very large distribution. (B) Optical image of $(C_4H_9NH_3)_2PbBr_4$ exfoliated by ultrasonicating the single crystal in hexanes. (C) AFM images of the exfoliated sheets. It is very hard to find a large single layer. The bigger sheets are typically more than 100 nm thick. This is probably because the mechanical properties are not strong enough, so the large thin sheets just break into small pieces (less than 200 nm wide).

4.4 Characterization of the Structure of Ultrathin Layered Halide Perovskite Sheets:

To determine the crystal structure of the 2D hybrid perovskites, x-ray diffraction (XRD) and TEM were used. The XRD pattern revealed that the (001) plane grew parallel to the substrate, and the out-of-plane *d* spacing was 1.42 nm (Fig. 4-7), which is consistent with reported data for this material.[16] The in-plane structural information was revealed by selected-area electron diffraction (SAED) in a TEM. Fig. 4-8A shows a TEM image of a 2D sheet grown on a lacy-carbon grid. After examining more than 20 individual sheets by TEM, we found that they all show similar shape and identical diffraction pattern (additional TEM images are shown Fig. 4-9); Fig. 4-8B shows the SAED pattern of another sheet. The calculated average in-plane lattice constants are a = 8.41 Å and b = 8.60 Å from five sheets, which are slightly greater than the lattice constants in the bulk crystal measured by single-crystal XRD (a = 8.22 Å and b = 8.33 Å, see ref. 19, also Table 4-1, 4-2). The electron diffraction patterns were consistent with structural simulations, which further confirm the structure of the atomically thin 2D structure (Fig. 4-10, 4-11).

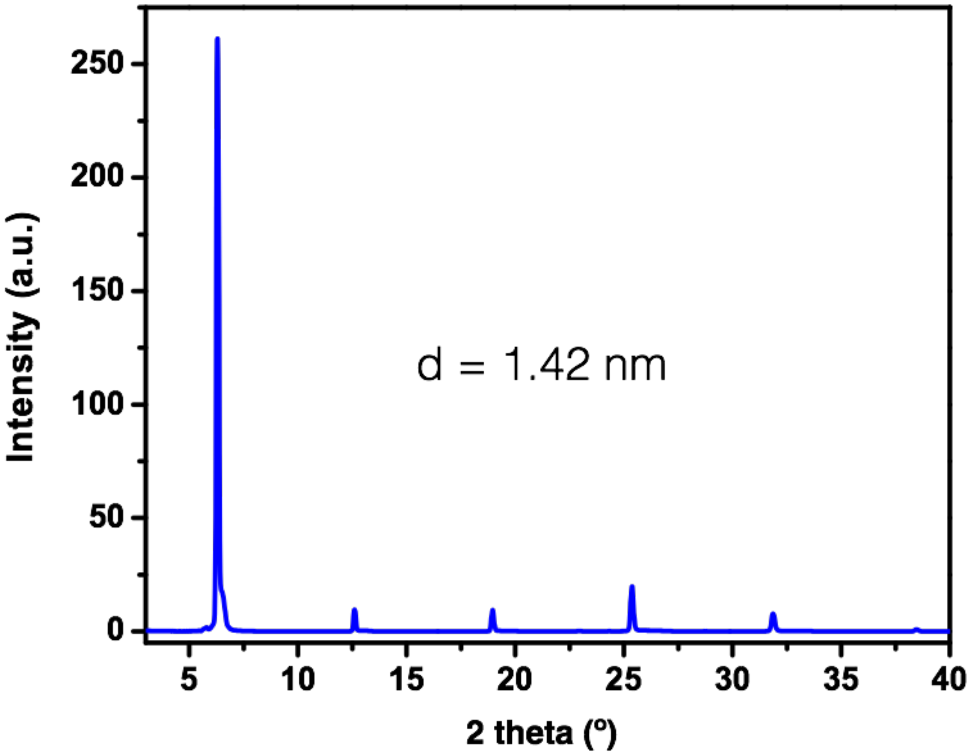

Fig. 4-7. X-ray diffraction of the solution-grown $(C_4H_9NH_3)_2PbBr_4$. A relatively more concentrated solution was used to grow highly dense sheets on the substrate to get enough signal for the measurement.

Table 4-1. Single crystal X-ray diffraction data of $(C_4H_9NH_3)_2PbBr_4$.

Empirical formula	$C_8H_{24}Br_4N_2Pb$	
Formula weight	675.12	
Temperature	100(2) K	
Wavelength	0.71073 Å	
Crystal system	Orthorhombic	
Space group	Pbca	
Unit cell dimensions	a = 8.2530(2) Å	α = 90°.
	b = 8.1375(2) Å	β = 90°.
	c = 27.4028(9) Å	γ = 90°.
Volume	1840.34(9) $Å^3$	
Z	4	
Density (calculated)	2.437 Mg/m^3	
Absorption coefficient	17.833 mm^{-1}	
F(000)	1232	
Crystal size	0.040 x 0.040 x 0.020 mm^3	
Theta range for data collection	1.486 to 25.355°.	
Index ranges	-9<=h<=9, -9<=k<=9, -33<=l<=33	
Reflections collected	28141	
Independent reflections	1678 [R(int) = 0.0376]	
Completeness to theta = 25.000°	100.0 %	
Absorption correction	Semi-empirical from equivalents	
Max. and min. transmission	0.745 and 0.428	
Refinement method	Full-matrix least-squares on F^2	
Data / restraints / parameters	1678 / 0 / 72	
Goodness-of-fit on F^2	1.279	
Final R indices [I>2sigma(I)]	R1 = 0.0225, wR2 = 0.0440	
R indices (all data)	R1 = 0.0269, wR2 = 0.0452	
Extinction coefficient	n/a	
Largest diff. peak and hole	0.953 and -0.761 $e.Å^{-3}$	

Table 4-2. Atomic coordinates (x10^4) and equivalent isotropic displacement parameters (Å^2 x10^3) of $(C_4H_9NH_3)_2PbBr_4$.

	x	y	z	U(eq)
C(1)	4572(6)	5329(6)	8853(2)	20(1)
C(2)	4765(6)	5236(6)	8307(2)	16(1)
C(3)	3620(7)	6372(7)	8040(2)	26(1)
C(4)	3800(8)	6253(8)	7489(2)	39(2)
N(1)	5751(5)	4222(5)	9103(2)	14(1)
Br(1)	4692(1)	5176(1)	6095(1)	14(1)
Br(2)	6904(1)	8106(1)	5013(1)	14(1)
Pb(1)	5000	5000	5000	9(1)

We observed rapid radiation damage of the sheets under the strong electron beam. After exposing the 2D sheets to the electron beam for a few seconds, Pb was reduced and precipitated, and the sample was irreversibly changed (Fig. 4-12). This phenomenon is similar to that observed in alkali halides.[24] More examples of SAED patterns of individual sheets and their corresponding TEM images demonstrating the degradation can be found in Fig. 4-13. Fig. 4-8C to 4-8F show the elemental distribution in the thin sheets; Lead, bromine, carbon, and nitrogen are all present in the square.

The lattice expansion in the 2D sheets was further confirmed through macroscopic GIWAXS measurements. Fig. 4-8G shows the GIWAXS image and Fig. 4-8H shows the integrated pattern. In addition, to the (200) and (020) peaks observed in TEM diffraction, many other peaks can be assigned. The *d* spacing of the (200), (020), (111), and (113) planes are 4.19 (lattice constant a = 8.38 Å), 4.25 (lattice constant b = 8.50 Å), 5.81, and 5.00 Å; respectively. These values are all greater than that of the bulk crystals and are consistent with our TEM measurements of single 2D sheets.

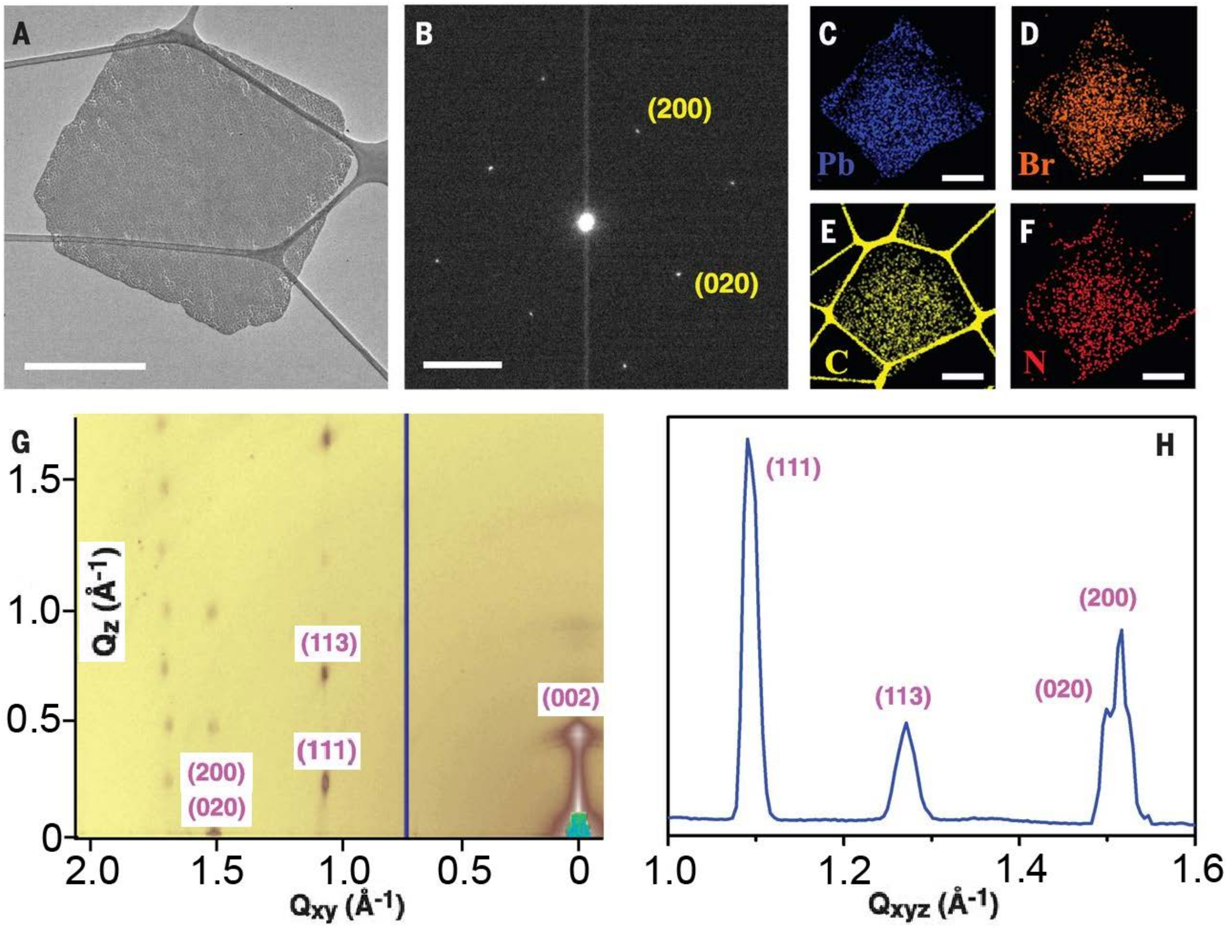

Fig. 4-8. Transmission electron microscopy, energy dispersive spectroscopy, and grazing-incidence wide-angle X-ray scattering studies. (A) TEM image of a thin $(C_4H_9NH_3)_2PbBr_4$ sheet. The scale bar is 1 μm. (B) Electron diffraction pattern of a thin sheet of $(C_4H_9NH_3)_2PbBr_4$. The scale bar is 2 1/nm. (C-F) EDS analysis showing the elemental distribution of lead, bromide, carbon, and nitrogen; respectively. (G) GIWAXS image of the 2D thin sheets. (H) Integrated GIWAXS spectrum of the 2D thin sheets showing the diffraction of (200), (020), (111), and (113) planes.

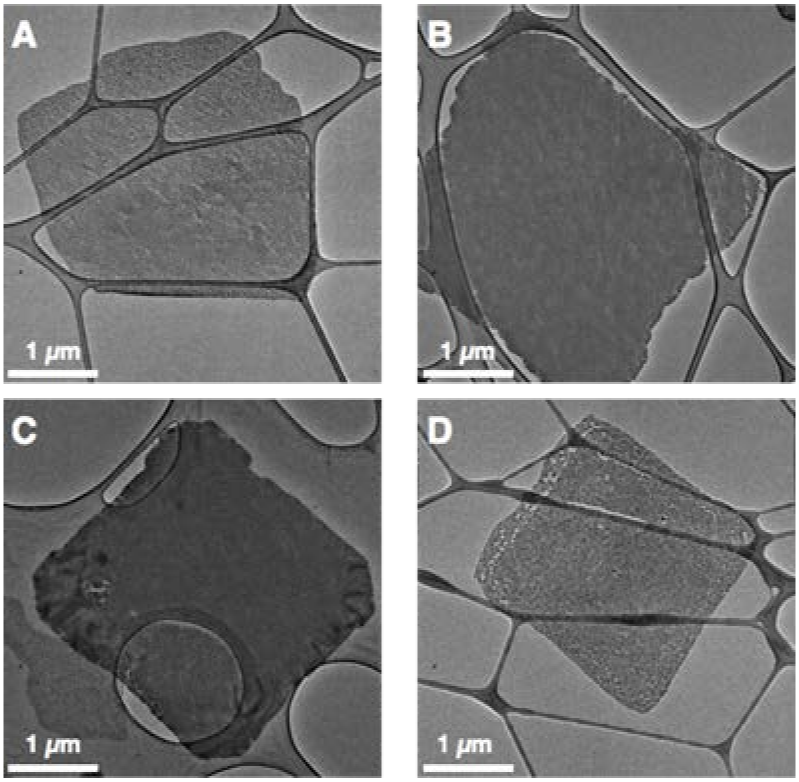

Fig. 4-9. More examples of the 2D sheets found in the TEM measurements. They all have similar size and shape.

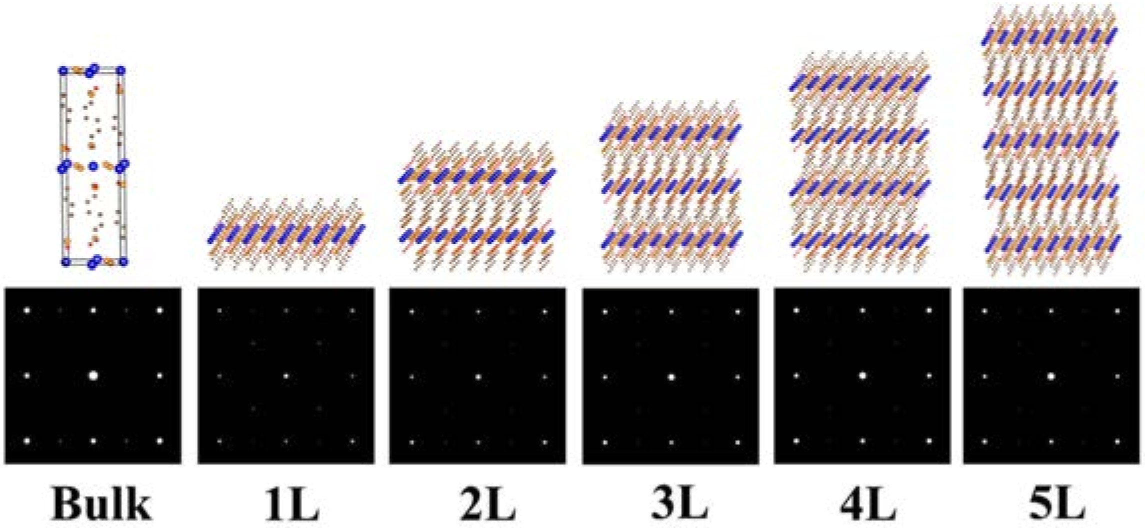

Fig. 4-10. Simulation of electron diffraction of bulk and 2D sheets with different thicknesses (from 1 layer to 5 layers). Upper row shows the structure models. For bulk $(C_4H_9NH_3)_2PbBr_4$, the unit cell was shown. For 2D sheets with different layers, 4×4×1 supercells were shown. Lower row shows the corresponding simulated electron diffraction patterns. All the structures exhibit strong (200) and (020) diffraction spots, while their intensities vary. The intensities of the main spots ((200) and (020)) increase as the layer thicknesses increase from 1 layer to 5 layers, and the bulk

has the strongest intensity. Looking into details of the minor spots, the bulk shows much stronger (210) diffraction spots (also see Fig. 4-11) than the 2D thin sheets. Different from the other well-known 2D materials, e.g. graphene, there is not any special stacking sequence among layers (e.g. AB…, ABC…). Therefore, the commonly used method to judge the layer thickness via the intensity ratio of two main spots fails here. Instead, we consider the feature of the (210) spot to be the criterion for roughly judging the thickness. Comparing with the bulk materials, the few-layer 2D sheets exhibit very weak (210) spots, and the weak (110) spots appear in the few-layer 2D sheets. However, the weak spots may not be observed experimentally due to the rapid radiation damage, and only the stronger (200) and (020) main points are maintained (see Fig. 4-11).

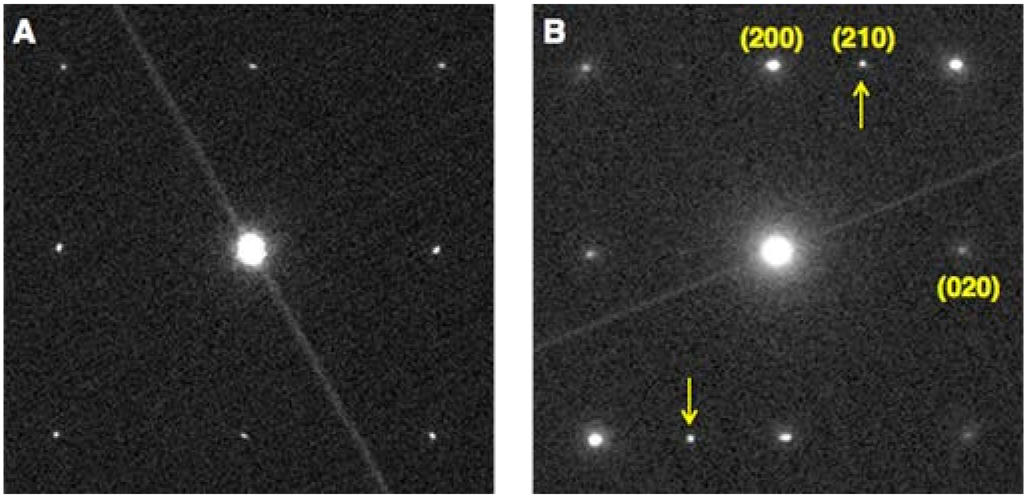

Fig. 4-11. Experimental electron diffraction patterns of thin-layer (A) and thick-layer (B) 2D sheets. In Fig. 4-11A, only (200) and (020) main spots can be observed, while apart from stronger main spots, there are also (210) spots in Fig. 4-11B as indicated by arrows. The diffraction pattern of Fig. 4-11B was acquired on a sheet with darker contrast in TEM, which was assumed to be thicker than that of Fig. 4-11A. The asymmetry of the intensity in Fig. 4-11B was attributed to the rolling-up of the sheet during the electron beam exposure, so that the sheet deviated from the zone axis. Hence, the experimental data supports the above simulation prediction (Fig. 4-10), that is, thin-layer sheet exhibit only (200) and (020) strong spots, while a thick-layer sheet is bulk-like and shows relatively stronger (210) spots. One point worth mentioning is that sometimes we indeed observe the very weak (210) spots in thin-layer sheets when we take a first look at the diffraction pattern. However, they disappeared so quickly because of the rapid radiation damage, which prevented them to be acquired by the camera even with very short exposure time. The (200) and (020) main spots may even only be visible for a few seconds.

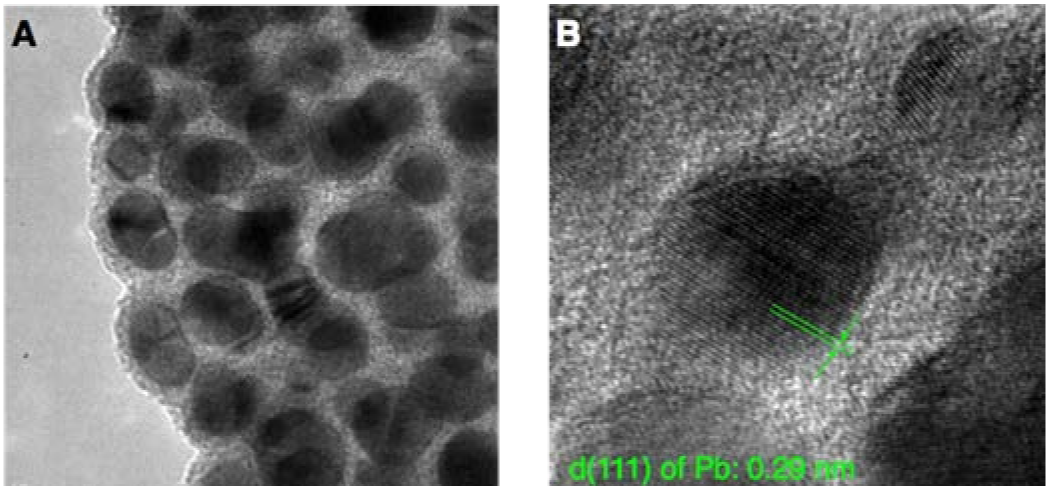

Fig. 4-12. HRTEM images of the 2D sheets. The sheet has already been damaged when magnification increases so that we cannot obtain an image of the perovskite lattice. Instead, we can observe lots of precipitates of Pb particles (Fig. 4-12A). A higher magnification in Fig. 4-12B shows the lattice image of one of the particles. The interplane distance was measured to be 0.29 nm, which agrees with the Pb (111) lattice distance and further confirms the presence of Pb precipitates.

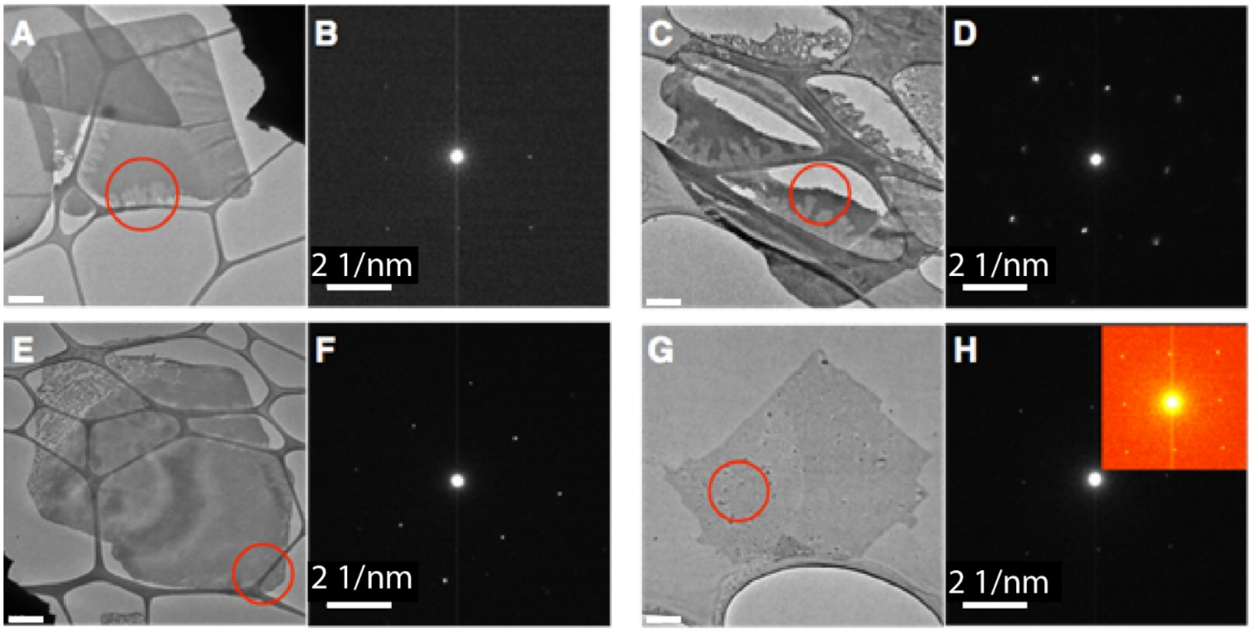

Fig. 4-13. More examples of the SAED patterns and their corresponding TEM images. The red circles indicate the selected area for diffraction. All the illumination conditions and exposure times were kept the same so that the thicker sheets may have stronger diffraction intensity (D and F), while that of the thinner sheets is weaker (B and H). For H, the intensity becomes too weak to be visible (inset shows the enhanced contrast with false color) and the corresponding sheet is assumed to be very thin. It is challenging to acquire SAED patterns in view of the rapid radiation damage. The method used here is to set the experimental diffraction conditions in advance, and then we

move the sample randomly in diffraction mode. We quickly acquired the SAED pattern once it was visible. Then we came back to the image mode with low dose, and gradually increased the dose rate to obtain a suitable contrast for TEM image acquisition. Sometimes, the sheets break or roll up during image acquisition (e.g. A and C).

In addition, we examined the Raman spectra of the bulk crystal and the thin sheet as shown in Fig. 4-14. The peaks found at 57.7 and 43.6 cm^{-1} for the bulk crystal shifted to 55.2 and 41.3 cm^{-1} for the 2D sheet, respectively. These peaks can be attributed to Pb-Br stretching and librational motions of both inorganic and organic ions, indicating that relaxation of the crystal lattice occurs in the thin sheets.[25] Meanwhile, the peak at 122.2 cm^{-1} (from -CH_3 group torsional motion and insensitive to lattice distortion) did not change. The peaks for the 2D sheet became narrower, suggesting better-defined vibrational states in the thin sheet. Furthermore, our density functional theory (DFT) calculation indicates a small lattice expansion of around 0.1 Å for the monolayer as compared to the bulk $(C_4H_9NH_3)_2PbBr_4$ crystal.

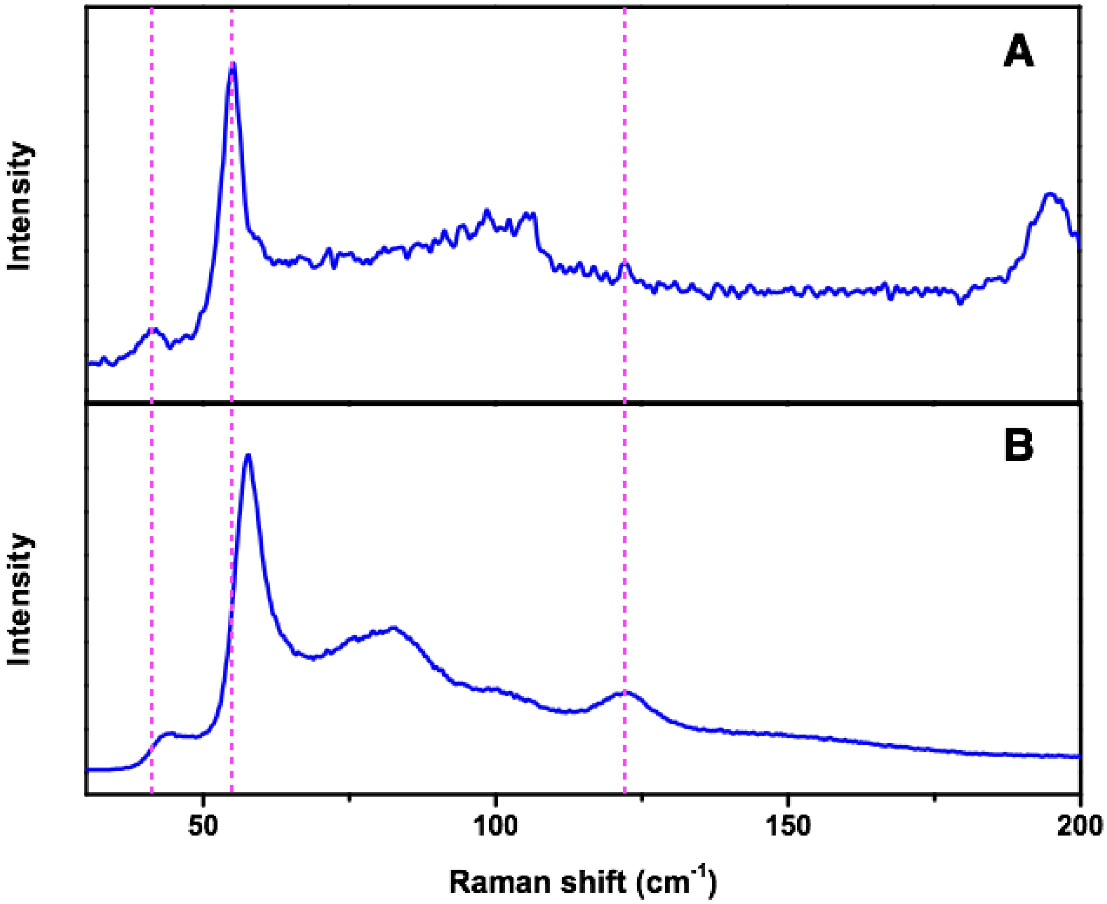

Fig. 4-14. Raman spectra of the 2D thin sheet and bulk crystal. (A) 2D sheet. (B) Bulk crystal. The signal at ~100 and 190 cm^{-1} in (A) are from substrate (Mica).

Strong crystal lattice distortions are common for hybrid perovskites.[5-10] Structural distortion induced optical and electronic changes have been reported in bulk hybrid perovskites.[26-

[29] Single-crystal XRD data of the bulk crystal of $(C_4H_9NH_3)_2PbBr_4$ revealed that the $PbBr_4^{2-}$ layer in the bulk crystal is highly distorted, with a Pb-Br-Pb bond angle of 152.94° (Fig. 4-15, Table 4-3, 4-4 for more details), which may provide driving forces for lattice relaxation in the 2D thin sheet. In other reported 2D materials, the in-plane crystal structure does not change from bulk to isolated sheets; and the optical and electronic properties change because of electronic decoupling between adjacent layers.

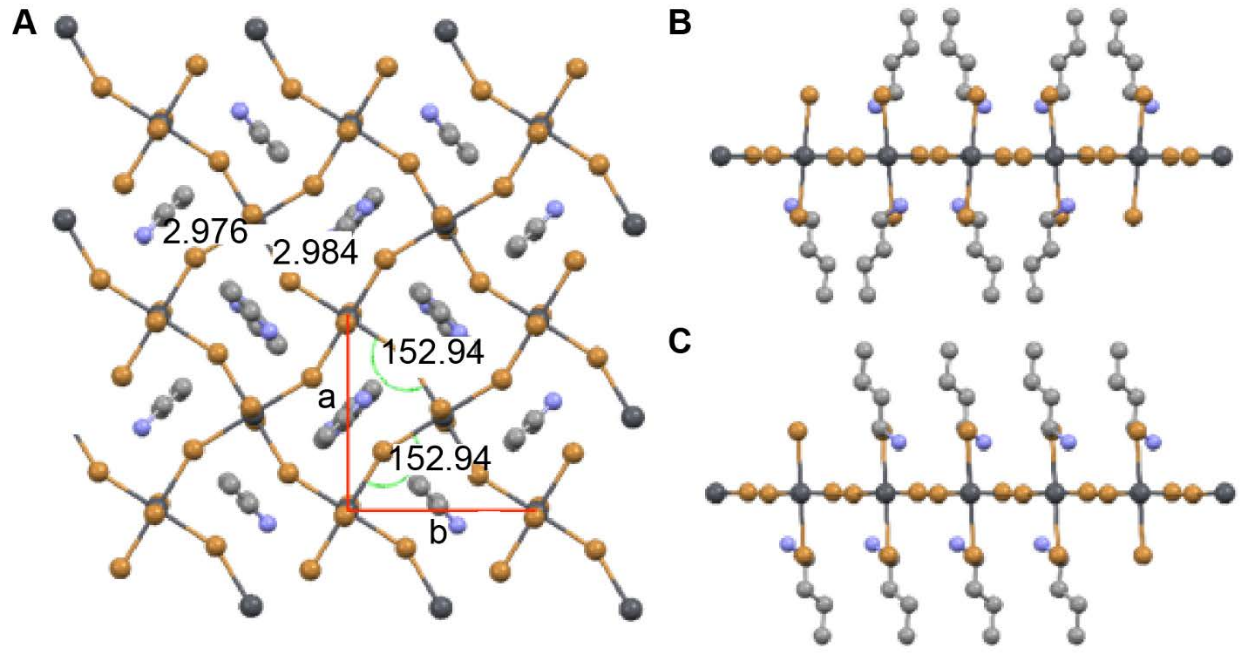

Fig. 4-15. Single crystal X-ray structure of bulk $(C_4H_9NH_3)_2PbBr_4$. (A) View from *c* axis. (B) View from *b* axis. (C) View from *a* axis. The Pb-Br-Pb bond angle is 152.94 °, which indicates a strong distortion in the *a*-*b* plane. For clarity, all hydrogen atoms were removed. Yellow balls, bromine atoms; black balls, lead atoms; grey balls, carbon atoms; blue balls, nitrogen atoms.

Table 4-3. Bond lengths [Å] and angles [°] for $(C_4H_9NH_3)_2PbBr_4$.

Bond	Length		Bond	Angle
C(1)-N(1)	1.493(6)		N(1)-C(1)-C(2)	111.1(4)
C(1)-C(2)	1.506(7)		N(1)-C(1)-H(1A)	109.4
C(1)-H(1A)	0.99		C(2)-C(1)-H(1A)	109.4
C(1)-H(1B)	0.99		N(1)-C(1)-H(1B)	109.4
C(2)-C(3)	1.512(6)		C(2)-C(1)-H(1B)	109.4
C(2)-H(2A)	0.99		H(1A)-C(1)-H(1B)	108
C(2)-H(2B)	0.99		C(1)-C(2)-C(3)	112.6(4)
C(3)-C(4)	1.519(8)		C(1)-C(2)-H(2A)	109.1

C(3)-H(3A)	0.99		C(3)-C(2)-H(2A)	109.1
C(3)-H(3B)	0.99		C(1)-C(2)-H(2B)	109.1
C(4)-H(4A)	0.98		C(3)-C(2)-H(2B)	109.1
C(4)-H(4B)	0.98		H(2A)-C(2)-H(2B)	107.8
C(4)-H(4C)	0.98		C(2)-C(3)-C(4)	112.4(5)
N(1)-H(1C)	0.91		C(2)-C(3)-H(3A)	109.1
N(1)-H(1D)	0.91		C(4)-C(3)-H(3A)	109.1
N(1)-H(1E)	0.91		C(2)-C(3)-H(3B)	109.1
Br(1)-Pb(1)	3.0138(5)		C(4)-C(3)-H(3B)	109.1
Br(2)-Pb(1)	2.9762(4)		H(3A)-C(3)-H(3B)	107.8
Br(2)-Pb(1)#1	2.9843(4)		C(3)-C(4)-H(4A)	109.5
Pb(1)-Br(2)#2	2.9762(4)		C(3)-C(4)-H(4B)	109.5
Pb(1)-Br(2)#3	2.9843(4)		H(4A)-C(4)-H(4B)	109.5
Pb(1)-Br(2)#4	2.9843(4)		C(3)-C(4)-H(4C)	109.5
Pb(1)-Br(1)#2	3.0138(5)		H(4A)-C(4)-H(4C)	109.5
			H(4B)-C(4)-H(4C)	109.5
			C(1)-N(1)-H(1C)	109.5
			C(1)-N(1)-H(1D)	109.5
			H(1C)-N(1)-H(1D)	109.5
			C(1)-N(1)-H(1E)	109.5
			H(1C)-N(1)-H(1E)	109.5
			H(1D)-N(1)-H(1E)	109.5
			Pb(1)-Br(2)-Pb(1)#1	152.940(17)
			Br(2)-Pb(1)-Br(2)#2	180
			Br(2)-Pb(1)-Br(2)#3	89.222(4)
			Br(2)#2-Pb(1)-Br(2)#3	90.778(4)
			Br(2)-Pb(1)-Br(2)#4	90.778(4)
			Br(2)#2-Pb(1)-Br(2)#4	89.222(4)
			Br(2)#3-Pb(1)-Br(2)#4	180
			Br(2)-Pb(1)-Br(1)	89.573(12)
			Br(2)#2-Pb(1)-Br(1)	90.429(12)
			Br(2)#3-Pb(1)-Br(1)	94.874(12)
			Br(2)#4-Pb(1)-Br(1)	85.126(12)
			Br(2)-Pb(1)-Br(1)#2	90.427(12)
			Br(2)#2-Pb(1)-Br(1)#2	89.571(12)
			Br(2)#3-Pb(1)-Br(1)#2	85.125(12)
			Br(2)#4-Pb(1)-Br(1)#2	94.875(12)
			Br(1)-Pb(1)-Br(1)#2	180.000(15)

Symmetry transformations used to generate equivalent atoms:
#1 x+1/2,-y+3/2,-z+1 #2 -x+1,-y+1,-z+1 #3 -x+3/2,y-1/2,z
#4 x-1/2,-y+3/2,-z+1

Table 4-4. Anisotropic displacement parameters (Å^{2}x 10^3) for $(C_4H_9NH_3)_2PbBr_4$. The anisotropic displacement factor exponent takes the form: $-2\pi^2[\ h^2a^{*2}U^{11} + ... + 2\ h\ k\ a^*\ b^*\ U^{12}\ ]$.

	U^{11}	U^{22}	U^{33}	U^{23}	U^{13}	U^{12}
C(1)	21(2)	24(2)	12(3)	1(2)	1(2)	2(2)
C(2)	19(2)	15(2)	14(3)	1(2)	0(2)	6(2)
C(3)	25(3)	33(3)	21(3)	7(2)	-5(2)	-2(2)
C(4)	35(3)	62(4)	21(3)	13(3)	-5(3)	-3(3)
N(1)	16(2)	15(2)	12(2)	0(2)	3(2)	-1(2)
Br(1)	16(1)	14(1)	12(1)	1(1)	-2(1)	2(1)
Br(2)	13(1)	12(1)	17(1)	-1(1)	2(1)	-4(1)
Pb(1)	9(1)	8(1)	10(1)	0(1)	0(1)	0(1)

4.5 Optical Properties of Ultrathin Layered Halide Perovskite Sheets:

We investigated the photoluminescence (PL) properties of individual 2D crystals under 325-nm laser excitation. Fig. 4-16A shows the PL spectra of the bulk $(C_4H_9NH_3)_2PbBr_4$ crystal and 2D sheets with different thickness (22, 8, and 3 layers thick) and Fig. 4-16, B to E, shows the corresponding PL image of each sheet. Both the bulk materials and the sheets exhibit similar strong purple-blue light emission. The bulk crystal has an emission peak at 411 nm (2.97 eV) and the 2D sheets have slightly blue-shifted peaks at ~ 406 nm (3.01 eV). The slightly increased optical band gap for the ultrathin 2D sheets is likely induced by the lattice expansion. Our DFT simulation also suggests a 20 meV blue shift in PL for the few layer 2D sheets, which is a trend consistent with the experimental observation.[21] The 2D sheets with different thickness (from 22 to 3 layers) have similar PL spectra, the peak position shift is within 1 nm, and any lattice constant difference is within the experimental error from SAED observed between these samples.

Cathodoluminescence microscopy, a technique that provides a map of the light emitted from a sample when excited by a focused electron beam with excellent lateral resolution, was used to determine the spatial distribution of emissive sites on the 2D sheets. As shown in Fig. 4-16, the cathodoluminescence mapping from 395 to 435 nm shows a square shape identical to the corresponding scanning electron microscopy (SEM) images as shown in Fig. 4-16F, indicating the emission is from the whole square. The PL internal quantum efficiency (QE) of the 2D sheets was estimated by comparing the integrated PL intensity (from 390 to 450 nm) of the band edge emission at room temperature (298 K) and helium cryogenic temperature (6 K) and the results are shown in Fig. 4-16H.[30] There is a small red shift of the main peak from 406 to 412 nm as the temperature decreases. The emission at 421 nm (2.91 eV) at 6 K is known from the Γ_1^- state, which cannot be distinguished with the Γ_2^- state at room temperature (*26*). The PL QE for the 2D sheet is calculated to be ~26%, which is much higher than the QE of the bulk crystal (<1%), indicating the high quality of the single crystalline 2D sheets. The PL intensity increased linearly as the excitation power increased (Fig. 4-17), suggesting the PL QE was constant within our measurement range. The PL lifetime of the 2D sheets was measured by time resolved photoluminescence. As shown in Fig. 4-16I, the decay curve showed a bi-exponential feature with lifetimes of 0.78 ns (67%) and 3.3 ns (33%), near the reported data for the bulk crystals.[15]

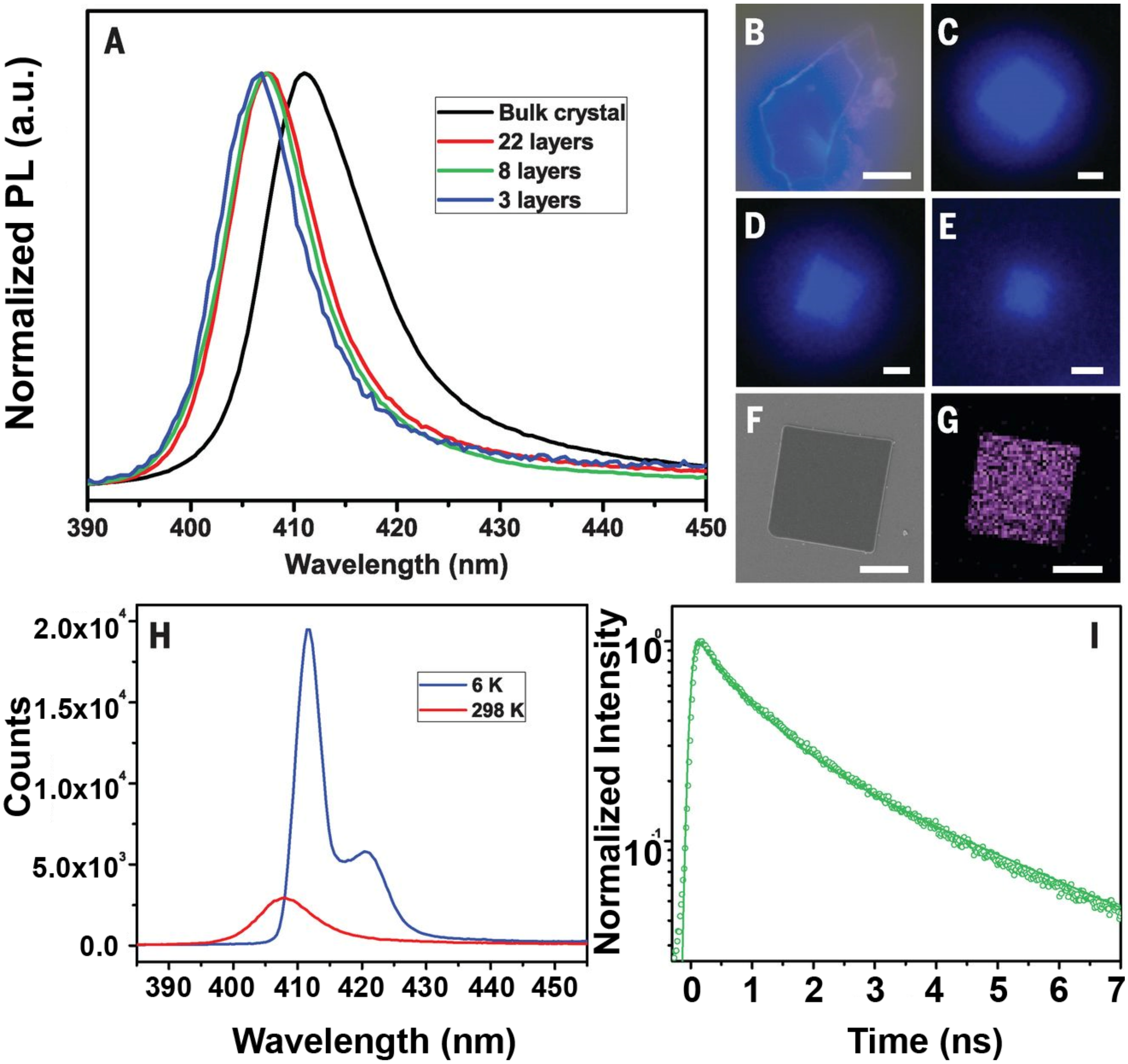

Fig. 4-16. Photoluminescence properties of the 2D $(C_4H_9NH_3)_2PbBr_4$ sheets. (A) Steady-state PL spectrum of a piece of bulk crystal and several 2D sheets under a 325 nm laser excitation. (B) The corresponding optical image of the bulk crystal under excitation. The scale bar is 20 μm. (C-E) Optical images of the 2D sheets with 22 layers, 8 layers, and 3 layers thick. The scale bars are 2 μm. (F) Scanning electron microscope image of a 2D sheet. The scale bar is 2 μm. (G) The corresponding cathodoluminescence image showing the emission (with a 40 nm band pass filter centered at 415 nm). (H) PL spectra of a 2D sheet at 298 K and 6 K. (I) Time resolved PL measurements showing a bi-exponential decay.

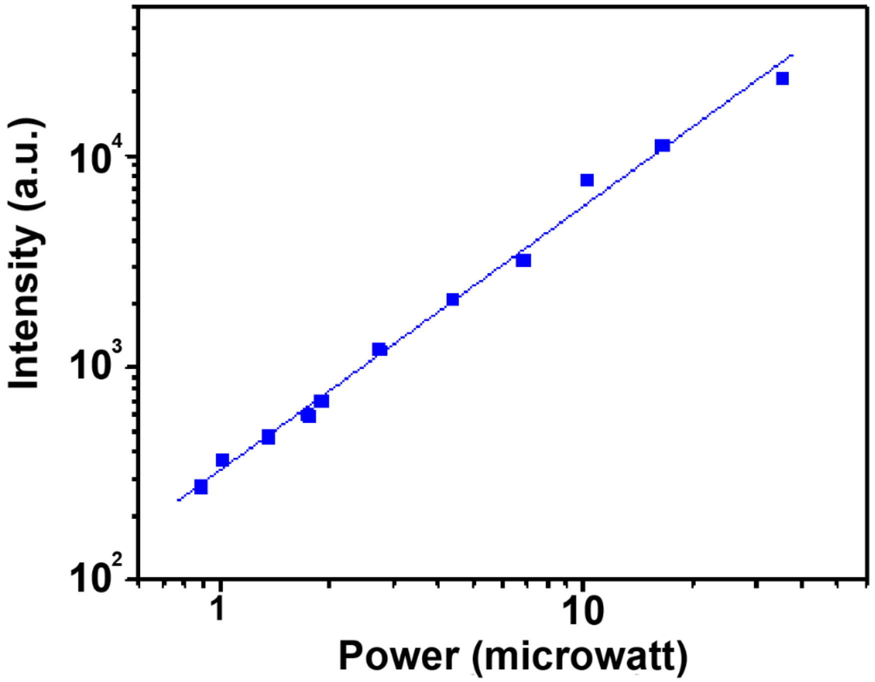

Fig. 4-17. Excitation power dependence of the photoluminescence as measured at room temperature.

4.6 Tunability of Ultrathin Layered Perovskites:

The chemistry of synthesizing these ultrathin 2D sheets was extended to other hybrid perovskites. We prepared $(C_4H_9NH_3)_2PbCl_4$, $(C_4H_9NH_3)_2PbI_4$, $(C_4H_9NH_3)_2PbCl_2Br_2$, $(C_4H_9NH_3)_2PbBr_2I_2$, and $(C_4H_9NH_3)_2(CH_3NH_3)Pb_2Br_7$ ultrathin 2D sheets using similar methods, and their PL spectra and optical images are shown in Fig. 4-18 (see Fig. 4-18 for XRD and Fig. 4-19 for AFM images). For the $(C_4H_9NH_3)_2PbCl_4$ sheet (i), the band edge emission was in the ultraviolet at ~340 nm, which was beyond our detection range for the single sheet measurement. Interestingly, three states in the visible region were observed at 486, 568, and 747 nm, which made the sheets appear nearly white. This emission is attributed to the transient formation of self-trapped excitons.[31] For the $(C_4H_9NH_3)_2PbI_4$ sheet (iii), the band edge emission was at 514 nm, which is 9 nm blue-shifted compared to the bulk.[5] This blue shift is consistent with the bromide case (ii) discussed above. For the chloride-bromide alloy crystal, $(C_4H_9NH_3)_2PbCl_2Br_2$ (iv), the band edge emission peak was at 385 nm and a broad self-trapped exciton emission appeared at longer wavelength. However, the bromide-iodide alloy (v) showed only one peak at 505 nm. In the case of $(C_4H_9NH_3)_2(CH_3NH_3)Pb_2Br_7$, no well-defined squares were observed and the thickness of the plates was ~10 nm. Preliminary PL study indicates a band edge emission at 453 nm, which is red-shifted slightly compared to the bulk. These results indicate that the 2D hybrid perovskites have excellent composition and color tunability.

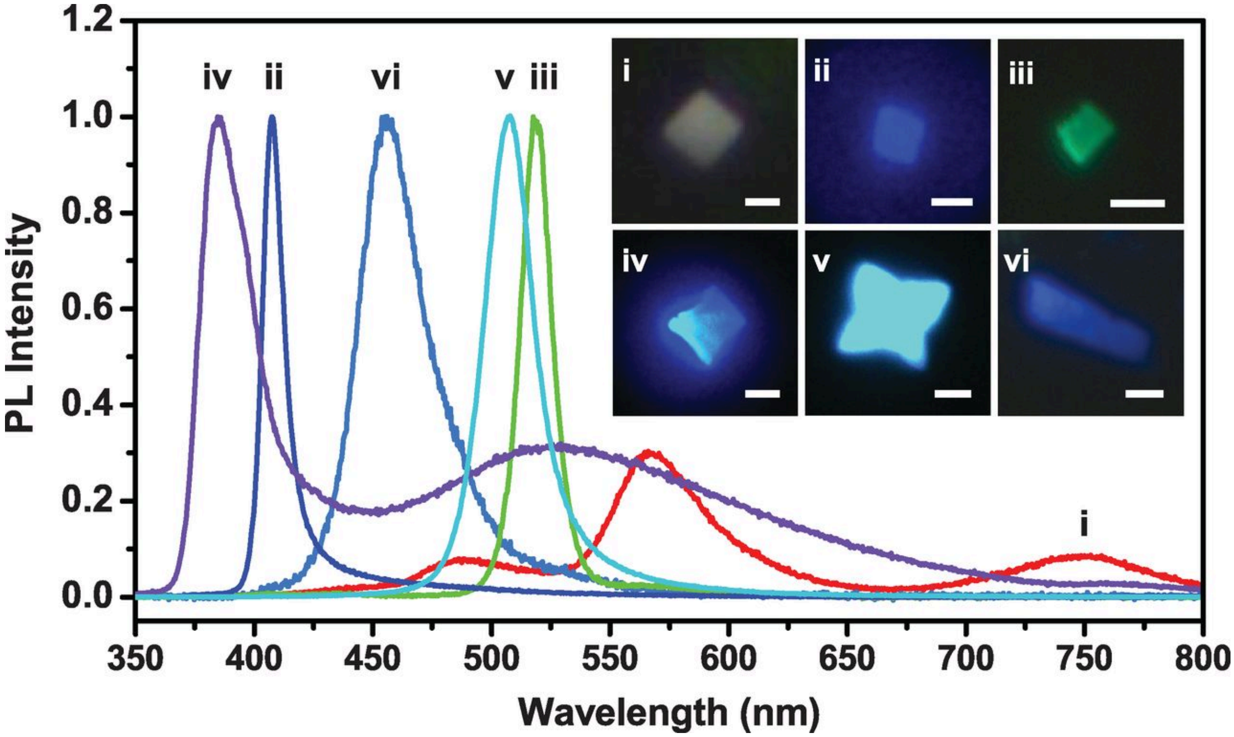

Fig. 4-17. Photoluminescence of different 2D hybrid perovskites. $(C_4H_9NH_3)_2PbCl_4$ (i), $(C_4H_9NH_3)_2PbBr_4$ (ii), $(C_4H_9NH_3)_2PbI_4$ (iii), $(C_4H_9NH_3)_2PbCl_2Br_2$ (iv), $(C_4H_9NH_3)_2PbBr_2I_2$ (v), and $(C_4H_9NH_3)_2(CH_3NH_3)Pb_2Br_7$ (vi) 2D sheets demonstrate that the solution phase direct growth method is generalizable. The corresponding optical PL images are shown in the inset. Scale bars are 2 μm for (i)-(v); 10 μm for (vi).

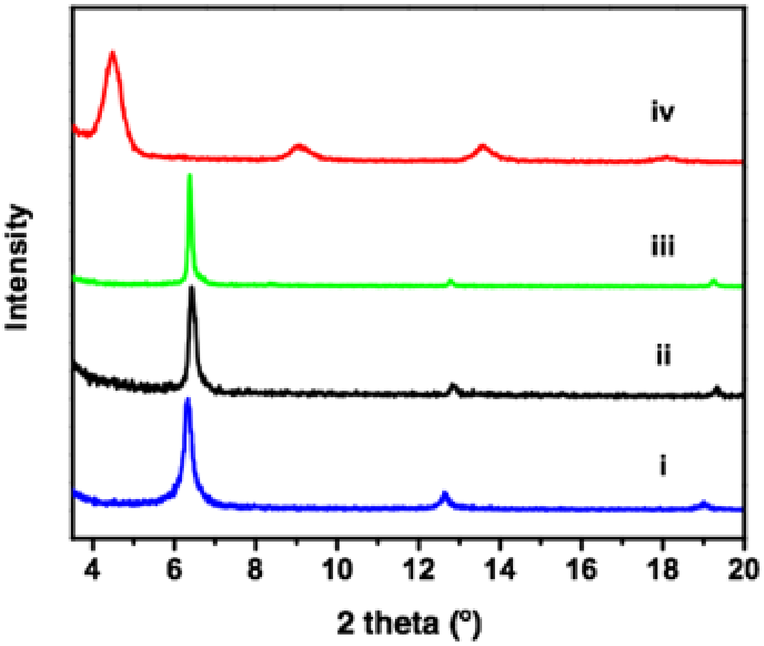

Fig. 4-18. X-ray diffraction spectra of $(C_4H_9NH_3)_2PbCl_4$ (i), $(C_4H_9NH_3)_2PbBr_4$ (ii), $(C_4H_9NH_3)_2PbI_4$ (iii), and $(C_4H_9NH_3)_2(CH_3NH_3)Pb_2Br_7$ (iv) 2D sheets.

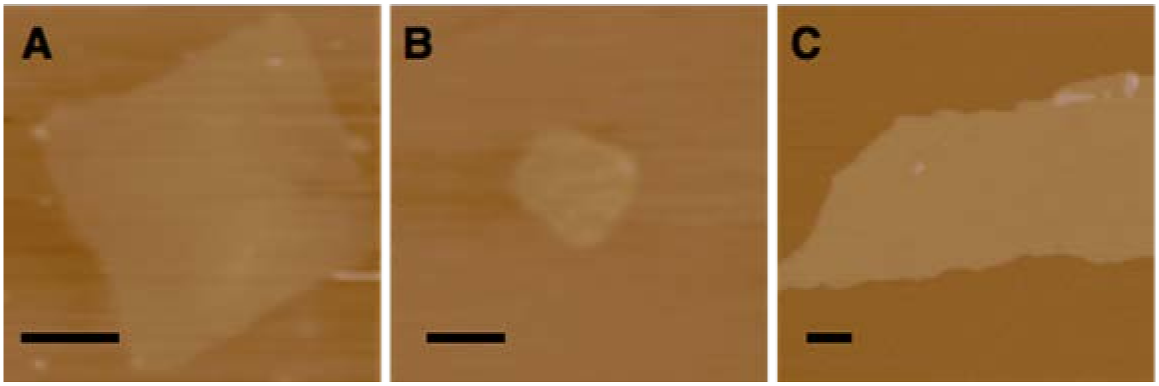

Fig. 4-19. AFM images of $(C_4H_9NH_3)_2PbCl_4$ (A), $(C_4H_9NH_3)_2PbI_4$ (B), and $(C_4H_9NH_3)_2(CH_3NH_3)Pb_2Br_7$ (C) 2D sheets with 5, 2, and 4 layers thick; respectively. Scale bars are 2 μm.

4.7 Chapter 4 Conclusions:

The direct growth of atomically thin sheets overcomes the limitations of the conventional exfoliation and chemical vapor deposition methods, which normally produce relatively thick perovskite plates.[17-19, 32, 33] These materials are solution-processable, and their structure, composition, and optical/electrical properties are highly tunable by simply varying the organic and inorganic precursors in solution. In contrast to other 2D materials, the structural framework of hybrid perovskites is flexible and deformable; and different from the bulk crystal, the thin 2D sheets exhibit new features such as structural relaxation and PL shift. This study opens up opportunities for fundamental research on the synthesis and characterization of atomically thin 2D hybrid perovskites, and introduces a new family of 2D solution-processed semiconductors for nanoscale optoelectronic devices such as field effect transistors, photodetectors, and light emitting diodes.

4.8 Chapter 4 Methods:

Synthesis of the 2D hybrid perovskites.

Reagents: Unless otherwise stated, all of the chemicals were purchased from Sigma-Aldrich and used as received.

Synthesis of $C_4H_9NH_3Br$: 10 mL of butylamine and 25 mL of methanol were added to a 250 mL round bottom flask. The mixture was stirred and maintained at 0 °C using an ice-water bath. 10 mL of HBr (50 wt% in water) was added to the mixture dropwise. The ice-water bath was removed and the mixture was stirred at room temperature for 2 hours. The solvent (methanol and water) was then removed by a rotary evaporator at 70 °C. The crude oil-like material was washed with diethyl ether by stirring the solution for 30 min, a step which was repeated for three times, and finally recrystallized from a mixed solvent of diethyl ether and ethanol. After filtration, the white solid was collected and dried at 60 °C in a vacuum oven for 24 h. Another related chemical, CH_3NH_3Br, was purchased from 1-material Inc. and used without further purification.

Growth of $(C_4H_9NH_3)_2PbBr_4$ thin sheets: All the solution preparation and thin sheets growth were carried out inside an argon-filled glove box with oxygen and water levels less than 1 ppm. The as-synthesized $C_4H_9NH_3Br$ (308 mg, 2 mmol) and $PbBr_2$ (367 mg, 1 mmol) were dissolved in 2 mL of anhydrous dimethylformide (DMF) inside a 4 mL vial. The solution was then diluted 100 times by a DMF/chlorobenzene (1:1 volume ratio) co-solvent. Before use, the diluted solution was further diluted 10 times by either chlorobenzene (CB) or CB/acetonitrile (2:1 volume ratio) co-solvent. Si/SiO_2 was used as the substrate for the 2D perovskite growth. Si/SiO_2 substrates were cleaned by ultra-sonication in isopropanol, acetone, water, and isopropanol again for 5 min and then dried by a nitrogen gun. The substrates were then transferred into a glove box and preheated at 75 °C on a hot plate. 10 µL of the diluted solution was dropped onto the Si/SiO_2 surface and dried at 75 °C for 10 min. Thin sheets of $(C_4H_9NH_3)_2PbBr_4$ grew spontaneously as the solvent evaporated. All other chloride, iodide, and alloy derivatives were synthesized using a similar procedure.

Growth of $(C_4H_9NH_3)_2(CH_3NH_3)Pb_2Br_7$ thin sheets: All the steps were the same as above except for the solution preparation: $C_4H_9NH_3Br$ (154 mg, 1 mmol), CH_3NH_3Br (56 mg, 0.5 mmol) and $PbBr_2$ (367 mg, 1 mmol) were dissolved in 2 mL of anhydrous dimethylformide (DMF) inside a 4 mL vial.

Mechanical exfoliation of the $(C_4H_9NH_3)_2PbBr_4$ thin sheets: Single crystals of $(C_4H_9NH_3)_2PbBr_4$ were prepared by the slow cooling of the hot solution (90 °C) of $C_4H_9NH_3Br$ (308 mg, 2 mmol) and $PbBr_2$ (367 mg, 1 mmol) in a 20 mL DMF/toluene mixture with 2 drops of HBr aqueous solution. The sheet-like crystals were then attached to a regular piece of scotch tape, and the part of the tape with the crystals was refolded upon a clean adhesive section of the same piece of tape. The two layers were then pressed firmly together for several seconds. The tape was gently unfolded so that two mirrored crystal areas on the tape remained. This process was repeated for 4 to 5 times. Then the Si/SiO_2 substrate was placed shiny-side down on an area with the crystals and pressed firmly to the tape for several seconds. It was then gently removed, and the sample was washed in hexanes.

Solvent exfoliation of the $(C_4H_9NH_3)_2PbBr_4$ thin sheets: 1 mg of the $(C_4H_9NH_3)_2PbBr_4$ single crystal was added to 2 mL of anhydrous hexanes and the mixture was ultra-sonicated for 10 min to fully exfoliate and disperse the material. The suspension was then diluted 10 times by hexanes. 10 µL of the diluted solution was drop-casted on the Si/SiO_2 substrate and dried at 60 °C for 10 min.

Characterization of the 2D hybrid perovskites.

Optical microscopy (OM) measurements: OM images of the thin sheets were taken using a Zeiss Axio Scope.A1 in dark field mode. The 2D hybrid perovskites, which were directly grown, drop-casted from hexane dispersion, and mechanically exfoliated on Si/SiO$_2$ substrate, were used for the measurements.

Atomic force microscopy (AFM) measurements: AFM images of the thin sheets were taken using an Asylum MFP 3D in tapping mode. The 2D hybrid perovskites directly grown, drop-casted from hexane dispersion, and mechanically exfoliated on Si/SiO$_2$ substrate were used for the measurements.

X-ray diffraction (XRD) measurements: Powder X-ray diffraction was measured using a Bruker AXS D8 Advance diffractometer with a Cu K$_\alpha$ source. Single crystal X-ray diffraction was measured using an APEX II QUAZAR diffractometer with a Mo K$_\alpha$ source and an APEX II detector. A colorless plate 0.040 x 0.040 x 0.020 mm in size was mounted on a Cryoloop with Paratone oil. Data were collected in a nitrogen gas stream at 100(2) K using phi and omega scans. The crystal-to-detector distance was 40 mm and the exposure time was 10 seconds per frame using a scan width of 2.0°. Data collection was 100.0% complete to 25.000° in □. A total of 28141 reflections were collected covering the indices, -9<=*h*<=9, -9<=*k*<=9, -33<=*l*<=33. 1678 reflections were found to be symmetry independent, with a R$_{int}$ of 0.0376. Indexing and unit cell refinement indicated a primitive, orthorhombic lattice. The space group was found to be P b c a (No. 61). The data were integrated using the Bruker SAINT software program and scaled using the SADABS software program. Solution by iterative methods (SHELXT) produced a complete heavy-atom phasing model consistent with the proposed structure. All non-hydrogen atoms were refined anisotropically by full-matrix least-squares (SHELXL-2014). All hydrogen atoms were placed using a riding model. Their positions were constrained relative to their parent atom using the appropriate HFIX command in SHELXL-2014.

Transmission electron microscopy (TEM) and energy dispersive spectroscopy (EDS) measurements: To grow the 2D sheets on TEM grids, lacy carbon TEM grids were put on the surface of a Si/SiO$_2$ substrate and a drop of the dilute solution was added and dried at 70 °C. All TEM images and SAED patterns were acquired using FEI TitanX 60-300 microscope operated at 60kV. Before taking SAED patterns, the camera was calibrated using a standard copper film calibration sample. The electron diffraction simulation was performed using the MacTempas software (1). Structure models (Fig. 4-1a, Fig. 4-10) were drawn using the VESTA software (2).

Grazing incidence wide angle X-ray scattering (GIWAXS): GIWAXS spectra were taken at beamline 7.3.3. at the Advanced Light Source (ALS) at Lawrence Berkeley National Lab utilizing an incident wavelength of 10 keV. 2D spectra were recorded with a Pilatus 2M-2D detector and integrated to 1D with NIKA GIWAXS software.

Steady state photoluminescence (PL) measurements: Photoluminescence measurements were performed using the 325 nm He:Cd laser. The full intensity of the beam is 5 mW. Using an iris diaphragm and a focusing lens, a Gaussian beam spot with a waist of approximately 30 μm was obtained and used to excite individual 2D sheets. The output power of the excitation source was adjusted by neutral density filters (normally 1 ~ 100 μW) and monitored with an external energy meter. Emission from 2D sheets was collected with a dark-field microscope objective (Nikon 50×, N.A. 0.55, in a Nikon ME600 optical microscope) and routed via a bundled optical fiber to a UV-vis spectroscopy spectrometer (Princeton Instruments/Acton) equipped with a 1200 groove/mm grating blazed at 300 nm and a liquid N_2-cooled charge-coupled device. During the measurement, the sample was placed in a vacuum chamber with a vacuum level of 2×10^{-3} torr. For the low temperature measurements, liquid helium was used to keep the sample at about 6 K and the vacuum was maintained at 2×10^{-6} torr to avoid moisture condensing on the sample. There was no obvious sample damage by laser during the measurement. Internal QE was calculated from the ratio of the integrated PL signal of a 2D sheet at 298K and 6K.

Time-resolved photoluminescence (TRPL) measurements: Time resolved photoluminescence was collected on a Picoquant Fluotime 300 with PMA 175 detector and an LDH-P-C-405 diode laser (excitation wavelength of 407.1 nm) at room temperature.

Raman spectroscopy: The Raman spectra were taken by a Horiba HR800 system with laser excitation wavelength of 780 nm. The laser is focused to a diameter of 2 mm and has a power of 300 mW. For the Raman measurement, 2D crystals were grown on Mica instead of Si/SiO_2 to avoid a strong background signal. The signals at 100 and 200 cm^{-1} are from the Mica substrate.

Cathodoluminescence measurements: Cathodoluminescence (CL) images were acquired with a modified Zeiss Gemini SUPRA 55 Scanning Electron Microscope (SEM). An aluminum parabolic reflector was positioned above the same sample in order to couple a 1.3π sr of emission outside of the vacuum chamber through a quartz window. Emission at 410 nm was collected using a H7360-01 photon counting head (Hamamatsu) with a 40 nm bandpass filter centered at 415 nm. All images were acquired at 3 kV with 512 x 512 pixels and a scanning rate of 10 ms/line.

Density functional theory (DFT) simulations: The calculations are based on density functional theory within the generalized gradient approximation (GGA) formulated by Perdew, Burke, and Ernzerhof (PBE) as implemented in VASP code. The projector augmented wave (PAW) pseudopotentials are employed, and the valence wavefunctions are expanded in a plane-wave basis with an energy cutoff of 400 eV. For the lattice constant calculations, the primitive cell is employed and the Brillouin zone integration is sampled with a $3 \times 3 \times 1$ k-point mesh. Larger energy cutoffs and finer k-point meshes have been tested, and the difference is negligible.

The calculated in-plane lattice constants are 8.27 and 8.46 Å for the monolayer; 8.25 and 8.40 Å for the bulk crystal. The lattice constant of the bulk is in good agreement with the experimental values. The slight overestimate is well known in PBE functional calculations. The calculated lattice constant of the single layer is ~0.1 Å larger than that of the bulk, which is however, smaller than the experimental lattice expansion. Because we calculate isolated material, and the substrate effect is not taken into account, the large lattice expansion in experiments may be induced by the substrate and needs further investigation. The calculated band gap for bulk crystal is 2.57 eV, few layer sheet is 2.59 eV. These values are consistent with the experimental results.

4.9: Chapter 4 Supplemental Text

Discussion of the synthetic conditions for the ultrathin 2D hybrid perovskite crystals.

Many parameters affect the growth of the 2D sheets, and the parameter range is flexible within a certain degree. Under the optimized condition, the volume ratio of DMF, CB, and acetonitrile is around 1:13:6. We found that it is necessary to have 4% ~ 6% DMF to facilitate the dissolution of the precursors (because without DMF, the precursors cannot dissolve). Between 25% to 40% acetonitrile is required to achieve square-shaped 2D sheet formation. The growth temperature can be from 60 to 100 °C. Lower temperatures led to particles with random shape and higher temperatures damaged the 2D sheets and resulted in poor surface morphology. We varied the concentration of the precursors and found the 2D sheets form within a window of 0.02% ~ 0.04% by weight. Lower concentration gave only small dots and higher concentration gave large particles with random shapes. We also note that the 2D sheets can grow on different substrates such as Si/SiO_2, Si, quartz, Mica, aluminum foil, etc.

The role of acetonitrile: We noticed that if using a DMF/CB binary solvent, DMF is “too good” of a solvent and CB is “too bad” of a solvent for the hybrid perovskites, and the ratio of DMF to CB is hard to control to achieve effective crystallization during solvent evaporation. The purpose underlying the use of an intermediate solvent, such as acetonitrile, is to balance the dissolution and crystallization of the 2D hybrid perovskites. Acetonitrile has a higher vapor pressure and can leave the solution more quickly under heating, so the CB:DMF ratio increases and induces the crystal formation. Any further role of acetonitrile in the growth mechanism is still unclear. Further study is necessary to fully understand the mechanism.

We noticed that the thickness distribution is quite wide (from ~2 to ~50 nm) and the average thickness (number of layers) is dependent on growth temperature and solution concentration. Under the optimized condition (75 °C, 0.03%), the average thickness is ~10 nm. Higher concentration (75 °C, 0.04%) gave relatively thicker samples with an average of ~15 nm. We also found slightly higher or lower temperature all gave relatively thicker samples. Although we observe some initial trend, there was sample-to-sample variation, which is possibly because there may be more factors that need to be taken into account. A more detailed study has been carried out to fully understand the growth mechanism as well as to achieve more precise control of the lateral size and thickness of the 2D sheets.

Discussion on the PL of the ultrathin 2D hybrid perovskite crystals.

The blue shift of the PL is probably from the structural relaxation of the in-plane crystal lattice. Our TEM and GIWAXS measurements show a slight increase of the in-plane lattice constant for the few layer samples, as compared to the bulk crystal, and the lattice expansion should lead to a small increase of the band gap. To confirm this, we have carried out DFT simulations (showing that the calculated band gap for the bulk crystal is 2.57 eV, while the band gap of the few layer sheet is 2.59 eV). The reason that the PL of the 22-layer sample is more close to that of the 8-layer and 3-layer samples but far from the bulk is probably because the bulk crystal is much thicker (at least several micrometers, over 500 layers) than the 22-layer and 8-layer samples and possesses a slightly different lattice constant. As a result, the structure of the 22-layer sample is more close to the 8-layer and 3-layer samples (indeed the lattice constant calculated from TEM diffraction pattern for thinner and thicker sheets are very similar), but these thin sheets are more different from the bulk crystal. Furthermore, we cannot rule out that the blue shift may also be related to a reduction in the image charge effect coupling excitons between layers or to a change in the dielectric environment, but we currently do not have direct evidence.

There are two possible effects that may contribute to the asymmetric peak shape of the PL emission. One contributing effect is the existence of the Γ_2^- and the Γ_1^- excitonic states in the energy range plotted. As proposed in ref. 26 in the main text, these states emerge because of the splitting of the energy levels caused by the exchange interactions between the electron and hole within the layered perovskite. As shown in Fig. 4-16H in the main text, these states can be distinguished by PL at 6K with the Γ_1^- state being slightly red-shifted and less bright relative to the Γ_2^- state, but these states cannot be clearly resolved at room temperature, which may contribute to the asymmetry of the PL peak. A second possible contributing effect stems from the coupling of the excitonic states to phonons, which has been proposed in related materials such as for $(C_6H_5C_2H_4\text{-}NH_3)_2PbI_4$ by Gauthron et al. (ref. 17) and for $(C_4H_9NH_3I)_2(PbI_2)$ by Wu et al. (ref. 31). In both cases, the PL reported in these works showed a broad lower energy tail, which was attributed to these interactions. In the work by Wu et al., it was proposed that the exciton-phonon interactions lead to the formation of self-trapped excitons. In the case of PL broadening from self-trapping, the few layer 2D sheet would still be expected to exhibit this self-trapping behavior, as the deformation energy would remain low as the number of layers decreases. Therefore, we believe that it is likely that a 3-layer $(C_4H_9NH_3)_2PbBr_4$ sheet may experience this effect strongly, which may explain the asymmetric PL from the sample.

4.10: Chapter 4 References

1. Lee, M. M.; Teuscher, J.; Miyasaka, T.; Murakami, T. N.; Snaith, H. J. *Science* **2012**, 338, 643-647.
2. Burschka, J.; Pellet, N.; Moon, S.-J.; Humphry-Baker, R.; Gao, P.; Nazzeeruddin, M. K.; Gratzel, M. *Nature,* **2013**, 499, 316-319.
3. Dou, L.; Yang, Y. M.; You, J.; Hong, Z.; Chang, W.-H.; Li, G.; Yang, Y. *Nature Commun*. **2014**, 5, 5404.
4. Zhou, H.; Chen, Q.; Li, G.; Luo, S.; Song, T.-B.; Duan, H.-S.; Hong, Z.; You, J.; Liu, Y.; Yang, Y. *Science* **2014**, 345, 542-546.
5. Mitzi, D. B. *Prog. Inorg. Chem*. **2007**, 48, 1-121.
6. Papavassiliou, G. C. *Prog. Solid State Chem*. **1997**, 25, 125-270.
7. Mitzi, D. B. *J. Chem. Soc., Dalton Trans*. **2001**, 1-12.
8. Lanty, G.; Jemli, K.; Wei, Y.; Leymarie, J.; Even, J.; Lauret, J.-S.; Deleporte, E. *J. Phys. Chem. Lett.* **2014**, 5, 3958-3963.
9. Borriello, I.; Cantele, G.; Ninno, D. *Phys. Rev. B* **2008**, 77, 235214.
10. Meresse, A.; Daoud, A. *Acta Cryst*. 1989, C45, 194-196.
11. Ishihara, T.; Takahashi, J.; Goto, T. *Solid State Commun*. **1989**, 69, 933-936.
12. Willett, R.; Place, H.; Middleton, M. *J. Am. Chem. Soc.* **1988**, 110, 8639-8650.
13. Calabrese, J.; Jones, N. L.; Harlow, R. L.; Herron, N.; Thorn, D. L.; Wang, Y. *J. Am. Chem. Soc*. **1991**, 113, 2328-2330.
14. Mitzi, D. B.; Wang, S. Feild, C. A.; Chess, C. A.; Guloy, A. M. *Science*, **1995**, 267, 1473-1476.
15. Kawano, N.; Koshimizu, M.; Sun, Y.; Yahaba, N.; Fujimoto, Y.; Yanagida, T.; Asai, K. *J. Phys. Chem. C* **2014**, 118, 9101-9106.

16. Takeoka, Y.; Asai, K.; Rikukawa, M.; Sanui, K. *Bull. Chem. Soc. Jpn*. **2006**, 79, 1607-1613.
17. Gauthron, K.; Lauret, J-S.; Doyennette, L.; Lanty, G.; Al Choueiry, A.; Zhang, S. J.; Brehier, A.; Largeau, L.; Mauguin, O.; Bloch, J.; Deleporte, E. *Opt. Express* **2010**, 18, 5912-5919.
18. Niu, W.; Eiden, A.; Prakash, G. V.; Baumberg, J. J. *Appl. Phys. Lett*. **2014**, 104, 171111.
19. Ha, S. T.; Liu, X.; Zhang, Q.; Giovanni, D.; Sum, T. C.; Xiong, Q. *Adv. Opt. Mater.* **2014**, **2**, 838-844.
20. Green, M. A.; Baillie, A. H.; Snaith, H. *Nature Photon*. **2014**, 8, 506-514.
21. Dou, L.; Wong, A. B.; Yu, Y., Lai, M.; Kornienko, N.; Eaton, S. W.; Fu, A.; Bischak, C. G.; Ma, J.; Ding, T.; Ginsberg, N. S.; Wang, L.-W.; Alivisatos, A. P.; Yang, P. *Science*, **2015**, 349, 1518-1521.
22. Mercier, N.; Poiroux, S.; Riou, A.; Batail, P. *Inorg. Chem*. **2004**, 43, 8361-8366.
23. G. Cunningham et al., *ACS Nano* **6**, 3468–3480 (2012).
24. L. W. Hobbs, Radiation effects in analysis of inorganic specimens by TEM. In Introduction to analytical electron microscopy (Ed. J. J. Hren, J. I. Goldstein, and D. C. Joy, Plenum, New York, 1979).
25. Abid, Y. *J. Phys.: Condens. Matter* **1994**, 6, 6447-6454.
26. Tanaka, K.; Takahashi, T.; Kondo, T.; Umeda, K.; Ema, K.; Umebayashi, T.; Asai, K.; Uchida, K.; Miura, N. *Jpn. J. Appl. Phys*. 2005, 44, 5923-5932.
27. S. Sourisseau, N. Louvain, W. Bi, N. Mercier, D. Rondeau, F. Boucher, J.-Y. Buzaré, C. Legein, *Chem. Mater*. **2007**, 19, 600-607.
28. Filip, M. R.; Eperon, G. E.; Snaith, H. J.; Giustino, F. *Nature Commun*. **2015**, 5, 5757.
29. Dohner, E. R.; Jaffe, A.; Bradshaw, L. R.; Karunadasa, H. I. *J. Am. Chem. Soc*. 2014, **136**, 13154-13157.
30. Gargas, D. J.; Gao, H.; Wang, H.; Yang, P. *Nano Lett*. 2011, **11**, 3792-3796.
31. Wu, X.; Trinh, M. T.; Niesner, D.; Zhu, H.; Norman, Z.; Owen, J. S.; Yaffe, O.; Kudisch, B. J.; Zhu, X.-Y. *J. Am. Chem. Soc*. 2015, **137**, 2089-2096.
32. Novoselov, K. S.; Geim, A. K.; Morozov, S. V.; Jiang, D.; Zhang, Y.; Dubonos, S. V.; Grigorieva, I. V.; Firsov, A. A. *Science* **2004**, 306, 666-669.
33. Mak, K. F.; Lee, C.; Hone, J.; Shan, J.; Heinz, T. F. *Phys. Rev. Lett*. **2010**, 105, 136805.
34. O'Keefe, M. A.; Kilaas, R. *Scanning Microsc. Suppl*. **1988**, 2, 225.
35. Momma, K.; Izumi., F. *J. Appl. Crystallogr*. **2011**, 44, 1272.

Chapter 5

Synthesis and Properties of $CsSnI_3$ Nanowires

5.1 Abstract:

The synthesis of the lead-free halide perovskite is an interesting new area for the development of new high performance, solution processable semiconductors that are less toxic than existing materials. This work introduces the first synthesis of perovskite $CsSnI_3$ nanowires. Electrical conductivity as well as Seebeck coefficient measurements demonstrate that black, orthorhombic phase $CsSnI_3$ nanowires are highly conductive p-type semiconductors with a hole mobility of 394 $cm^2\ V^{-1}\ S^{-1}$ while temperature-dependent electrical conductivity measurements show metallic behavior. Our results show that $CsSnI_3$ possesses a rare combination of high electrical conductivity and ultralow thermal conductivity, which is sought after for unique thermal barrier coatings and thermoelectric devices. Lattice thermal conductivities of solution-synthesized, single-crystal inorganic perovskite $CsSnI_3$ nanowires are measured to be 0.38 ± 0.04 W $m^{-1}\ K^{-1}$ at room temperature, which is only a factor of two larger than the calculated minimum thermal conductivity for this material. *Ab-initio* analysis reveals that these $CsSnI_3$ nanowires possess intrinsically small group velocities and extremely short phonon mean free paths down to a few nanometers, and strong optical-acoustic phonon scattering that results from a rattling mechanism.

5.2 Introduction:

Halide perovskite materials have attracted significant attention for their unique material properties. This family of materials spans the organic-inorganic hybrid perovskites such as $CH_3NH_3BX_3$ and $HC(NH_2)_2BX_3$ as well as the all-inorganic halide perovskites, which include $CsBX_3$ (where B = Pb, Sn and X = Cl, Br, I). Together, both of these halide perovskites have been investigated for potential applications in solution-processed optoelectronic devices such as photovoltaics,[1,2] light emitting diodes,[3,4] and lasers.[5,6] The study of the fundamental properties of $CsSnI_3$ is also of interest as this material is lead-free and possesses a direct band gap in the near IR at 1.3 eV. In contrast to other materials with direct band gaps in a similar range like GaAs, CdTe, and InP, there are no highly toxic reagents necessary to synthesize this material. This makes the development of this material interesting for application as an optoelectronic device.

The reliability and performance of optoelectronic devices is critically dependent on operating temperature, and it is essential to understand the thermal transport properties of the halide perovskites at the nanoscale especially given the relevance of thermal loads and the drive towards miniaturization of semiconductor devices.[7,8] Furthermore, perovskite nanowires (NWs) can be utilized as a platform to create hybrid composites. Hybrid composites can further optimize transport properties via interfacial engineering and enable flexible and scalable inexpensive devices.[9] However, there have been very limited experimental investigations on the thermal conductivity of halide perovskites,[10] and to our knowledge, there has been no experimental investigation of the thermal transport properties of all-inorganic perovskites. It is very likely that there is also a mechanistic difference between the thermal transport properties of the all inorganic perovskites and the hybrid perovskites because of the differing behavior of polyatomic organic cation versus the monoatomic Cs^+ cation.[11] Understanding the thermal transport in the all-inorganic perovskites is important as it has been proposed that all-inorganic perovskites may have advantages in thermal stability over hybrid perovskites.[12]

The ability to efficiently manage the flow of thermal energy is crucial to numerous applications such as microelectronics and energy conversion devices. Materials with low thermal conductivity are sought for turbine engines, thermal data storage devices, and thermoelectric energy conversion devices,[13-15] and materials with high thermal conductivity are required to dissipate heat efficiently from microelectronic devices.[16] While electrically insulating amorphous solids generally possess the lowest thermal conductivities,[17] single crystals with ultralow thermal conductivity are rare due to their well-ordered atomic structure, and these rare crystals often involve complicated compositions and expensive synthetic processes.[18] To achieve low thermal conductivity, complex systems have been designed with large numbers of atoms in the primitive unit cell along with cage-like crystal structures that exhibit atomic rattling motions (e.g. skutterudites and clathrates).[19,20] Other approaches use disordered layer and superlattice structures. For example, thermal conductivity in disordered layered crystals of WSe_2 was found to be lower than the amorphous limit in the cross-plane direction,[21] and thermal conductivity of epitaxial oxide superlattices was reduced below the alloy limit by the phonon interference effect.[22] However, finding materials with low thermal conductivity in a simple, fully dense, and single crystalline solid with a simple synthetic process has been extremely challenging.

Here, we report ultralow thermal conductivity of solution-synthesized $CsSnI_3$ all-inorganic perovskite NWs. Based on our *ab-initio* simulations, the ultralow thermal conductivity is attributed to low group velocity, significant anharmonicity, and strong collective rattling at the atomic level. Our measurement indicates that $CsSnI_3$ has a rare combination of ultralow thermal conductivity, a high electrical conductivity value of 282 S/cm, and a high hole mobility of 394 $cm^2\ V^{-1}\ S^{-1}$.

5.3 Synthesis of $CsSnI_3$ Nanowires:

In this report, we have developed the first synthesis of black phase $CsSnI_3$ NWs by a low temperature solution-phase process, which has been a challenge because of the sensitivity of $CsSnI_3$ to moisture and oxidation.[23,24] The black phase of $CsSnI_3$ has a direct band gap at 1.3 eV, which makes this material a good IR emitter and light absorber without the presence of toxic lead or cadmium or the use of highly reactive metal-organic chemical vapor deposition precursors. As a result, this material is of interest for the development of optoelectronic devices. A scheme for the synthesis and images of as synthesized $CsSnI_3$ nanowires are shown in Fig. 5-1 and Fig. 5-2 a,b. During the reaction, nanoplates and nanocubes may form in addition to nanowires. As discussed below, in this work, the yield of $CsSnI_3$ nanowires was optimized, and individual nanowires were isolated using a micromanipulator.

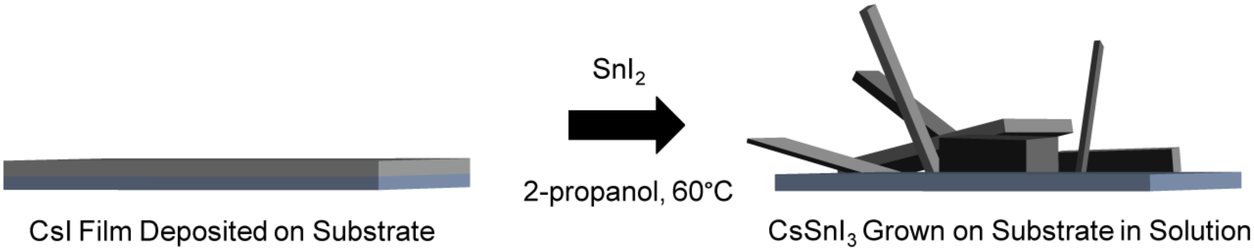

Figure 5-1. Schematic of $CsSnI_3$ solution phase synthesis in anhydrous 2-propanol.

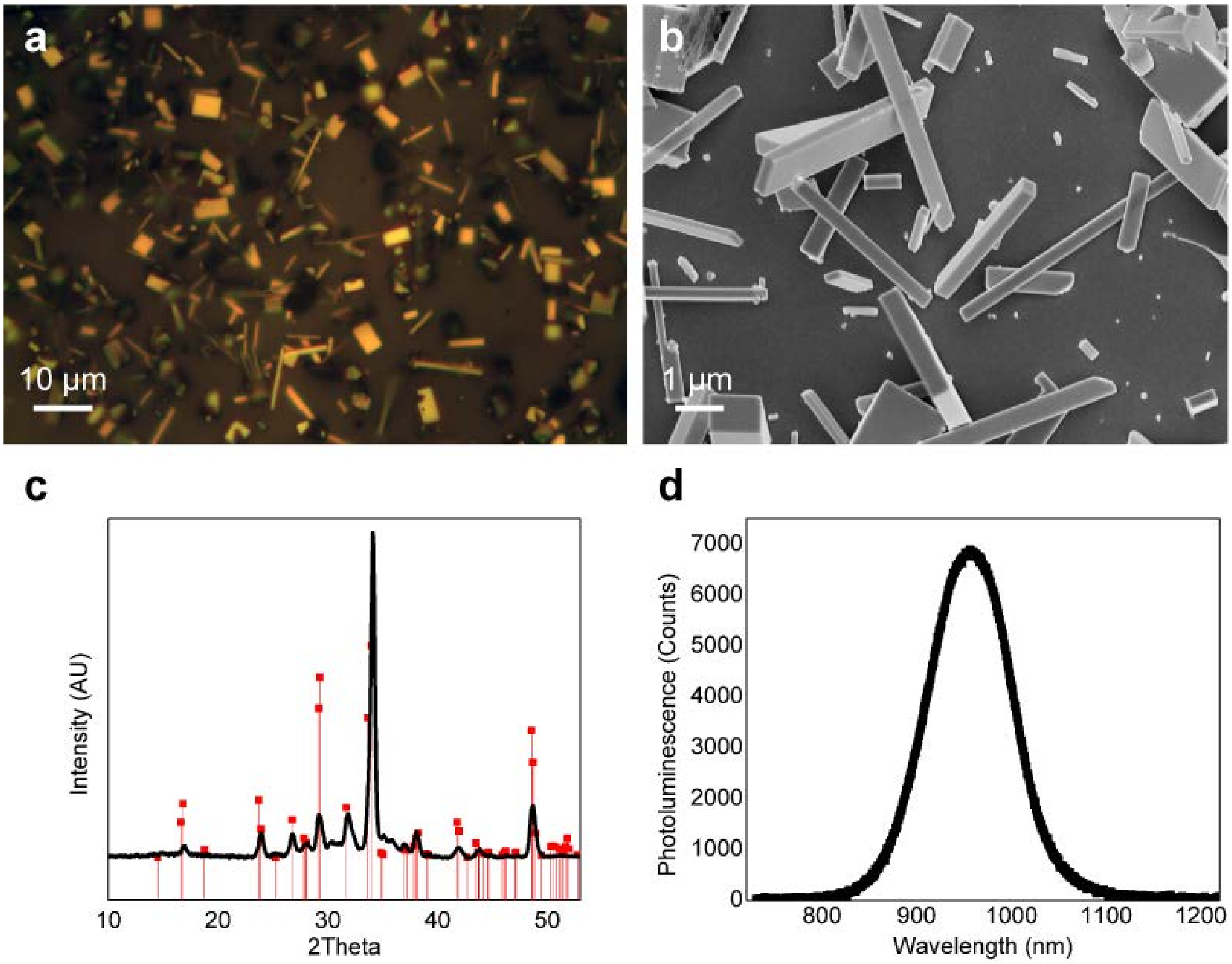

Figure 5-2. Characterization of solution phase synthesized $CsSnI_3$ nanowires. (a) Optical microscopy image of as-synthesized $CsSnI_3$ nanowires grown on a Si substrate. (b) SEM image of as-synthesized $CsSnI_3$ nanowires. (c) Powder X-ray diffraction of $CsSnI_3$ sample. The red drop down lines show the fitting to the standard pattern for the room temperature black orthorhombic phase of $CsSnI_3$ with ICSD number: 69996. (d) Single nanowire photoluminescence from a $CsSnI_3$

nanowire showing strong photoluminescence around 1.3 eV, which is indicative of the black phase $CsSnI_3$.

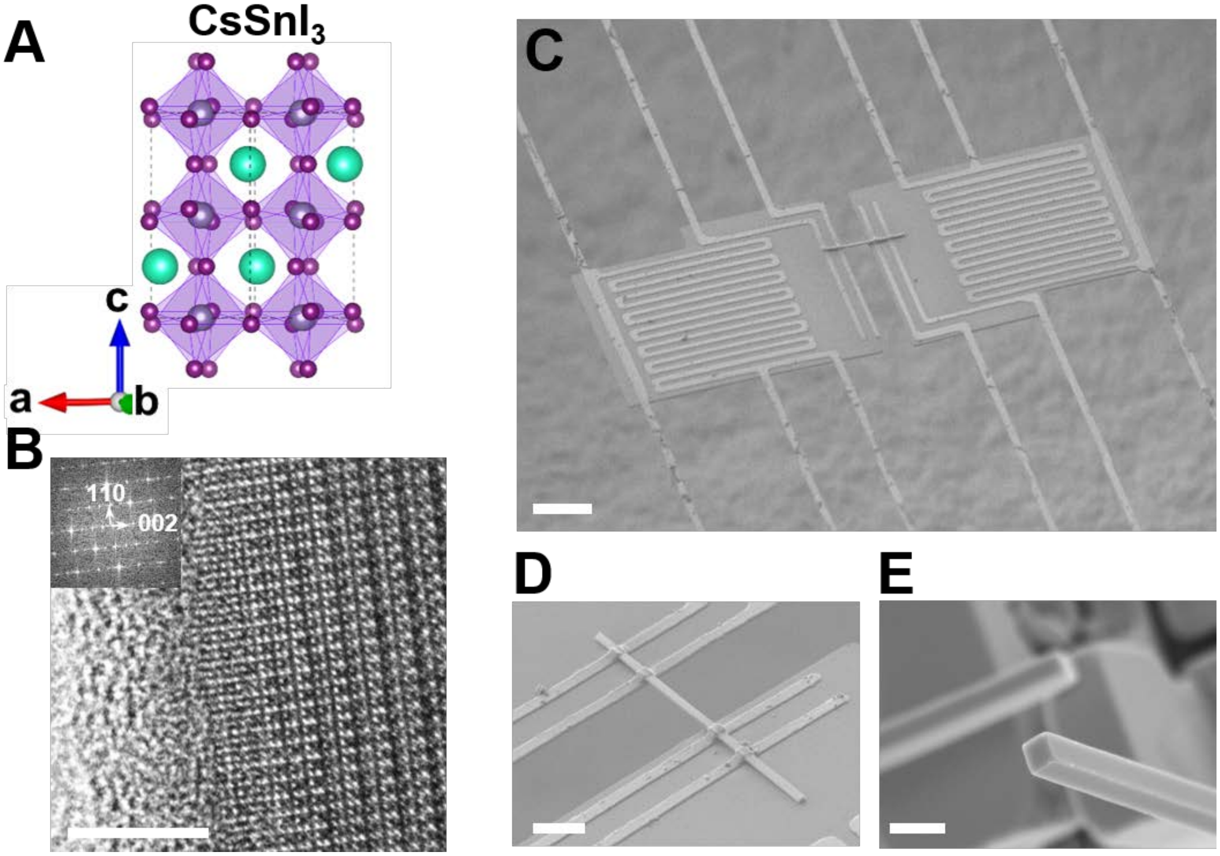

Figure 5-3. Inorganic perovskite $CsSnI_3$ nanowires and all-in-one suspended devices to measure their thermal and electrical properties. (A) Crystal structure of $CsSnI_3$. Atoms are colored by Cs: green, I: purple, Sn: light purple. (B) High resolution transmission electron microscope (HRTEM) image and corresponding Fast Fourier transform (FFT) pattern of $CsSnI_3$ demonstrate its single crystalline nature. (C to E) SEM images of all-in-one suspended devices. Individual perovskite nanowires are suspended between two membranes. (E) SEM image of the individual perovskite nanowire. Scale bars in (B), 5 nm: in (C), 10 µm: in (D) 3 µm: in (E) 1 µm.

Overall, it has proven non-trivial to synthesize the black phase of $CsSnI_3$ in solution with the product typically being the yellow $CsSnI_3$ polymorph, which consists of double chains of $[Sn_2I_6^{2-}]$. Recently, it has been demonstrated that it is possible to synthesize $CsSnI_3$ nanocubes in the presence of a trioctylphosphine reducing agent in colloidal solution.[25] In our synthesis of $CsSnI_3$ nanowires, it is interesting to note that in a well-maintained glove box atmosphere with high purity reagents, a reducing agent is not necessary to obtain the black orthorhombic phase of $CsSnI_3$. Following previous reports, reagent purity is important in our reaction for synthesizing $CsSnI_3$ nanostructures.[26]

5.4 Structural and Optical Characterization of $CsSnI_3$ Nanowires:

We confirm the assignment of the nanowires to the black orthorhombic phase of $CsSnI_3$ by X-ray powder diffraction (XRD) and single-nanowire photoluminescence, which shows an optical bandgap of 1.3 eV (Fig. 5-2, C, D). Low-dose high-resolution transmission electron microscopy, Fourier transforms of the lattice images, and selected area electron diffraction data for $CsSnI_3$ NWs confirm that these NWs are single crystalline, and that the crystal growth direction is [110] (Fig. 5-3B, 5-4). Specifically, the bulk film and the single nanowires can be indexed to the orthorhombic phase of $CsSnI_3$ (ICSD Number: 69996) by powder X-ray diffraction and selected area electron diffraction, respectively (Fig. 5-2C, 5-4). A SEM image of the $CsSnI_3$ nanowires shows that the nanowires are faceted with a typical rectangular cross section (Fig. 5-2B, 5-3E).

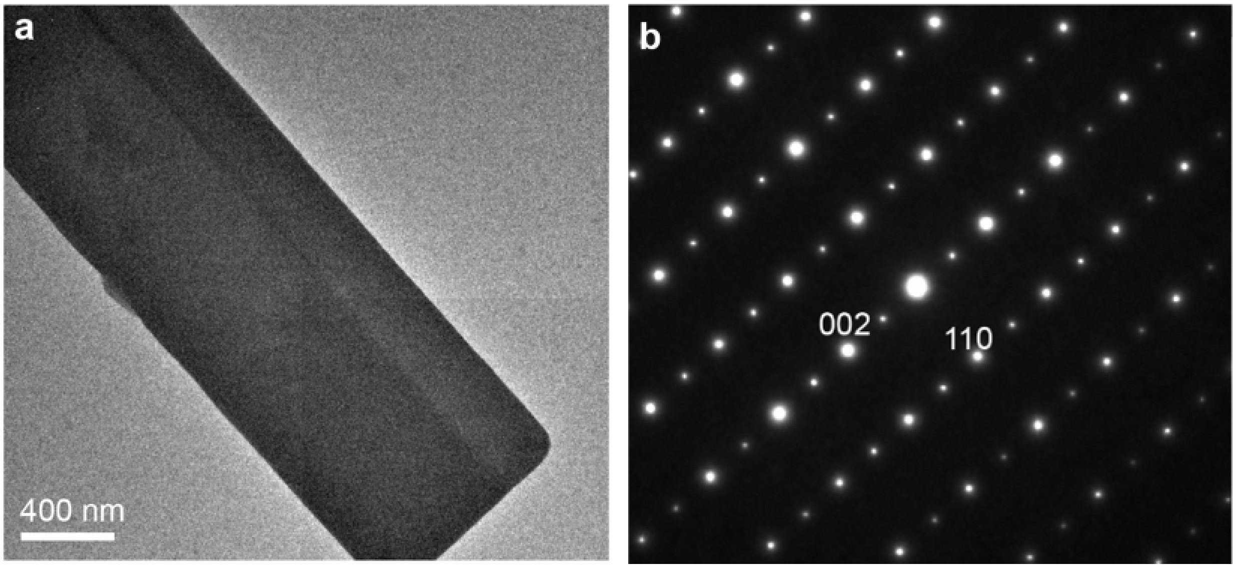

Figure 5-4. TEM and corresponding SAED of $CsSnI_3$ perovskite nanowires. (a) TEM image of a $CsSnI_3$ nanowire. (b) Corresponding SAED image of the $CsSnI_3$ nanowire.

In addition, a representative photoluminescence spectrum from a single $CsSnI_3$ nanowire is shown in Fig. 5-2D. Single nanowires of $CsSnI_3$ show strong photoluminescence centered around 950 nm, which matches reports for the room temperature black orthorhombic phase of $CsSnI_3$.[23] Furthermore, since the single nanowires only display IR light emission centered around 950 nm without any visible light emission, this also confirms that the individual nanowires are in the black phase of $CsSnI_3$ as opposed to the yellow double chain phase of $CsSnI_3$, which will exhibit photoluminescence in the visible range.

For this reaction, a film of CsI and a solution of SnI_2 in 2-propanol serve as the precursors for the reaction to grow nanostructures on the substrate that is submerged in the anhydrous 2-propanol solution. Previous reports for the synthesis of $CH_3NH_3PbX_3$ (X=Cl, Br, I) mixed nanowires, nanosheets, and nanocubes demonstrate the reaction of a lead acetate or lead iodide film on a substrate with a solution of CH_3NH_3X in 2-propanol.[27,28] For these reactions, the Pb precursor is deposited on the substrate, and the Pb^{2+} cation occupies the B site in the ABX_3 perovskite structure. Interestingly, for the growth of $CsSnI_3$, the precursor for the A site cation, which is CsI, should be loaded onto the substrate first to produce well-faceted black phase $CsSnI_3$

nanowires. Another difference is that although the reaction to grow $CH_3NH_3PbX_3$ nanowires can be performed in air, the reaction to synthesize $CsSnI_3$ requires air-free conditions, which requires a N_2 or Ar glove box. The reactions to grow $CH_3NH_3PbX_3$ nanowires are believed to occur via both a liquid-solid interfacial reaction and a dissolution-recrystallization mechanism, which yields the growth of faceted nanostructures via the existence of a low and controllable supersaturation of precursors from the continued dissolution of the underlying film. We believe that $CsSnI_3$ may crystalize via a similar mechanism. As shown in Fig. 5-5, when the concentration of SnI_2 is too high, the products are a mixture of many large and small cuboids with very few high aspect ratio products. Furthermore, when the concentration is too low, the majority of the products are relatively large with relatively low aspect ratio. This trend suggests that at high concentrations there is too much rapid nucleation and growth of $CsSnI_3$ particles, and at low concentrations, fewer $CsSnI_3$ particles nucleate, but these particles will eventually grow to a relatively large size with poor control over the aspect ratio. Overall, intermediate concentrations of SnI_2 in 2-propanol are best for the synthesis of $CsSnI_3$ nanowires.

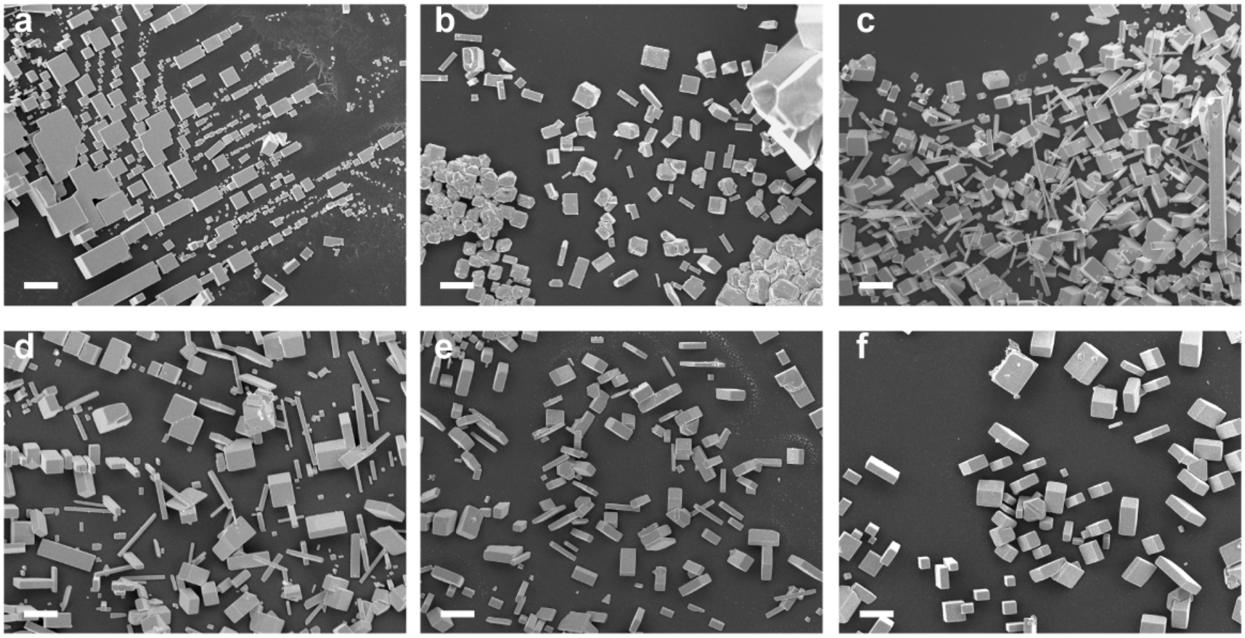

Figure 5-5. Effect of SnI_2 concentration on morphology of $CsSnI_3$. (a) 6.6 mmol/L SnI_2. (b) 3.3 mmol/L SnI_2. (c) 1.7 mmol/L SnI_2. (d) 1.1 mmol/L SnI_2. (e) 0.83 mmol/L SnI_2. (f) 0.66 mmol/L SnI_2. For all substrates, the reaction time was 120 minutes. All scale bars are 5 µm.

5.5 Characterization of the Thermal Conductivity of $CsSnI_3$ Nanowires:

In order to measure thermal conductivity of the all-inorganic perovskite $CsSnI_3$ nanowires, we employed all-in-one suspended micro-island devices that are capable of measuring the thermal conductivity, electrical conductivity, and Seebeck coefficient of the same single NW (Fig. 5-3, C-E).[29,30] Suspended devices allow us to investigate these transport properties along the length of the NW. We first validated our measurement platform by measuring the thermal conductivity of amorphous SiO_2 NWs (Fig. 5-6). Furthermore, we estimated the thermal contact resistance between the NWs and Pt electrodes to obtain an accurate value for the intrinsic thermal conductivity (Fig. 5-7).[31,32] The contribution of thermal contact resistances is only found to be ~3% of the intrinsic thermal resistance of the perovskite NWs.

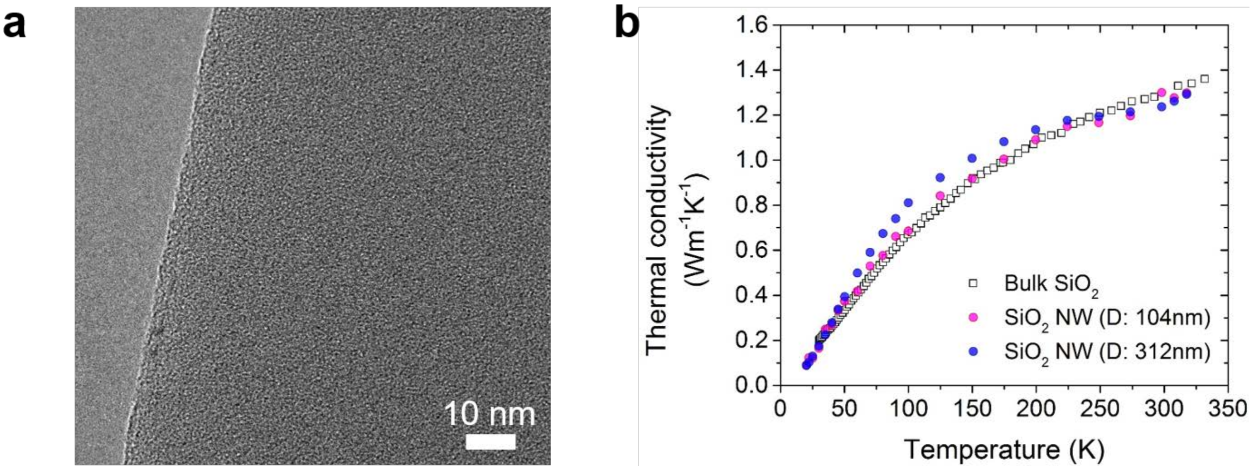

Figure 5-6. Validation of thermal conductivity experiment: control experiment with amorphous SiO_2 (a-SiO_2) nanowires and comparison between measured thermal conductance and estimated noise equivalent conductance (NEG) (a) a-SiO_2 NW is confirmed by HRTEM. (b) Thermal conductivity of a-SiO_2 NWs with diameters 104 and 312 nm agrees very well with bulk a-SiO_2, proving that our experimental setups are firmly valid.

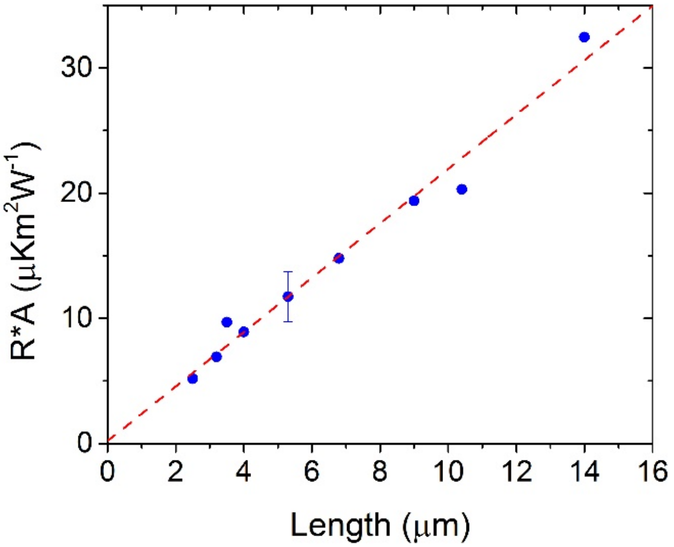

Figure 5-7. Characterization of thermal contact resistances of two interfaces between $CsSnI_3$ nanowire and Pt electrode. Measured total thermal resistances multiplied by cross-section area of nanowires are plotted against length of nanowires. From y-intercept 0.21×10^{-6} $K\cdot m^2\cdot W^{-1}$, we estimate the thermal contact resistance to range from 0.5×10^6 to 3×10^6 K/W, and the contribution

of thermal contact resistance is only up to ~3% of the intrinsic thermal resistance of the perovskite NWs.

The measured thermal conductivity for a representative NW is presented in Fig. 5-8. The characteristic diameter of the NWs, which can be represented in terms of the Casimir length ($\sqrt{4wh/\pi}$, where w is the width and h is the height), is 400 nm.[33] These $CsSnI_3$ inorganic perovskite NWs exhibit crystal-like thermal conductivity in which the thermal conductivity initially increases and then decreases as temperature rises, despite having ultralow lattice thermal conductivity values: $CsSnI_3$ 0.38 ± 0.04 $Wm^{-1}K^{-1}$ at room temperature. The black phase $CsSnI_3$ has a high electrical conductivity as elaborated upon below, so electrons significantly contribute to the thermal conductivity. Using the Wiedemann-Franz law, the electron ($k_{electron}$) and lattice ($k_{lattice}$) thermal conductivity can be readily obtained from the measured total thermal conductivity (k_{total}). In order to compare the lattice thermal conductivity of the $CsSnI_3$ NWs with the minimum thermal conductivity of that composition, we estimated the amorphous limit of the lattice thermal conductivity (k_{min}) based on the hopping heat conduction model developed by Cahill et al. (Fig. 5-8).[17] As can be clearly seen, the lattice thermal conductivity is close to the minimum amorphous-limit thermal conductivity near room temperature, despite the fact that the NWs are single-crystalline. We measured the thermal conductivity of several single NWs, and the results are consistent across each of our single nanowire devices (Fig. 5-9).

It is interesting to consider how the thermal conductivity of $CsSnI_3$ compares with other crystalline materials with low thermal conductivity (Fig. 5-8B). Remarkably, the measured thermal conductivity values of solution-synthesized inorganic perovskite NWs are comparable to and even smaller than various crystal structures such as Zintl compounds, clathrates, and skutterudites.[15] The inset of Fig. 5-8B shows the ratio of $k_{lattice}$ to k_{min} for inorganic perovskite NWs at room temperature, which is only about 2. This ratio is uncommonly low given the fact that Bi_2Te_3 ($k_{lattice}$ = 1.6 $Wm^{-1}K^{-1}$) has the ratio[34] of 6 and filled skutterudite $CeFe_4Sb_{12}$ ($k_{lattice}$ = 1.9 $Wm^{-1}K^{-1}$) has the ratio of 3.5.[34] It is also worthwhile to make direct comparisons with other crystals of ultralow thermal conductivity. The ratio of $k_{lattice}$ to k_{min} for clathrate $Ba_8Ga_{16}Ge_{30}$ ($k_{lattice}$ = 1.1 $Wm^{-1}K^{-1}$)[36] and Zintl $Yb_{14}AlSn_{11}$ ($k_{lattice}$ = 0.6 $Wm^{-1}K^{-1}$)[37] is 2, which is comparable but still higher than the ratio for $CsSnI_3$.

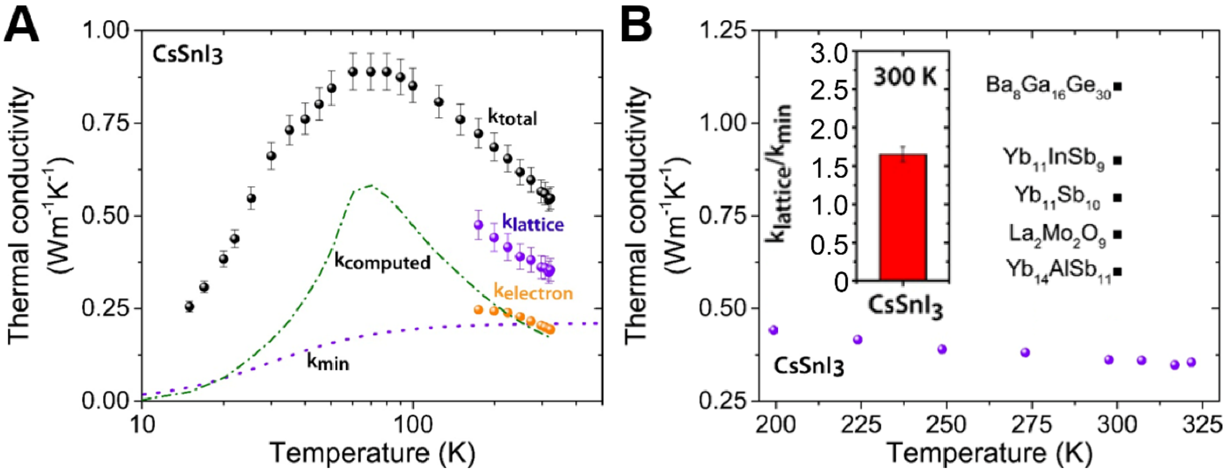

Figure 5-8. Thermal conductivity of $CsSnI_3$ inorganic perovskite nanowires. (A) Measured thermal conductivity (k_{total}), *ab-initio* calculated thermal conductivity ($k_{computed}$), and estimated minimum thermal conductivity (k_{min}). Thermal conductivity contribution by electrons ($k_{electron}$) for $CsSnI_3$ is estimated from measured electrical conductivity and the Wiedemann-Franz law, and lattice thermal conductivity ($k_{lattice}$) is obtained by subtracting electron thermal conductivity ($k_{electron}$) from total thermal conductivity (k_{total}). (B) Comparison between $CsSnI_3$ and other crystals with very low thermal conductivity ($Ba_8Ga_{16}Ge_{30}$,[36] $Yb_{11}InSb_9$,[46] $Yb_{11}Sb_{10}$,[47] $La_2Mo_2O_9$,[48] $Yb_{14}AlSb_{11}$).[37] Inset shows the ratio of lattice thermal conductivity to the minimum thermal conductivity.

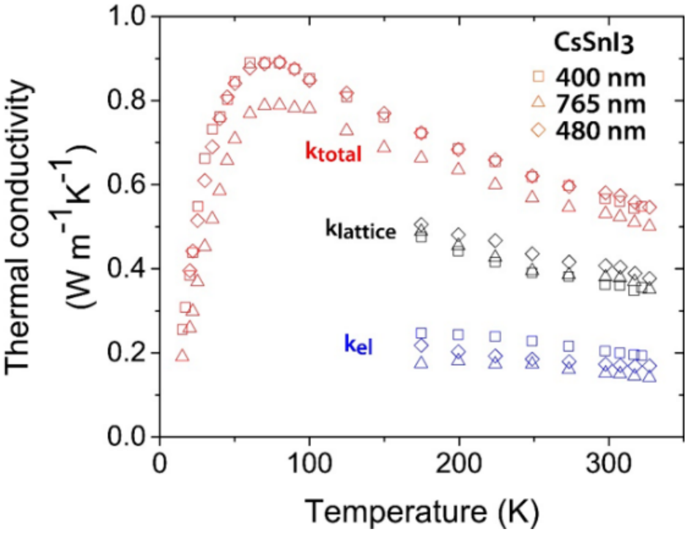

Figure 5-9. Thermal conductivity results of $CsSnI_3$ are consistent between several individual nanowires of different diameters.

5.6 Potential Origin of Ultralow Thermal Conductivity of $CsSnI_3$ Nanowires:

While dynamic disorder associated with rotational degrees of freedom in organic components is considered to be the main reason for the low thermal conductivity in hybrid perovskite materials,[10] such a scenario cannot be applied to inorganic perovskite crystals. In order to elucidate the fundamental mechanisms responsible for the observed ultralow thermal conductivity in our crystalline $CsSnI_3$ NWs, we applied a combination of *ab-initio* simulations and Boltzmann transport theory (details in supplementary text).[38] With the defect density serving as a fitting parameter, the crystal-like temperature dependence was reproduced, and the calculated thermal conductivity is in reasonable agreement with experiments (Fig. 5-8A). This agreement suggests that two- and three-phonon processes govern the phonon transport in perovskite NWs, and the discrepancy between the calculated and experimental values at high temperature may arise from collective phonon excitations. For the $CsSnI_3$ crystal, the defect density calculated from fitting to the experimental thermal conductivity is consistent with that calculated by fitting to the electrical transport measurements (Fig. 5-16), which supports the interpretation that Sn vacancies are the dominant intrinsic defect determining the carrier concentration and transport properties as indicated by previous studies.[23]

Our simulations suggest that the extremely low $k_{lattice}$ values can be attributed to low group velocities (v_g) and the short phonon mean free paths (l). The calculated v_g is quite small, as expected given the large atomic masses in $CsSnI_3$ (Fig. 5-11). On the other hand, l is significantly suppressed either by scattering of intrinsic defects and boundaries at low temperature, or by strong phonon-phonon scattering at high temperature (Fig. 5-10A, 5-12). Once a sufficient density of phonons is populated by thermal energy, strong interactions between optical and acoustic modes will be stimulated as a result of the large number of band-crossings in the low-frequency range (Fig. 5-10A, inset). The calculated $k_{lattice}$ exhibits substantial anisotropy, which is probably due to the lower density of phonon modes along the [001] direction. It is worth noting that the maximum l at 300 K in the γ phase of $CsSnI_3$ is already comparable to its lattice parameters. Nevertheless, unlike the mechanism of thermal energy exchange between neighboring atoms vibrating with random phases in amorphous materials,[39] the coherent nature of lattice vibration is preserved in our $CsSnI_3$ crystals.

Since the low v_g is not uncommon among thermoelectric materials, the exceptionally low $k_{lattice}$ should mainly be attributed to the tremendous anharmonicity that leads to the maximum l (γ-$CsSnI_3$: 5 nm) being much shorter than those of traditional inorganic crystals (PbTe: 200 nm,[40] Si: 30,000 nm);[38] instead it is comparable to those of Ge clathrates with guest atoms (1-6 nm)[41-42] and Zn_4Sb_3 (1 nm)[43]. The rattling mechanism associated with local soft modes is widely accepted to be responsible for the low $k_{lattice}$ in clathrates,[41-42] and it has also been used to understand thermal transport in Zn_4Sb_3 where Sb_2 dumbbells are considered to be rattling units,[43] although structural disorder may also play an important role.[44] From the cage structure of the γ phase, it is intuitive to investigate the rattling mechanism as the main source of anharmonicity. However, it is not clear why such an effect would be especially significant in our system. To answer this question, we correlate the rattling strength with structural inhomogeneity via an analysis of bond length distributions. In the case of γ-$CsSnI_3$ (Fig. 5-10B), the distances from a Cs rattler to the surrounding I atoms are quite different as enforced by the orthorhombic symmetry of the cages, which generates soft optical modes for interacting with acoustic phonons, and this is evident in the projected DOS on Cs atoms.

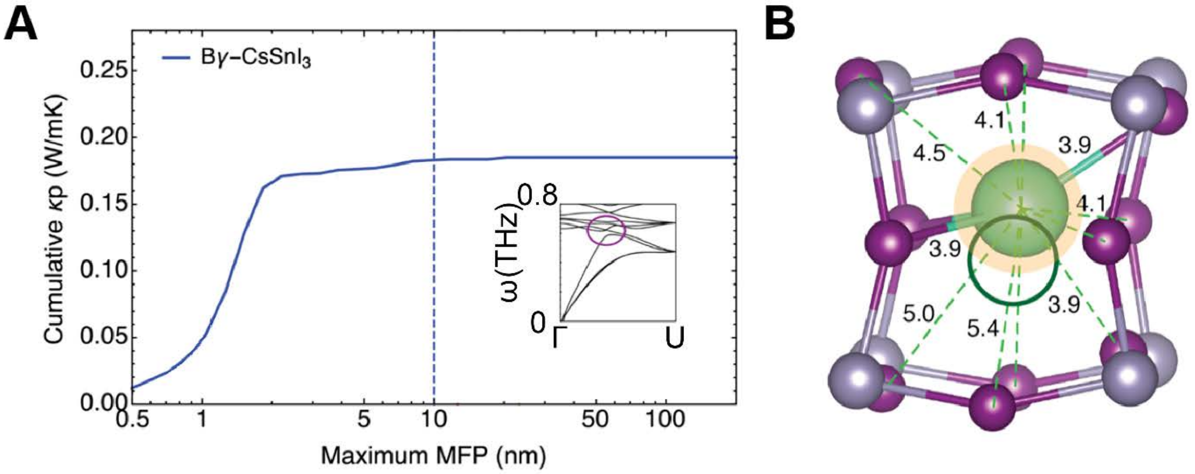

Figure 5-10. Theoretical analysis of $CsSnI_3$ lattice thermal conductivity ($k_{lattice}$) based on the cluster rattling model. (A) Cumulative $k_{lattice}$ with respect to mean free path (l) at room temperature computed by a combination of the Boltzmann transport equation and DFT, with a dashed line corresponding to the defect concentration fitted to the experimental data shown in Fig. 5-8. The inset presents the phonon dispersion curve of $CsSnI_3$ calculated by DFT, with the band-crossing between optical and acoustic modes highlighted by the purple circle. Inhomogeneous bonding structures associated with (B) the atomic rattling mechanism in $CsSnI_3$. The Cs-I bonds with length < 3.90 angstroms are shown as sticks, while the others are denoted by dashed lines. The rattling unit is highlighted by an orange shaded region.

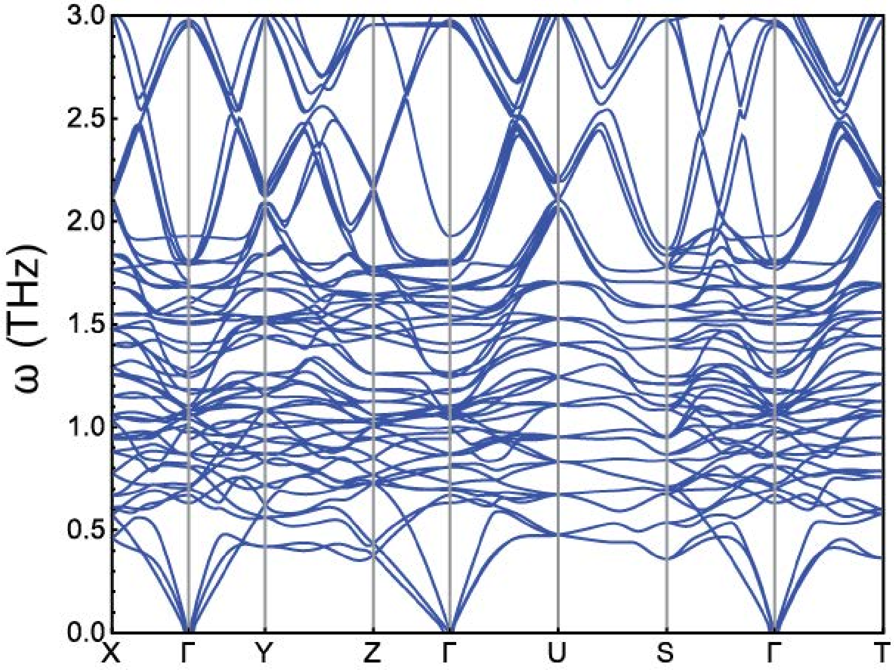

Figure 5-11. Calculated phonon dispersion relation of bulk $CsSnI_3$ crystals.

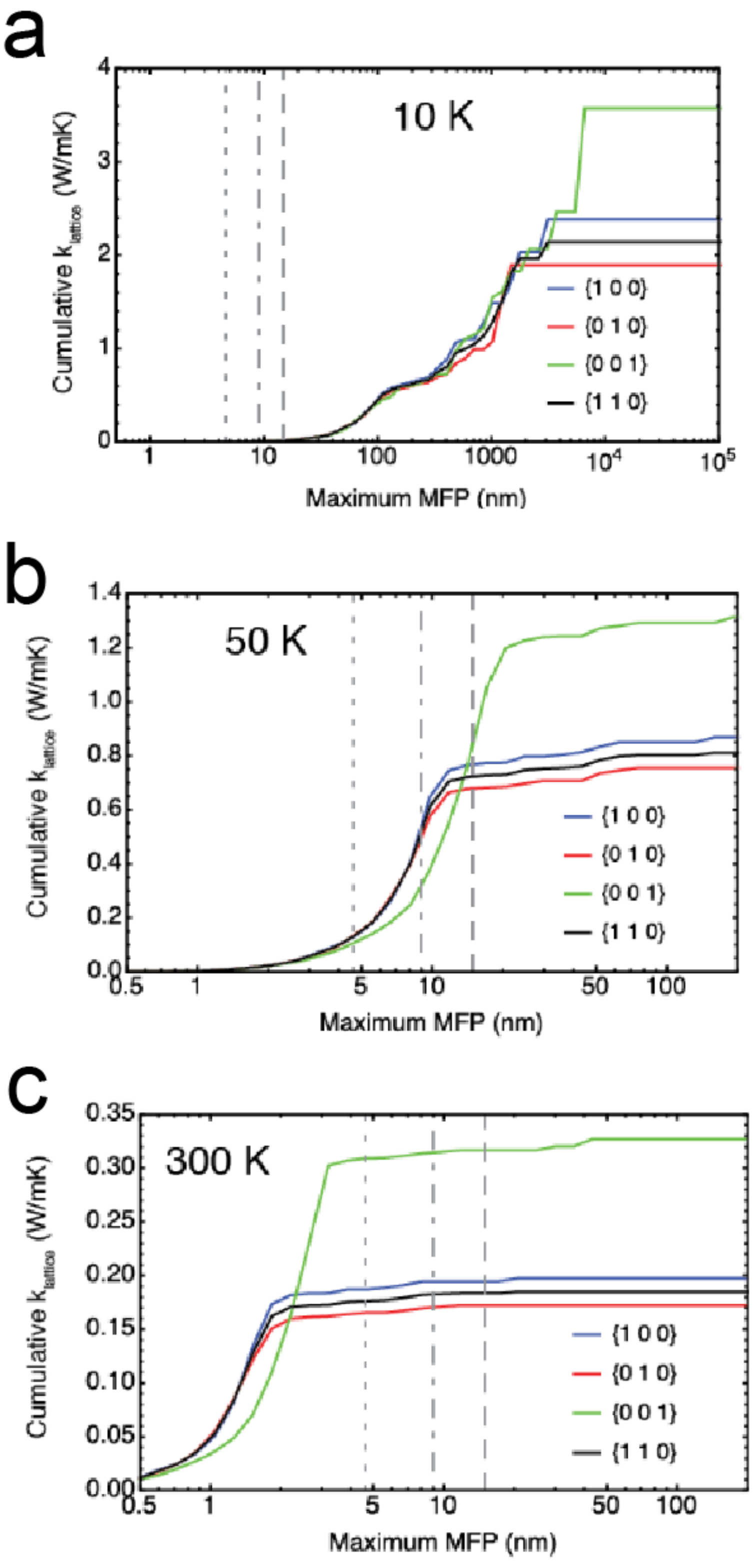

Figure 5-12. Computed cumulative *$k_{lattice}$* with respect to phonon mean free path in various directions of $CsSnI_3$ crystals, at temperatures of 10 K (a), 50 K (b), and 300 K (c). The dotted,

dashed-dotted and dashed lines illustrate the values based on concentrations of Sn vacancies of 1×10^{19}, 1×10^{18}, and 3×10^{17} cm^{-3}, respectively. The cumulative $k_{lattice}$ includes the contributions from the phonons with $\mathbf{\Lambda}_\lambda$ up to the maximum MFP.

5.7 Charge Transport Properties of $CsSnI_3$ Nanowires

Next, we measure the charge transport properties for the black $CsSnI_3$ NWs. Fig. 5-13 shows the four-probe electrical conductivity (σ) and Seebeck coefficient (S) of a single black phase $CsSnI_3$ NW. At room temperature, σ is 282 S/cm, and S is 79 µV/K. σ decreases as the temperature increases, exhibiting metallic behavior, and the positive S indicates a hole dominant (*p*-type) semiconductor. The transport properties of other single $CsSnI_3$ NWs are consistent (Fig. 5-9, 5-14). The observed temperature dependent σ and S are in agreement with previous work on black single-crystalline bulk $CsSnI_3$.[23] Black phase $CsSnI_3$ NWs have a relatively high electrically conductivity, yet ultralow thermal conductivity (k_{total} = 0.57 $Wm^{-1}K^{-1}$). SnSe crystals that were recently studied exhibit a similar thermal conductivity, but electrical conductivity is at least one order smaller than that of black phase $CsSnI_3$.[45] In order to estimate the hole mobility (μ), the electronic relaxation time was extracted by fitting the calculated σ to experimental data, and then the relation $\sigma=ne\mu$ in the low concentration limit indicates a high hole mobility value at room temperature of 394 cm^2 V^{-1} s^{-1}. In a first among the halide perovskites, we also report the power factor and calculated ZT of black phase $CsSnI_3$, 186 µW m^{-1} K^{-2} and 0.11 at 320 K, respectively (Fig. 5-14b).

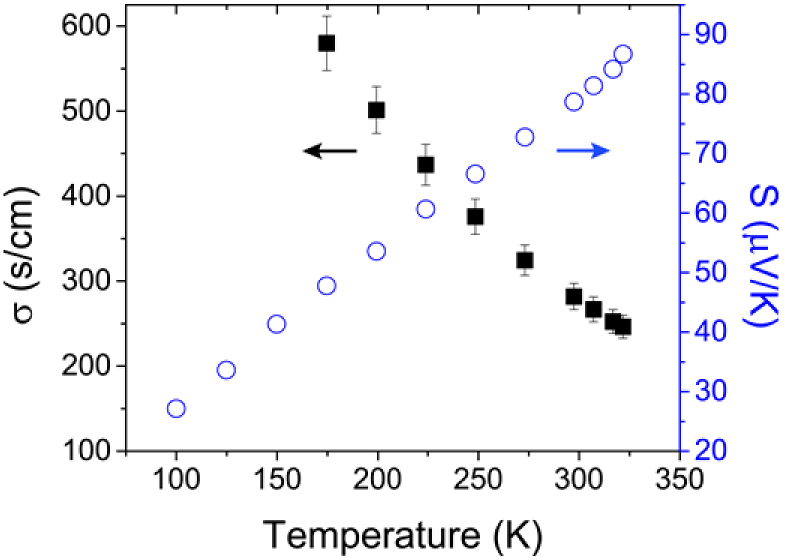

Figure 5-13. Electrical conductivity (blue circles) and Seebeck coefficient (black squares) of a single $CsSnI_3$ NW.

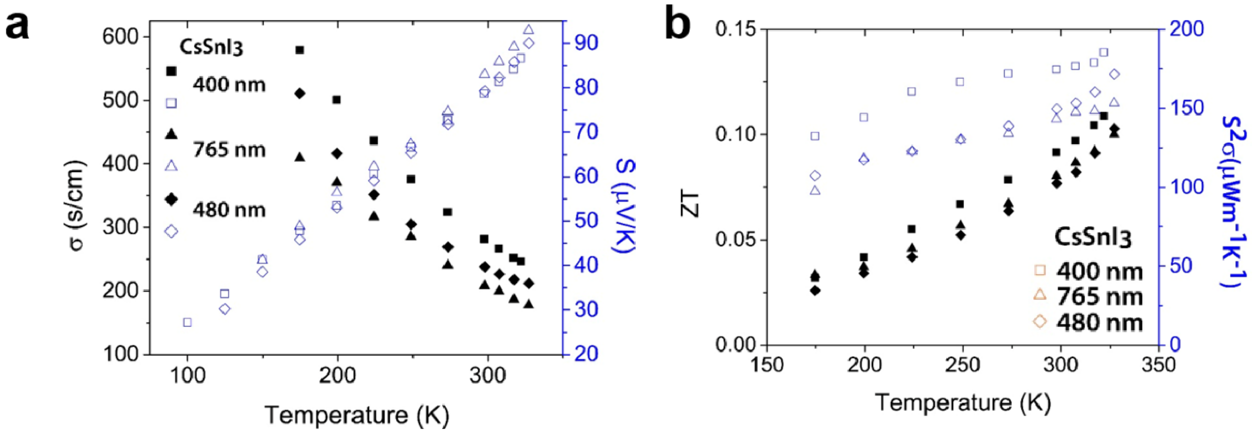

Figure 5-14. (a) Four-probe electrical conductivity (black) and Seebeck coefficient (blue) of single CsSnI$_3$ nanowires. (b) Calculated figure-of-merit (ZT) in black and power factor ($S^2\sigma$) in blue for single CsSnI$_3$ nanowires.

The superior electrical conductivity in CsSnI$_3$ compared to the other insulating halide perovskite nanowires can be understood by their different electronic structures and doping densities. According to our simulations, CsSnI$_3$ is a semiconductor that exhibits substantial dispersion (Fig. 5-15). The low effective mass, though, will not lead to high σ unless the carrier concentration is sufficiently large. This raises a dilemma for halide perovskites without an explicit dopant: a low density of intrinsic defects will not provide enough free carriers, while a high defect density is likely to generate trap states that serve as fast recombination centers. An advantage of CsSnI$_3$ revealed by our calculations is that the dominant intrinsic defect type (V$_{Sn}$) can lower the Fermi level efficiently, but it affects the band structure only slightly and preserves wavefunction delocalization even at very high carrier concentration. This scenario is consistent with the measured p-type transport behavior, as well as the small deviation from the Wiedemann–Franz law that implies a high DOS around the Fermi level (Fig. 5-16).

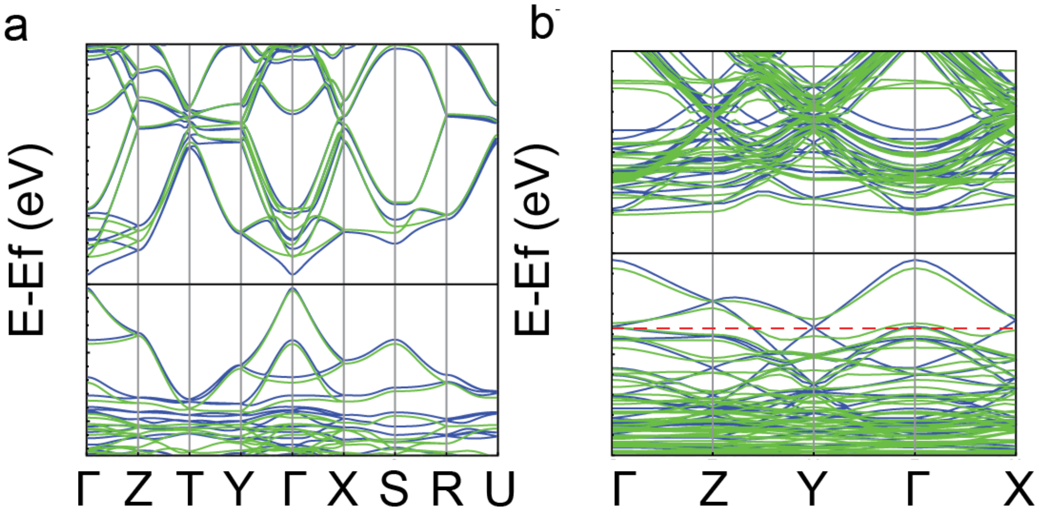

Figure 5-15. Calculated band structures of pristine $CsSnI_3$ crystals. The blue and green lines in panel (a) are results obtained with and without the inclusion of spin-orbit coupling effects. Panel (b) present the band structure of a 2×2×2 $CsSnI_3$ supercell containing one V_{sn} defect (in green), compared to that of the pristine $CsSnI_3$ crystals (in blue). The Fermi level of the supercell with the defect is denoted by the red dashed line.

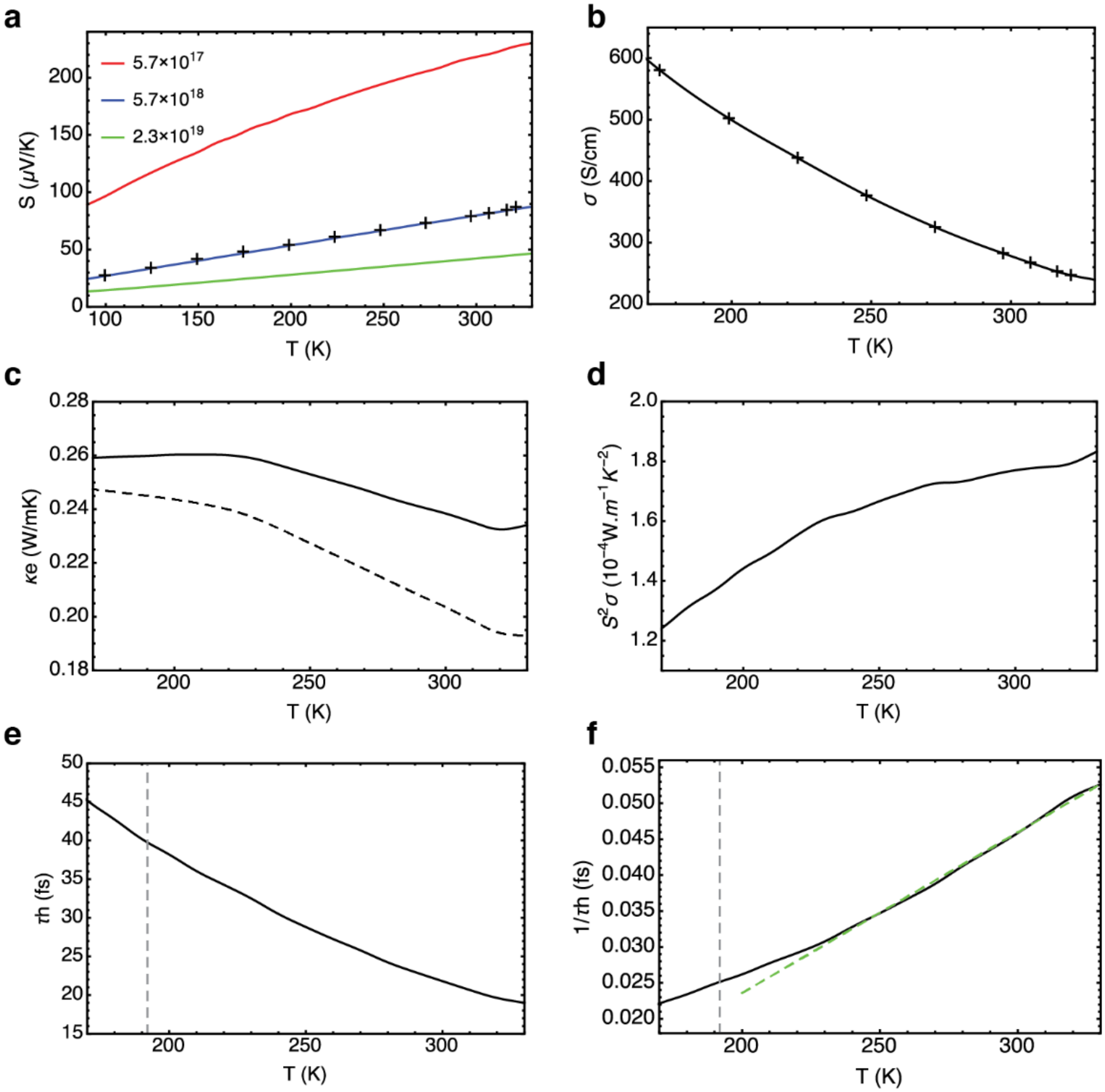

Figure 5-16. Calculated temperature dependent electrical transport properties of $CsSnI_3$ crystals. (a) Seebeck coefficients calculated with various carrier concentrations (in units of cm^{-3}), along with the experimental data presented by the cross symbols. (b) Electrical conductivities measured by experiment, with the curve illustrating the fitting to these values. (c) Electrical thermal conductivity calculated by our approach (in solid line) and that obtained by the Wiedemann-Franz

law (in dashed line). (d) Computed power factor. (e) Hole relaxation time and (f) its inverse with the Debye temperature denoted by gray dashed lines. The green dashed line shows the linear fitting between $1/\tau_h$ and T at high temperature.

5.8 Chapter 5 Conclusions:

Overall, $CsSnI_3$ inorganic halide perovskite NWs synthesized by low-temperature solution method shows several interesting and usually contraindicated properties: strong PL at 1.3 eV, metallic electrical conductivity, and ultralow thermal conductivity, which is within a factor of ~2 of the minimum thermal conductivity. Recently, rapid advances in the photovoltaic efficiency has attracted significant interest in halide perovskites, but based on the ultralow thermal conductivity, careful attention should likewise be focused regarding heat management for optoelectronic and other applications. The ultralow thermal conductivity reported in this work suggests that inorganic halide perovskites can be beneficial for solution-processable thermal-barrier coatings and thermoelectric applications. Furthermore, $CsSnI_3$ may act as a solution-processable electrically conductive thermal-barrier layer. Our theoretical analysis suggests that the formation of an inhomogeneous bonding network may serve as a new guideline for designing crystals with ultralow thermal conductivity.

5.9 Chapter 5 Supplemental Text:

Validation of the experimental setup: control experiment of amorphous SiO_2 (a-SiO_2) and comparison between measured thermal conductance and noise equivalent conductance (NEG):

In order to validate our thermal conductivity experimental results, we performed a control experiment on amorphous SiO_2 NWs that are known to have low thermal conductivity.[49] We first converted Si NWs grown by vapor-liquid-solid (VLS) method to amorphous SiO_2 (a-SiO_2) NWs by dry oxidation at 1000 °C for ~4 hours. As shown in Fig. 5-6a, conversion to a-SiO_2 is confirmed by HRTEM. We manipulated single a-SiO_2 NWs onto suspended thermal devices followed by Pt-C electron beam induced deposition (EBID) to improve thermal contacts between a-SiO_2 and membranes. The measured thermal conductivity of a-SiO_2 NWs with diameters 104 and 312 nm is in very good agreement with thermal conductivity of bulk a-SiO_2 (Fig. 5-6b). Thermal conductivity reduction due to a decreased characteristic length scale, such as a decreased diameter in this case, is not expected since the nanowires are amorphous. Therefore, it clearly demonstrates that our experimental setups are valid and accurate.

One could argue that thermal conductivity measurements of a-SiO_2 NW alone are not fully supportive of the validity of the experimental setup because the thermal conductivity of inorganic perovskite NWs is smaller than that of a-SiO_2 NW. To provide additional validation, we estimated the noise equivalent conductance (NEG) and compared it with our measured thermal conductance of inorganic perovskite NWs and a-SiO_2 NWs. We followed the procedure described in our earlier work[30] and estimated the minimum thermal conductance one can measure, which is set by the NEG and was found to be at most 5 times lower compared to the values reported in this work.

Characterization of contact resistance

When measuring thermal conductivity using suspended devices, one must consider thermal contact resistances between NWs and membranes. Experimentally measured thermal resistance (R) is the summation of intrinsic thermal resistance of nanowires (R_{nw}) and thermal contact resistance of two interfaces between nanowire and Pt electrode (R_c) as $R = R_{nw} + R_c$. In order to quantify the thermal contact resistance, we have measured the length-dependent thermal resistance of $CsSnI_3$ nanowires. Since the cross-sectional geometry is rectangular as seen in Fig. 5-3E, we followed the method,[32] where thermal contact resistance (R_c) multiplied by the cross-sectional area (A) is plotted as the length of nanowire (Fig. 5-7). Based on dimensions of the nanowires and the y-intercept, we can extract the thermal contact resistance. Estimated thermal contact resistance ranges from 0.5×10^6 to 3×10^6 K/W. These values are similar to previous measurements on other nanowires such as ZnO ($R_c \sim 1\times10^6$ K/W) and Bi ($R_c \sim 2.5\times10^5$).[50,51] As a result, estimated thermal contact resistance is only up to ~3 % of the intrinsic thermal resistance of the perovskite NWs. To obtain accurate thermal conductivity, we subtracted the estimated thermal contact resistances from measured total resistances.

Measurement of electrical conductivity (σ) and Seebeck coefficient (S)

We describe in this section how we measured the electrical conductivity and Seebeck coefficient of black phase $CsSnI_3$ using suspended devices. We measured four-probe resistance to eliminate contact resistances and to obtain the electrical conductivity at various temperatures, which is $\sigma = L/(R \cdot A)$ where L is the length and A is the cross-sectional area of the NW (Fig. 5-17a). In order to obtain the Seebeck coefficient, the temperature differential (ΔT) across individual NWs is created by applying Joule-heating into one of two membranes; open-circuit voltages (ΔV) are subsequently measured at several ΔT points (Fig. 5-17b). Since Seebeck coefficient is given by $S = -\Delta V / \Delta T$, the Seebeck coefficient can be readily calculated. We note that the Seebeck coefficient reported in this work is relative to the Seebeck coefficient of 50 nm Pt.

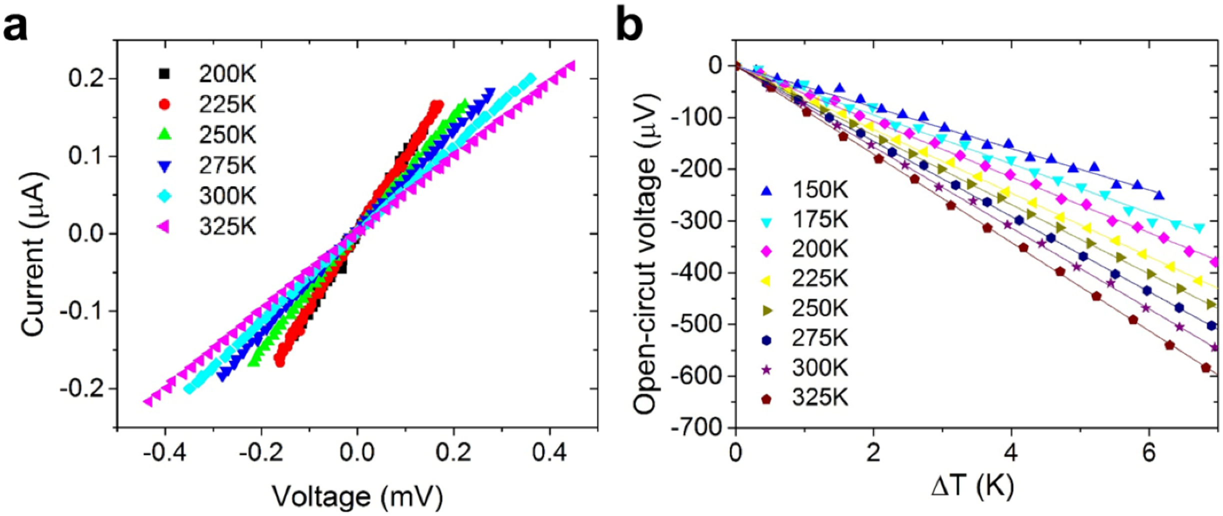

Figure 5-17. Experimental details of four-probe electrical measurement and Seebeck coefficient measurement. Measured I-V (a) and V-ΔT (b) of a black phase $CsSnI_3$ single nanowire at various temperatures.

5.10 Chapter 5 Methods:

Synthesis of the $CsSnI_3$ Nanowires: $CsSnI_3$ nanowires were synthesized as shown in Fig. 5-1, Fig. 5-2a,b. For this work, the yield of nanowires was optimized, and individual $CsSnI_3$ nanowires were applied for further characterization. $CsSnI_3$ nanowires were synthesized on clean substrates that were loaded with a layer of CsI and allowed to react in a solution of SnI_2 in anhydrous 2-propanol. All reagents were used as received without further purification. As reflected in Fig. 5-1 and Fig. 5-2a,b, in addition to the $CsSnI_3$ nanowires, other structures may also grow in solution. To grow $CsSnI_3$ nanowires, Si or SiO_2 (1 cm^2) substrates are cleaned by sequential sonication in acetone, 2-propanol, and deionized water, which is followed by drying under a stream of nitrogen. Subsequent steps are performed in an argon-filled glove box with an oxygen level of < 0.1 ppm and a H_2O level of < 2.0 ppm. A saturated solution of CsI (99.999%, anhydrous beads, Aldrich) in anhydrous methanol (99.8%, Spectrum) is prepared by allowing the solution to stir for at least 1 hour. Afterwards, the clean substrates are heated on a clean hotplate to 100°C and are allowed to equilibrate for 10 minutes. 70 μL of the saturated CsI solution is pipetted dropwise onto the hot substrates, which wets the surface completely, without spilling. For substrates of different size, the volume of the CsI/MeOH must scale appropriately to wet the surface of the substrate without spilling. The substrates are allowed to completely dry for up to 30 minutes on the hotplate. Anhydrous DMSO also can be used as a substitute for anhydrous methanol for this step. Afterwards, the CsI-coated substrates are placed in a clean 20 mL vial (Kimble, #FS74504-20) with the CsI-coated side facing up. The vial containing the CsI-coated chip is heated to 60°C before the reaction begins.

Separately, a saturated stock solution of SnI_2 (99.999%, ultra-dry, Alfa Aesar) in anhydrous 2-propanol (99.5%, Aldrich) is prepared (6.6 mmol/L) by stirring overnight, and the solution is diluted to 4 mmol/L to 0.3 mmol/L by diluting with anhydrous 2-propanol. To begin the reaction, 1 mL of SnI_2/2-propanol solution is pipetted onto the warm CsI-coated substrates, and the vial is capped and allowed to react for 90 to 120 minutes. To minimize oxygen and moisture contamination of the glove box, any paper inserts on the vial caps are removed prior to the reaction. The substrates darken with the nucleation and growth of $CsSnI_3$ in the SnI_2/2-propanol solution.

To stop the reaction, the chip is lifted out of the solution, and the chip is tipped towards the corner and any excess solution is wiped with a kimwipe to absorb the growth solution while minimizing the deposition of salts on the chip after evaporation of the growth solution. Optionally, the sample can be quickly washed in anhydrous 2-propanol and dried in the same manner. After synthesis, the sample is stored and transported in a sealed centrifuge tube to minimize air/humidity exposure.

X-ray diffraction: XRD of $CsSnI_3$ was acquired using a Bruker AXS D8 Advance diffractometer, which used Co Kα radiation with a wavelength of 1.79026 Å. To prepare the sample for XRD, a drop of PMMA (C4, MicroChem) was deposited and baked onto a $CsSnI_3$ sample grown on clean glass to improve the stability of the sample for XRD measurements in ambient air.

Scanning Electron Microscopy: SEM images of as-synthesized $CsSnI_3$ nanowires and nanostructures were taken using a JEOL JSM-6340F field emission scanning electron microscope. A Zeiss 1540 EsB instrument was used to take SEM images of single-nanowire devices and to perform electron beam induced deposition (EBID) of Pt-C.

Transmission Electron Microscopy: HRTEM and SAED of $CsSnI_3$ were collected on a FEI Titan microscope operated at 300 kV at the National Center for Electron Microscopy. The accelerating voltage of 300 kV was chosen to maximize contrast of the image through the relatively thick nanowires. As these samples were particularly beam sensitive, the electron dose was carefully controlled and was minimized to below 6000 to 200 $e/Å^2s$, depending on the nanowire. In all cases, the beam exposure of the nanowire was minimized before the HRTEM image was acquired.

Photoluminescence: Photoluminescence of $CsSnI_3$ single nanowires was measured using a focused 325 nm excitation from a HeCd laser with emission collected on a Nikon A1 microscope coupled to a multimode fiber. The spectra were acquired using a liquid-nitrogen-cooled InGaAs CCD (PI Acton).

Preparation of all-inorganic perovskite nanowires on devices: All-inorganic perovskite nanowires are manipulated onto suspended devices using a micromanipulator. Then, Pt-C is deposited to improve thermal and electrical contact between NW and Pt electrode on the suspended devices. $CsSnI_3$ is air-sensitive, and upon air-exposure black phase $CsSnI_3$ slowly changes to yellow phase $CsSnI_3$, according to previous reports.[23] Therefore, it requires special attention to prepare $CsSnI_3$ nanowires on suspended devices. To maintain the black-phase of $CsSnI_3$, we manipulate NWs to the suspended devices inside a chamber that is continuously purged with dry nitrogen gas. In addition, we keep the suspended devices inside a portable container filled with dry nitrogen to minimize air exposure when we transferred the devices between the EBID tool and the experimental setup.

Thermal conductivity measurement: The thermal conductivity measurement is based on a well-established single NW thermometry technique,[29,30] in which micro-islands are suspended from a substrate to force heat flux through a NW. Two symmetric island structures are each equipped with Pt electrodes, which can act as both a thermometer and a heater, and these islands are supported by thin and long SiN_x beams. Individual NWs are placed across the two islands by a manipulator such that the nanowire bridges the two islands. The nanowire is then mechanically and thermally anchored on the Pt electrode by electron beam induced deposition (EBID) of Pt-C. Subsequently, the single NW on the device is transferred to a closed cycle He cryostat (Janis). Under a high vacuum ($< 10^{-6}$ torr), one island is heated, and the bridged NW transports heat by conduction to the other island. During this process, the temperature of each membrane is monitored simultaneously. The temperature difference between the two islands is used to extract the thermal conductance of single NW. Knowing the temperature of each membrane and the amount of heat dissipation, the thermal conductance of a single NW can be quantified. The dimensions of the NW are measured using SEM, and the thermal conductivity is calculated using the obtained dimensions.

Computational Methods: The phonon contribution to thermal conductivity ($k_{lattice}$) of the bulk $CsSnI_3$was calculated by solving the Boltzmann transport equation (BTE) iteratively, as implemented in the ShengBTE package (v1.0.2),[38] with the second and third order interatomic force constants (IFCs) obtained by *ab-initio* simulations within the framework of density functional theory (DFT) using the Vienna Ab Initio Simulation Package (VASP, v5.3).[52] The electronic structures of bulk $CsSnI_3$ crystals were computed by standard DFT including spin-orbit coupling (SOC) with 8×8×6 and 8×16×3 Gamma k-point grids for γ and δ phases, and a 300 eV kinetic-energy cutoff. For the DFT calculations, plane-wave and projector-augmented-wave (PAW) type pseudopotentials with kinetic-energy cutoffs of up to 400 eV were applied, with the PBEsol exchange-correlation functional as implemented in the VASP package (v5.4).

Since $CsSnI_3$ exhibits *p*-type character in experiments, and the valence band structure near the band edge is barely affected by the SOC, we recalculated its band structure without SOC but using a very dense k-point grid of 20×20×16. The transport coefficients were then calculated by semi-classical Boltzmann theory with the RTA using the BoltzTraP package (v1.2.5).[53] The hole concentration (n_h) was determined by fitting the computed T-dependent Seebeck coefficient (S) to the experimental values. Similarly, the T-dependent relaxation time (τ_h) was obtained by fitting the calculated electrical conductivity (σ_h) to the experimental data. The electrical thermal conductivity (κ_e) and power factor (PF) were then computed with these τ_h and σ_h. Finally, the influence of Sn vacancy on the electronic structure was studied using a 2×2×2 supercell containing one defect.

5.11 Chapter 5 References:

1. McMeekin, D. P.; Sadoughi, G.; Rehman, W.; Eperon, G. E.; Saliba, M.; Hörantner, M. T.; Haghighirad, A.; Sakai, N.; Korte, L.; Rech, B.; Johnston, M. B.; Herz, L. M.; Snaith, H. J. *Science* **2016**, 351, 151-155.
2. Chung, I.; Lee, B.; He, J.; Chang, R. P. H.; Kanatzidis, M. G. *Nature* **2012**, 485, 486-489.

3. Tan, Z.-K.; Moghaddam, R. S.; Lai, M. L.; Docampo, P.; Higler, R.; Deschler, F.; Price, M.; Sadhanala, A.; Pazos, L. M.; Credgington, D.; Hanusch, F.; Bein, T.; Snaith, H. J.; Friend, R. H. *Nature Nanotech*. **2014**, 9, 687-692.
4. Hong, W.-L.; Huang, Y.-C.; Chang, C.-Y.; Zhang, Z.-C.; Tsai, H.-R.; Chang, N.-Y.; Chao, Y.-C. *Adv. Mater.* **2016**, 28, 8029-8036.
5. Zhu, H.; Fu, Y.; Meng, F.; Wu, X.; Gong, Z.; Ding, Q.; Gustafsson, M. V.; Trinh, M. T.; Jin, S.; Zhu, X. Y. *Nat. Mater*. **2015**, 14, 636-642.
6. Eaton, S. W.; Lai, M.; Gibson, N. A.; Wong, A. B.; Dou, L.; Ma, J.; Wang, L.-W.; Leone, S. R.; Yang, P. *Proc. Natl. Acad. Sci. USA* **2016**, 113, 1993-1998.
7. Cahill, D. G.; Braun, P. V.; Chen, G.; Clarke, D. R.; Fan, S.; Goodson, K. E.; Keblinski, P.; King, W. P.; Mahan, G. D.; Majumdar, A.; Maris, H. J.; Phillpot, S. R.; Pop, E.; Shi, L. *Appl. Phys. Rev.* **2014**, 1, 011305.
8. Skoplaki, E.; Palyvos, J. A. *Solar Energy* **2009**, 83, 614-624.
9. Cho, E. S.; Coates, N. E.; Forster, J. D.; Ruminski, A. M.; Russ, B.; Sahu, A.; Su, N. C.; Yang, F.; Urban, J. J. *Adv. Mater.* **2015**, 27, 5744-5752.
10. Pisoni, A.; Jaćimović, J.; Barišić, O. S.; Spina, M.; Gaál, R.; Forró, L.; Horváth, E. *J. Phys. Chem. Lett.* **2014**, 5, 2488-2492.
11. Hata, T.; Giorgi, G.; Yamashita, K. *Nano Lett.* **2016**, 16, 2749-2753.
12. Kulbak, M.; Gupta, S.; Kedem, N.; Levine, I.; Bendikov, T.; Hodes, G.; Cahen, D. *J. Phys. Chem. Lett.* **2016**, 7, 167-172.
13. Goodson, K. E. *Science* **2007**, 315, 342-343.
14. Snyder, G. J.; Toberer, E. S. *Nat. Mater.* **2008**, 7, 105-114.
15. Toberer, E. S.; Zevalkink, A.; Snyder, G. J. *J. Mater. Chem.* **2011**, 21, 15843-15852.
16. Balandin, A. A. *Nat. Mater.* **2011**, 10, 569-581.
17. Cahill, D. G. ; Watson, S. K.; Pohl, R. O. *Phys. Rev. B* **1992**, 46, 6131-6140.
18. Zhao, L.-D.; Tan, G.; Hao, S.; He, J.; Pei, Y.; Chi, H.; Wang, H.; Gong, S.; Xu, H.; Dravid, V. P.; Uher, C.; Snyder, G. J.; Wolverton, C.; Kanatzidis, M. G. *Science* **2016**, 351, 141-144.
19. Toberer, E. S.; Cox, C. A.; Brown, S. R.; Ikeda, T.;. May, A. F; Kauzlarich, S. M.; Snyder, G. J. *Adv. Funct. Mater*. **2008**, 18, 2795-2800.
20. Nolas, G. S.; Poon, J.; Kanatzidis, M. *MRS Bulletin* **2006**, 31, 199-205.
21. Chiritescu, C.; Cahill, D. G.; Nguyen, N.; Johnson, D.; Bodapati, A.; Keblinski, P.; Zschack P. *Science* **2007**, 315, 351-353.
22. Ravichandran, J.; Yadav, A. K.; Cheaito, R.; Rossen, P. B.; Soukiassian, A.; Suresha, S. J.; Duda, J. C.; Foley, B. M.; Lee, C.-H.; Zhu, Y.; Lichtenberger, A. W.; Moore, J. E.; Muller, D. A.; Schlom, D. G.; Hopkins, P. E.; Majumdar, A.; Ramesh, R.; Zurbuchen, M. A. *Nat. Mater*. **2014**, 13, 168-172.
23. Chung, I.; Song, J.-H.; Im, J.; Androulakis, J.; Malliakas, C. D.; Li, H.; Freeman, A. J.; Kenney, J. T.; Kanatzidis, M. G. *J. Am. Chem. Soc.* **2012**, 134, 8579-8587.
24. Stoumpos, C. C.; Malliakas, C. D.; Kanatzidis, M. G. *Inorg. Chem.* **2013**, 52, 9019-9038.
25. Jellicoe, T. C.; Richter, J. M.; Glass, H. F. J.; Tabachnyk, M.; Brady, R.; Dutton, S. E.; Rao, A.; Friend, R. H.; Credgington, D.; Greenham, N. C.; Böhm, M. L. *J. Am. Chem. Soc.* **2016**, 138, 2941-2944.
26. Kumar, M. H.; Dharani, S.; Leong, W. L.; Boix, P. P.; Prabhakar, R. R.; Baikie, T.; Shi, C.; Ding, H.; Ramesh, R.; Asta, M.; Graetzel, M.; Mhaisalkar, S. G.; Mathews, N. *Adv. Mater.* **2014**, 26, 7122-7127.

27. Zhu, H.; Fu, Y.; Meng, F.; Wu, X.; Gong, Z.; Ding, Q.; Gustafsson, M. V.; Trinh, M. T.; Jin, S.; Zhu, X. Y. *Nat. Mater.* **2015**, 14, 636-642.
28. Fu, Y.; Meng, F.; Rowley, M. B.; Thompson, B. J.; Shearer, M. J.; Ma, D.; Hamers, R. J.; Wright, J. C.; Jin, S. *J. Am. Chem. Soc.* **2015**, 137, 5810-5818.
29. Shi, L.; Li, D.; Yu, C.; Jang, W.; Kim, D.; Yao, Z.; Kim, P.; Majumdar, A. *J. Heat Trans.* **2003**, 125, 881-888.
30. Lee, J.; Lee, W.; Lim, J.; Yu, Y.; Kong, Q.; Urban, J. J.; Yang, P. *Nano Lett.* **2016**, 16, 4133-4140.
31. Xu, X.; Pereira, L. F. C.; Wang, Y.; Wu, J.; Zhang, K.; Zhao, X.; Bae, S.; Tinh Bui, C.; Xie, R.; Thong, J. T. L.; Hong, B. H.; Loh, K. P.; Donadio, D.; Li, B.; Özyilmaz, B. *Nat. Comm.* **2014**, 5, 3689.
32. Lee, S.; Yang, F.; Suh, J.; Yang, S.; Lee, Y.; Li, G.; Sung Choe, H.; Suslu, A.; Chen, Y.; Ko, C.; Park, J.; Liu, K.; Li, J.; Hippalgaonkar, K.; Urban, J. J., Tongay, S.; Wu, J. *Nat. Comm.* **2015**, 6, 8573.
33. Lü, X.; Chu, J. H.; Shen, W. Z. *J. Appl. Phys.* **2003**, 93, 1219-1229.
34. Wood, C. *Rep. Prog. Phys.* **1988**, 51, 459.
35. C. Uher, in *Semiconductor and Semimetals*, T. M. Tritt, Ed. (Academic Press, San Diego, 2001), vol. 69, pp. 139-253.
36. May, A. F.; Toberer, E. S.; Saramat, A.; Snyder, G. J. *Phys. Rev. B* **2009**, 80, 125205.
37. Cox, C. A.; Toberer, E. S. Levchenko, A. A.; Brown, S. R.; Snyder, G. J.; Navrotsky, A.; Kauzlarich, S. M. *Chem. Mater.* **2009**, 21, 1354-1360.
38. Li, W.; Carrete, J.; Katcho, N. A.; Mingo, N. *Comp. Phys. Comm.* **2014**, 185, 1747-1758.
39. Cahill, D. G.; Watson, S. K.; Pohl, R. O. *Phys. Rev. B* **1992**, 46, 6131-6140.
40. Qiu, B.; Bao, H.; Zhang, G.; Wu, Y.; Ruan, X. *Comp. Mater. Sci.* **2012**, 53, 278-285.
41. Dong, J. J.; Sankey, O. F.; Myles, C. W. *Phys. Rev. Lett.* **2001**, 86, 2361-2364.
42. Tadano, T.; Gohda, Y.; Tsuneyuki, S. *Phys. Rev. Lett.* **2015**, 114, 095501.
43. Schweika, W.; Hermann, R. P.; Prager, M.; Persson, J.; Keppens, V. *Phys. Rev. Lett.* **2007**, 99, 125501.
44. He, Y.; Galli, G. *Nano Lett.* **2014**, 14, 2920-2925.
45. Zhao, L.-D.; Lo, S.-H.; Zhang, Y.; Sun, H.; Tan, G.; Uher, C.; Wolverton, C.; Dravid, V. P.; Kanatzidis, M. G. *Nature* **2014**, 508, 373-377.
46. Yi, T.; Cox, C. A.; Toberer, E. S.; Snyder, G. J.; Kauzlarich, S. M. *Chem. Mater.* **2010**, 22, 935-941.
47. Brown, S. R.; Kauzlarich, S. M.; Gascoin, F.; Snyder, G. J. *J. Sol. State Chem.* **2007**, 180, 1414-1420.
48. Winter, M. R.; Clarke, D. R. *J. Am. Cer. Soc.* **2007**, 90, 533-540.
49. Hochbaum, A. I.; Chen, R. K.; Delgado, R. D.; Liang, W. J.; Garnett, E. C.; Najarian, M.; Majumdar, A.; Yang, P. *Nature* **2008**, 451, 163-165.
50. Bui, C. T.; Xie, R.; Zheng, M.; Zhang, Q.; Sow, C. H.; Li, B.; Thong, J. T. L. *Small* **2012**, 8, 738-745.
51. Moore, A. L.; Pettes, M. T.; Zhou, F.; Shi, L. *J. Appl. Phys.* **2009**, 106, 034310.
52. Kresse, G.; Furthmuller, J. *Phys. Rev. B* **1996**, 54, 11169-11186.
53. Madsen, G. K. H.; Singh, D. J. *Comp. Phys. Comm.* **2006**, 175, 67-71.

Conclusions

Following all the discussion of my graduate research, I would like to take this opportunity to make some remarks about the potential directions of these research fields in addition to the conclusions appearing at the end of each chapter. In a sense, my research with Prof. Peidong Yang has come full circle from Cu_2S to $CsSnI_3$. My first project was related to the synthesis of Cu_2S, which is an air sensitive, degenerately doped p-type semiconductor with a band gap of 1.2 eV. My final project is also related to the synthesis of $CsSnI_3$, which is an air sensitive, highly conductive, p-type semiconductor with a band gap of 1.3 eV. I feel that the connection between these two materials is also illustrative of some directions within the field of nanoscale materials chemistry.

Cu_2S as a material had fallen out of favor as compared to alloys such as copper indium selenide, copper indium gallium selenide, and copper zinc tin sulfide in part because of the high instability of Cu_2S. Nonetheless, contemporary work on this material was merited because of the potential for this material to serve as an earth-abundant and solution processable light absorber material. The introduction of nanostructured Cu_2S might also mitigate the short minority carrier diffusion length of this material. Although it does not appear to be the most promising direction, there is still the potential to improve the performance of Cu_2S-based photovoltaics.

Recently, there has been a large shift in the field of nanostructured materials for optoelectronics with the emergence of halide perovskites, which offer high photoluminescence quantum efficiency, high mobility, and high defect tolerance. As a result, lab scale photovoltaic device efficiencies rapidly approached 20%, which has arguably redirected efforts in developing other types of light absorbers for high efficiency solution processable photovoltaics.

Regarding the halide perovskite materials, it is my belief going forwards that their defect tolerance is the main feature that makes these materials most interesting as solution processable semiconductors. It remains to be seen whether the successes in this area at the lab scale can be translated into the development of new beneficial technologies. Two potential stumbling blocks for this are the instability of these materials and the presence of lead.

As a result, two future research directions to deal with these fundamental issues are the development of new defect tolerant solution processable semiconductors similar to the halide perovskites, and the development of lead-free halide perovskites explicitly. It is for this reason that I have pursued the development of $CsSnI_3$. As for the other proposed direction, I will be eagerly awaiting reports of the development of new defect tolerant solution processable semiconductor materials in the coming years.